

SANDIA REPORT

SAND2013-8064

Unlimited Release

Printed September, 2013

Multiscale Modeling for Fluid Transport in Nanosystems

J.W. Lee, R.E. Jones, K.K. Mandadapu, J.A. Templeton, J.A. Zimmerman

Prepared by

Sandia National Laboratories

Albuquerque, New Mexico 87185 and Livermore, California 94550

Sandia is a multiprogram laboratory operated by Sandia Corporation,
a Lockheed Martin Company, for the United States Department of Energy's
National Nuclear Security Administration under Contract DE-AC04-94-AL85000.

Approved for public release; further dissemination unlimited.



Sandia National Laboratories

Issued by Sandia National Laboratories, operated for the United States Department of Energy by Sandia Corporation.

NOTICE: This report was prepared as an account of work sponsored by an agency of the United States Government. Neither the United States Government, nor any agency thereof, nor any of their employees, nor any of their contractors, subcontractors, or their employees, make any warranty, express or implied, or assume any legal liability or responsibility for the accuracy, completeness, or usefulness of any information, apparatus, product, or process disclosed, or represent that its use would not infringe privately owned rights. Reference herein to any specific commercial product, process, or service by trade name, trademark, manufacturer, or otherwise, does not necessarily constitute or imply its endorsement, recommendation, or favoring by the United States Government, any agency thereof, or any of their contractors or subcontractors. The views and opinions expressed herein do not necessarily state or reflect those of the United States Government, any agency thereof, or any of their contractors.

Printed in the United States of America. This report has been reproduced directly from the best available copy.

Available to DOE and DOE contractors from
U.S. Department of Energy
Office of Scientific and Technical Information
P.O. Box 62
Oak Ridge, TN 37831

Telephone: (865) 576-8401
Facsimile: (865) 576-5728
E-Mail: reports@adonis.osti.gov
Online ordering: <http://www.osti.gov/bridge>

Available to the public from
U.S. Department of Commerce
National Technical Information Service
5285 Port Royal Rd
Springfield, VA 22161

Telephone: (800) 553-6847
Facsimile: (703) 605-6900
E-Mail: orders@ntis.fedworld.gov
Online ordering: <http://www.ntis.gov/help/ordermethods.asp?loc=7-4-0#online>



Multiscale Modeling for Fluid Transport in Nanosystems

Jonathan W. Lee, Reese E. Jones, Kranthi K. Mandadapu,
Jeremy A. Templeton, Jonathan A. Zimmerman
Sandia National Laboratories, P.O. Box 969
Livermore, CA 94550-0969

Abstract

Atomistic-scale behavior drives performance in many micro- and nano-fluidic systems, such as microfluidic mixers and electrical energy storage devices. Bringing this information into the traditionally continuum models used for engineering analysis has proved challenging. This work describes one such approach to address this issue by developing atomistic-to-continuum multi scale and multi physics methods to enable molecular dynamics (MD) representations of atoms to be incorporated into continuum simulations. Coupling is achieved by imposing constraints based on fluxes of conserved quantities between the two regions described by one of these models. The impact of electric fields and surface charges are also critical, hence, methodologies to extend finite-element (FE) MD electric field solvers have been derived to account for these effects. Finally, the continuum description can have inconsistencies with the coarse-grained MD dynamics, so FE equations based on MD statistics were derived to facilitate the multi scale coupling. Examples are shown relevant to nanofluidic systems, such as pore flow, Couette flow, and electric double layer.

Acknowledgment

Sandia National Laboratories is a multi-program laboratory managed and operated by Sandia Corporation, a wholly owned subsidiary of Lockheed Martin Corporation, for the U.S. Department of Energy's National Nuclear Security Administration under contract DE-AC04-94AL85000. This work was funded under LDRD Project Number 151294 and Title "Multiscale Modeling for Fluid Transport in Nanosystems". The authors gratefully acknowledge helpful comments from Drs. Jeremy Lechman, Paul Crozier, Helgi Adalsteinsson, and Greg Wagner.

Contents

1	Introduction	13
2	Polarization as a field variable from molecular dynamics simulations	15
2.1	Introduction	15
2.2	Theory	16
2.3	Computational Framework	20
2.4	Applications to Small Polar Molecules	22
2.4.1	Bulk Water	22
2.4.2	Solid Liquid Interface – Electrical Double Layer	24
2.5	Discussion	25
2.6	Run-Time Cost Estimate for Molecular Coarse-Graining Algorithm	26
3	A Fractional Step Method for Conserved Energy Exchange in Coupled Atomistic-Finite Element Simulations	37
3.1	Introduction	37
3.2	Derivation of the Temporally Continuous Equations	39
3.2.1	Coupling with Thermostats	41
3.3	Fractional Step Time Advancement	44
3.3.1	Time Integration Scheme	44
3.4	Thermostat Framework for Energy Conservation	49
3.4.1	Discrete Thermostats	49
3.5	Example Problems	51
3.5.1	Thermal Conductivity of Liquid Argon	51

3.5.2	Multiscale Liquid Argon	51
3.6	Conclusions	51
3.7	Consistent Formulation for Combined Fixed Temperature/Energy Flux Localized Thermostats	55
4	A Method for Atomistic-to-Continuum Combined Thermal and Mechanical Coupling	59
4.1	Introduction	59
4.2	Coupled Finite Element/Atomistic Momentum and Temperature Equations	61
4.3	Combined Kinetostat/Thermostats	65
4.3.1	Direct Temperature and Velocity Imposition	65
4.3.2	Constraint-Based Atomistic-to-Continuum Coupling	66
4.4	Temporal Integration Scheme	68
4.5	Examples	69
4.5.1	Couette Flow	69
4.5.2	Electro-osmotic Flow	71
4.6	Conclusion	72
5	Sensitivity to physical parameters in MD simulations of concentration driven ionic flow through a silica nanopore	77
5.1	Introduction	77
5.2	Atomistic system and MD simulations	79
5.2.1	Atomistic system	79
5.2.2	Force-field	81
5.2.3	MD simulations	82
Equilibration	83	
Concentration Control	83	
5.3	Dependence on the pore diameter	84
5.3.1	Velocity profiles	85

5.3.2	Ionic conductance	87
5.4	Sensitivity to the gating charge	89
5.4.1	UQ Formulation	90
5.4.2	Bayesian regression	91
	Collection of observations	91
	Noise model and likelihood function	93
5.4.3	Bayesian regression: results	95
	Bayes Factor	98
	Posterior predictive check and predictive uncertainty	99
5.5	Conclusions	100
5.6	Appendix: Dual control volume concentration control algorithm	101
5.6.1	Concentration control	102
5.6.2	Temperature and momentum control	103
6	Finite Element Methods for Fluctuating Hydrodynamics	109
6.1	Introduction	109
6.2	Strong Form of Fluctuating Hydrodynamic Equations	109
6.3	Weak Form of Fluctuating Hydrodynamic Equations	110
7	Conclusions	113
	References	115

List of Figures

2.1	Bulk water: Running time-average of polarization vector in the z direction at the center of the system for several coarse-graining length scales and an applied electric field of $E_{ez} = -0.72 V/\text{\AA}$ using a constant coarse-graining function (2.18).	29
2.2	Bulk water: Running time-average of the dipole and quadrupole moment contributions to the total polarization vector in the z direction at the center of the system for an applied electric field of $E_{ez} = -0.72 V/\text{\AA}$ and a coarse-graining length of 5\AA using constant and linear coarse-graining functions given by (2.18) and (2.19), respectively.	30
2.3	Bulk water: Magnitude of Polarization as a function of magnitude of local electric field. The solid red line shows a linear fit to the data in the range where polarization varies linearly with local electric field. The dielectric susceptibility constant which is the slope of the linear fit is found to be $\chi_e = 71 \pm 3$. Inset shows the range where the polarization density is linearly proportional to the resultant electric field.	31
2.4	Bulk water: Spatially varying dipole $\left(\int_{\Gamma} \sum_{m=1}^{N_m} \mathbf{p}_m \Delta(\mathbf{y} - \mathbf{x}_m) d\Gamma \right)$ and quadrupole moment $\left(\int_{\Gamma} \frac{\partial}{\partial \mathbf{y}} \cdot \sum_{m=1}^{N_m} \left(\mathbf{q}_m \Delta(\mathbf{y} - \mathbf{x}_m) \right) f(\Gamma, t) d\Gamma \right)$ contributions to the total polarization density given by the first two terms on the right hand side of (2.16). A linear coarse-graining function corresponding to a coarse-graining length of 0.05\AA is used. The left and right walls are located at -21.34595\AA and 21.34595\AA , respectively	32
2.5	Bulk water: Resultant polarization vector containing contributions only from the dipole and quadrupole moments using a linear coarse-graining function (2.19) and a coarse-graining length of 0.05\AA	33
2.6	EDL: The wall-normal component of the polarization vector for several coarse-graining length scales using constant coarse-graining function (2.18).	34
2.7	EDL: Close-up of the wall-normal component of the polarization vector near the negatively charged wall.	35
2.8	EDL: Spatially varying wall-normal component of the resultant (microscopic) electric field.	35

2.9	EDL: Close-up of the wall-normal component of the microscopic electric field near the negatively charged wall.	36
3.1	Schematic of the quasi-1D test cases used in this work. Atoms which are part of the AtC method are yellow while boundary atoms used to confine the atoms and reflect phonons are in blue. The FE mesh is in red.	52
3.2	Mean and standard deviation of the temperature profile using fixed	53
3.3	Mean and standard deviation of the temperature profile.	54
4.1	Schematic of the Couette flow MD configuration. Surface atoms are yellow while fluid atoms are green.	70
4.2	Time evolution of Couette flow.	71
4.3	Schematic of the electrokinetic flow model configuration. Surface atoms are yellow while fluid atoms are blue, positively charged ions are green, and negatively charged ions are orange. The FE mesh is shown in red.	73
4.4	Time evolution of the electrokinetic flow.	74
5.1	(a) Schematic of the dual-reservoir nanopore system. The silica is a rectangular block with a cylindrical pore of nominal radius R . Only few surface layers of the silica block have dynamics (gray), shown in panel (b), while the rest comprises the “frozen” atoms (green). The volume of fluid is nominally $V_f = (2L_x L_y L_z^{(w)} + \pi R^2 L_z^{(s)})$	79
5.2	Silica pore model of dimensions (x, y, z) $L_x \approx 54$, $L_y \approx 60$ and $L_z^{(s)} \approx 32$ Å obtained from a bulk crystal silica structure after carving a pore of nominal radius R , ensuring stoichiometry, and hydroxylating the surface and pore defects. Color legend: silicon Si (ochre), bulk oxygens O_{bulk} (blue), hydroxide oxygens O_{hy} (yellow) and hydroxide hydrogens H_{hy} (black).	80
5.3	Snapshots of cross-sectional views of the systems for $D = 12.5$ (a), 17 (b), 21 (c) and 27 Å (d), taken during the steady state of the CC stage. Color legend: Si (ochre), O_{bulk} (blue), O_{hy} (yellow), H_{hy} (black), O_w (red), H_w (white), Na^+ (purple), Cl^- (cyan). The silica is nearly transparent for visualization convenience.	85

5.4	(a) Time/bin-averaged radial profile of the axial velocity v_z , for Na^+ and Cl^- computed for one replica of the case $D = 21 \text{ \AA}$ during the steady phase of the CC stage. (b) Time/bin-averaged axial velocity v_z plotted as a function of the z -coordinate computed for one replica of $D = 21 \text{ \AA}$ at the final step of the CC stage for water, Na^+ and Cl^- . In (a), for the sake of visualization, the data obtained from the spatial binning are interpolated over a finer mesh. In (b) the filled circles are plotted at the location of the 24 bins.	86
5.5	Time evolution of the running average conductance, $G(t)$, for Na^+ (a) and Cl^- (b) plotted for all 5 replicas and each diameter value showing the variation in steady state values and the timescale at which steady values are achieved.	88
5.6	(a) Steady-state replica values (markers) of the Na^+ (blue) and Cl^- (red) conductance as a function of the nominal pore diameter D , with the superimposed lines outlining the replica-averaged values. (b) Coefficient of variation, σ/μ , i.e. the ratio of the standard deviation, σ , over the mean, μ , of the conductance data plotted as function of the pore diameter, D , for both ions.	88
5.7	Snapshots obtained for $D = 12.5$ (a), 17 (b), 21 (c) and 27 \AA (d), during the steady state of the CC stage, showing the distribution of water molecules around the ions passing through the pore: Na^+ is color-coded purple, while Cl^- is color-coded cyan.	89
5.8	Panel (a): data set of the ionic conductance, G , computed for all replicas as a function of the gating charge density q_{surf} for Na^+ and Cl^- . The superimposed solid lines connect the replica-averaged values. Panel (b) shows the corresponding variances plotted as function of q_{surf} with a logarithmic scale on the y -axis. Note that since $q_{surf} = 0.265619083 \text{ Coul/m}^2$ yields vanishing Na^+ conductance for all three replicas, the corresponding variance is not shown panel (b).	92
5.9	Top row: Scatter plots of 20000 MCMC chain samples obtained for $\pi(g_0, g_1)$ for Na^+ (a) and Cl^- (b), extracted from the original MCMC chain by removing the burn-in period comprising the first 15000 samples. Bottom row: marginalized posterior, $\pi(g_k)$, of each PC coefficient g_k , $k = 0, \dots, 4$, obtained via KDE for Na^+ (c) and Cl^- (d). All panels show the results for a linear ($P = 1$), quadratic ($P = 2$), cubic ($P = 3$), and quartic ($P = 4$) expansion.	105
5.10	Panel (a) shows the comparison between the data points of the Na^+ (black circles) conductance and the corresponding predictions obtained from the MAP estimate of the PC regression function, $M(\xi)$, computed for a linear ($P = 1$), quadratic ($P = 2$), cubic ($P = 3$), and quartic ($P = 4$) expansion as a function of q_{surf} . The corresponding results for Cl^- are shown in panel (b).	106

5.11	Panel (a) shows the data-based variance (black circles) of the Na^+ conductance versus the corresponding predictions obtained from the MAP estimate of the noise PC coefficients $\{d_0, d_1\}$, as a function of the order, P , of the regression function, $M(\xi)$. The corresponding results for Cl^- are shown in panel (b). Both plots are presented with a log scale on the y-axis.	106
5.12	Results showing the posterior predictive check samples (gray) obtained for the Na^+ (a) and Cl^- (b) conductance using a third-order and fourth-order PC representation, respectively. Superimposed to the plots, we report the original data color-coded blue for Na^+ and red for Cl^- , and the mean (black square) and error bars for $\pm 3\tilde{\sigma}$, where $\tilde{\sigma}$ is the standard deviation calculated from the original data-set of conductances used in the inference.	107
5.13	Results of the “model uncertainty” analysis obtained for Na^+ (a) and Cl^- (b) showing how the posterior uncertainty in the inferred PC representations of the conductances is reflected in the corresponding predictions.	107

List of Tables

4.1	Self-interaction LJ potentials for all species used in Section 4.5.2.	72
5.1	Lennard-Jones parameters (ϵ, σ) and Coulombic charge, in multiples of the electron charge $ e $, for each atom type present in the system: $\{H_w, O_w\}$ are water hydrogen and oxygen atoms, respectively, $\{H_{hy}, O_{hy}\}$ are hydrogen and oxygen atoms appearing in an hydroxide group, O_{bulk} are oxygen atoms in the bulk of the silica, Si are silicon atoms and $\{Na^+, Cl^-\}$ are the salt ions. The Lorentz-Berthelot mixing rules $\sigma_{\alpha\beta} = \frac{1}{2}(\sigma_\alpha + \sigma_\beta)$, and $\epsilon_{\alpha\beta} = \sqrt{\epsilon_\alpha \epsilon_\beta}$ are used to define the interspecies Lennard-Jones interactions. For the remaining set of force-field parameters, refer to Ref. [82] for <i>silica</i> , to Ref. [56, 88] for <i>water</i> and to Ref. [104] for the <i>ions</i>	82
5.2	Computed values of $\ln B(\theta_{p_1}, \theta_{p_2})$, obtained for all four different models and each ion Na^+ and Cl^- . Note that due to the logarithmic scale adopted, for a given ion, the corresponding matrix of values is antisymmetric.	99

Chapter 1

Introduction

The behavior of fluids taking place at the nanoscale plays an important role in applications relevant to Sandia's missions, such as microfluidic devices for chemical detection and reactor regulation for biofuels, as well as battery and capacitor performance and safety for NW systems and CO₂ mitigation. In particular, the interaction between an electrolyte solution often plays a critical role in determining device performance. Microfluidic devices relying on electrokinetic flows often produce velocities far below those predicted by established theories (e.g., Poisson-Boltzmann) because they do not take into account finite packing of atoms and changes to the electrical media near the surface. Similarly, energy storage devices rely on double layers, both for transport through pores as well as directly for their capacitance. Improved simulation capabilities are therefore needed to gain increased understanding and guide design of micro- and nanofluidic systems.

Significantly hindering predictive simulation technologies for flows at the nanoscale are the divergent physical processes taking place. Adjacent to surfaces, atomistic effects dominate. The lattice imposes a structure on the fluid atoms, preventing them from arranging randomly. As a result, established fluid properties such as viscosity, to the extent they apply at all, can vary by orders of magnitude from their bulk equilibrium values. The effects of defects and other surface structures can similarly not be incorporated into continuum models.

By modeling the fluid as a continuum, however, significant computational savings are achieved because each continuum element contains 100s or more fluid particles. To model systems of technologically relevant sizes, such approaches are necessary in order to perform the number of calculations needed to explore the relevant parameter space. Continuum descriptions are fundamentally different from atomistic representation of matter so that the same computational infrastructure is inappropriate for both. Additionally, different information and parameters in the form of constitutive models and boundary conditions are required for each. The most direct way to obtain the benefits of both while mitigating the drawbacks of each is to develop a multiscale framework in which each approach is used in the domain to which it is best suited.

Sandia National Laboratories has established expertise in both atomistic modeling (through the molecular dynamics (MD) code LAMMPS [106]) and continuum modeling (through the SIERRA project). Previous efforts have also developed a multiscale atomistic-to-continuum (AtC) package for post-processing atomic data in terms of continuum quantities [137, 138], heat transfer [129, 123], and electric fields [122]. Missing from this capability set has been the consideration of fluids problems, which require the ability to simultaneously couple mass, momentum, and energy.

Unlike problems in solid mechanics, fluids are often described in the Eulerian frame and concern the convective transport of mass. It is also difficult to separate momentum and thermal transport because shear flows will generate heat, which must then be propagated away from the atoms. Finally, constituents in technologically important material systems tend to be molecular in nature, rather than atomistic as in solids.

The goal of this project was to fill this capability gap by developing a computational framework to enable AtC simulations of fluid-mediated transport at the nanoscale. Outcomes have been new theoretical constructions for combined mass/momentum/energy multiscale coupling and incorporation of molecular data into a multiscale framework. This latter effort is described in the next chapter. As the project advanced, it was discovered that the existing techniques to integrate the governing equations in time were not sufficiently robust to meet these requirements. A new time integration approach based on the fractional step method is described in Chapter 3. Chapter 4 builds on this work by presenting a methodology for simultaneous control and regulation of momentum and energy. The presentation then turns to a full mass/momentum/energy prescription in a nanopore geometry in Chapter 5. Another important lesson-learned during this project was that traditional continuum governing equations well known from macroscale physics can be inappropriate at both the nanoscale and in the context of multiscale simulations. Chapter 6 presents a reformulation of the continuum Navier-Stokes equations by including Brownian fluctuations and rescaling the equations to be appropriate for small-scale phenomena. This report concludes with Chapter 7, which provides an overview of the methods as well as a description of the software developed and released as part of this project.

Chapter 2

Polarization as a field variable from molecular dynamics simulations

2.1 Introduction

Polarization, \mathbf{P} , is an important quantity in electromagnetism that signifies the density of dipole moments in a dielectric material. These dipole moments can either be induced, for example in the case of non-polar molecules where the nucleus and the electronic charge separate in the presence of an electric field, or permanent in the case of polar molecules such as water. When in a fluid phase, polar molecules, and hence their dipoles, are distributed in a random fashion. In the presence of an electric field, these dipoles experience a torque that tends to align them in the direction of the applied field. The resultant polarization vector \mathbf{P} is then combined with the electric field \mathbf{E} to yield the electric displacement vector $\mathbf{D} = \epsilon_0\mathbf{E} + \mathbf{P}$, which enters into the macroscopic Maxwell's equation, where ϵ_0 is the vacuum permittivity [55]. An isotropic dielectric material is usually modeled by proposing a linear constitutive relation between the polarization vector and the electric field vector, $\mathbf{P} = \epsilon_0\chi_e\mathbf{E}$, where χ_e is the dielectric susceptibility [73]. In this case, $\mathbf{D} = \epsilon\mathbf{E} = \epsilon_0(1 + \chi_e)\mathbf{E}$ where ϵ is the dielectric constant of the material, which usually depends on the material and its state parameters such as density, temperature, *etc.*

Electrical double layers (EDL) in electrolyte solutions at a charged surface are typically modeled using Poisson-Boltzmann [39, 16, 50], modified Poisson-Boltzmann [14, 15], and composite diffuse-layer theories [63]. These theories are based on the assumption that the solvent throughout the double layer can be modeled with the bulk dielectric constant, *i.e.*, the polarization vector is directly proportional to the local electric field with the constant of proportionality being the bulk dielectric susceptibility of the solvent. However, this assumption breaks down close to the interface, where the solvent is organized in a structured manner [76]. Therefore, new models are required to accurately capture the effects of solvent close to the interface to represent the relationship between the polarization vector and the electric field. Such models can be formulated with the help of molecular dynamics (MD) simulations, where one may obtain solvent configurations in great detail as a function of distance from the interface. In such cases, it would be convenient to be able to obtain the spatially and temporally varying polarization vector, which can be related to the resultant local electric fields. The main objective of this paper is to provide a theoretical

The primary authors of this chapter are K. Mandadapu, J. Templeton, and J. Lee. It was originally published in [90].

and computational framework for obtaining the polarization vector as a field variable from MD simulations.

Earlier work on evaluating polarization vectors from MD simulations concerned calculations of the bulk dielectric constant of systems such as water; however, these methods obtain the polarization vector of the entire system [43]. A technique for computing the local polarization vector for electrolyte systems (NaCl + water) in nanochannels was described in [64]. In this method, the entire channel is divided into subregions and the spatial polarization vector is defined as the dipole moment densities in every subregion. However, it is not entirely clear how the polarization vector varies when one increases the size of the subregion. Moreover, obtaining polarization as a density of dipole moments might be applicable only for small-molecular solvents with predefined dipoles such as water. As the solvent size becomes bigger, it is not entirely clear how a spatial polarization density can be obtained systematically as the solvent can exist in different bins at the same time. Moreover, techniques of this kind have no way of quantifying the contribution of higher order moments (quadrupole, *etc*) to the overall polarization density. For example, it is well known that quadrupole moments contribute significantly to the dielectric constant of solvents such as benzene [72, 9]. In this paper, a general theoretical and computational procedure is described where the polarization vector so obtained does not depend on the specific structure of the system. This procedure also provides a way to obtain the polarization density to the desired accuracy.

The paper is organized as follows: In Section 2.2, the Irving-Kirkwood theory [53], which is developed for obtaining the stresses and heat-fluxes in terms of molecular positions and momenta, and the procedure for obtaining instantaneous polarization vector as described by Jackson [55, Chapter 6] are extended to the case of electrostatics. Here, the macroscopic electrostatic equation is obtained by coarse-graining the microscopic electrostatic equation by means of a suitable coarse-graining function and phase-space distribution function resulting in an expression for polarization density as a function of molecular dipole, quadrupole, and higher-order moments. A computational framework for evaluating the polarization density is described in Section 2.3. This theory is then tested on bulk water to recover its bulk dielectric constant in Section 2.4.1. Finally, the theory is applied to obtain the spatial polarization field in the electrical double layers of a 1:1 electrolyte solution confined between equal and oppositely charged surfaces in Section 2.4.2.

2.2 Theory

In this section, a theory for obtaining the polarization vector \mathbf{P} in terms of the molecular positions and charges is presented. Consider a system consisting of N atoms. Let $\mathbf{x}_1, \mathbf{x}_2, \dots, \mathbf{x}_N$ and $\mathbf{p}_1, \mathbf{p}_2, \dots, \mathbf{p}_N$ denote the positions and momenta of all atoms, respectively. Let $\Gamma = \{(\mathbf{x}_i, \mathbf{p}_i), i = 1, 2, \dots, N\}$ and $f(\Gamma, t)$ denote the phase-space and the associated phase-space distribution, respectively, such that

$$\int_{\Gamma} f(\Gamma, t) d\Gamma = 1. \quad (2.1)$$

The trajectories of atoms in the system are obtained by integrating Newton's equations of motion $m_i \dot{\mathbf{x}}_i = \mathbf{p}_i$ and $\dot{\mathbf{p}}_i = \mathbf{f}_i$, given initial conditions, masses m_i , and forces \mathbf{f}_i . The force \mathbf{f}_i on atom

i is the sum of interatomic forces obtained using an interatomic potential, Coulomb forces, and thermostat forces used to control the thermodynamic state of the system. The scale at which individual atoms are described is defined as the microscale and is denoted by \mathbf{x} . Let the scale at which quantities defined as averages over infinitesimal volumes containing groups of atoms and phase-space distribution be defined as the macroscale denoted by \mathbf{y} . Since the objective of the paper is to obtain the polarization vector, which is a macroscopic quantity entering the macroscopic Maxwell's equation, in terms of the molecular variables it is possible only by coarse-graining the exact microscopic electrostatic equation and comparing it with the macroscopic electrostatic equation.

To this end, the microscopic electrostatic equation at any instant is given by

$$\nabla \cdot \mathbf{e}(\mathbf{x}, t) = \frac{\rho^m(\mathbf{x}, t)}{\epsilon_0}, \quad (2.2)$$

where $\rho(\mathbf{x}, t)$ is the microscopic charge density and $\mathbf{e}(\mathbf{x}, t)$ is the microscopic electric field at position \mathbf{x} and time t . The microscopic charge density $\rho^m(\mathbf{x}, t)$ is given by

$$\rho^m(\mathbf{x}, t) = \sum_{f=1}^{N_f} q_f \delta(\mathbf{x} - \mathbf{x}_f) + \sum_{m=1}^{N_m} \left(\sum_{n=1}^{N_n^m} q_n^m \delta(\mathbf{x} - \mathbf{x}_n^m) \right), \quad (2.3)$$

where $\delta(\cdot)$ is the dirac-delta function, N_f is the number of free charges, and N_m and N_n^m are the number of molecules and number of charges in molecule m , respectively. Here, q_f is the free charge of atom f and q_n^m is the charge of atom n corresponding to the molecule m .

The macroscopic Maxwell's equation is given by,

$$\nabla \cdot \mathbf{D}(\mathbf{y}, t) = \rho_f^M(\mathbf{y}, t), \quad (2.4)$$

where $\mathbf{D}(\mathbf{y}, t)$ is the macroscopic electric displacement vector and $\rho_f^M(\mathbf{y}, t)$ is the macroscopic free-charge density at the spatial point \mathbf{y} and time t . Note that usually the macroscopic free-charge density $\rho_f^M(\mathbf{y}, t)$ excludes the solvent charges.

To obtain an equivalent macroscopic electrostatic equation starting from the microscopic counterpart, an explicit expression between the charge densities at the two scales needs to be established. To this end, since charge is an extensive quantity, the macroscopic total (free and bound) charge density $\rho^M(\mathbf{y}, t)$ at the macroscale \mathbf{y} may be defined as

$$\rho^M(\mathbf{y}, t) \equiv \int_{\Gamma} \int_{\mathcal{R}} \rho(\mathbf{x}, t) \Delta(\mathbf{y} - \mathbf{x}) f(\Gamma, t) d\mathbf{x} d\Gamma, \quad (2.5)$$

where the integrals are performed over the entire phase-space Γ and volume \mathcal{R} , respectively. Here, $\Delta(\mathbf{y} - \mathbf{x})$ is a coarse-graining function which quantifies the contribution of the charge at \mathbf{x} in the point-wise definition of the macroscopic charge density at \mathbf{y} . Note that the $\Delta(\cdot)$ is different from $\delta(\cdot)$ in (2.3). In other words, the relation (2.5) states that the macroscopic charge in a small volume around the continuum point is the weighted-sum of enclosed individual charges. The coarse-graining function $\Delta(\mathbf{y} - \mathbf{x})$ is assumed to have the following properties: (i) $\int_{\mathcal{R}} \Delta(\mathbf{y} - \mathbf{x}) d\mathbf{x} =$

1, (ii) $\ell_m \ll \text{supp} \Delta \ll \mathcal{R}$, where ‘‘supp’’ denotes the support of a function and ℓ_m is the characteristic microstructural length, which in this case refers to the spacing between individual atoms, (iii) $\Delta(\mathbf{y} - \mathbf{x}) = 0$ on $\partial \mathcal{R}$ when $\mathbf{y} \in \mathcal{R}$, where $\partial \mathcal{R}$ denotes the boundary of the system and (iv) $\Delta(\mathbf{y} - \mathbf{x})$ attains a maximum when $\mathbf{x} = \mathbf{y}$ [89]. Assumption (i) is a standard normalization condition that enforces consistency of the relation (2.5). Also, assumptions (ii) and (iv) signify the local nature of the macroscopic quantities, while assumption (iii) implies that $\Delta(\mathbf{y} - \mathbf{x})$ effects only interior volumetric averaging. Since the coarse-graining function is dependent on the variable $\mathbf{y} - \mathbf{x}$, it can be proved that

$$\frac{\partial}{\partial \mathbf{x}} \Delta(\mathbf{y} - \mathbf{x}) = -\frac{\partial}{\partial \mathbf{y}} \Delta(\mathbf{y} - \mathbf{x}). \quad (2.6)$$

Finally, it should be noted that the time scale of change in the macroscopic charge density is considerably smaller than the time scale involved in the changes of the microscopic charge density because of the spatial and ensemble averaging [66].

Using (2.5) and the definition of the microscopic charge density $\rho^m(\mathbf{x}, t)$ given in (2.3), the total macroscopic charge density is given by

$$\rho^M(\mathbf{y}, t) = \int_{\Gamma} \left(\sum_{f=1}^{N_f} q_f \Delta(\mathbf{y} - \mathbf{x}_f) + \sum_{m=1}^{N_m} \left(\sum_{n=1}^{N_n^m} q_n^m \Delta(\mathbf{y} - \mathbf{x}_n^m) \right) \right) f(\Gamma, t) d\Gamma \quad (2.7)$$

Now, following the procedure described in [55], let the position of the center of mass of a molecule be denoted by \mathbf{x}_m and the relative position of the charge q_n^m with respect to the center of mass be defined as $\mathbf{x}_{nm} \equiv \mathbf{x}_n^m - \mathbf{x}_m$. Using these definitions and rewriting the weighting function $\Delta(\mathbf{y} - \mathbf{x}_n^m)$ in terms of the center of mass coordinate, equation (2.7) becomes

$$\rho^M(\mathbf{y}, t) = \int_{\Gamma} \left(\sum_{f=1}^{N_f} q_f \Delta(\mathbf{y} - \mathbf{x}_f) + \sum_{m=1}^{N_m} \left(\sum_{n=1}^{N_n^m} q_n^m \Delta(\mathbf{y} - \mathbf{x}_m - \mathbf{x}_{nm}) \right) \right) f(\Gamma, t) d\Gamma. \quad (2.8)$$

Employing Taylor series expansion of $\Delta(\mathbf{y} - \mathbf{x}_m - \mathbf{x}_{nm})$ about $\mathbf{y} - \mathbf{x}_m$, equation (2.8) can be expressed as an infinite sum:

$$\begin{aligned} \rho^M(\mathbf{y}, t) &= \int_{\Gamma} \left(\sum_{f=1}^{N_f} q_f \Delta(\mathbf{y} - \mathbf{x}_f) + \sum_{m=1}^{N_m} \left(\sum_{n=1}^{N_n^m} q_n^m \Delta(\mathbf{y} - \mathbf{x}_m) - \sum_{n=1}^{N_n^m} q_n^m \mathbf{x}_{nm} \cdot \frac{\partial}{\partial \mathbf{y}} \Delta(\mathbf{y} - \mathbf{x}_m) \right. \right. \\ &\quad \left. \left. + \sum_{n=1}^{N_n^m} q_n^m \frac{\mathbf{x}_{nm} \otimes \mathbf{x}_{nm}}{2!} \cdot \frac{\partial}{\partial \mathbf{y}} \frac{\partial}{\partial \mathbf{y}} \Delta(\mathbf{y} - \mathbf{x}_m) + \dots \right) \right) f(\Gamma, t) d\Gamma \\ &= \int_{\Gamma} \left[\sum_{f=1}^{N_f} q_f \Delta(\mathbf{y} - \mathbf{x}_f) + \sum_{m=1}^{N_m} \left(\sum_{n=1}^{N_n^m} q_n^m \Delta(\mathbf{y} - \mathbf{x}_m) \right) \right] f(\Gamma, t) d\Gamma \\ &\quad + \frac{\partial}{\partial \mathbf{y}} \cdot \left(\int_{\Gamma} \left(- \sum_{m=1}^{N_m} \sum_{n=1}^{N_n^m} q_n^m \mathbf{x}_{nm} \Delta(\mathbf{y} - \mathbf{x}_m) + \right. \right. \\ &\quad \left. \left. \sum_{m=1}^{N_m} \sum_{n=1}^{N_n^m} q_n^m \frac{\mathbf{x}_{nm} \otimes \mathbf{x}_{nm}}{2!} \cdot \frac{\partial}{\partial \mathbf{y}} \Delta(\mathbf{y} - \mathbf{x}_m) + \dots \right) f(\Gamma, t) d\Gamma \right), \end{aligned} \quad (2.9)$$

where it can be seen that the first integral term on the right hand side of the second equality is equivalent to the macroscopic free charge density $\rho_f^M(\mathbf{y}, t)$.

Next, to obtain the macroscopic Maxwell's equation (2.4), one needs to coarse-grain the microscopic electrostatic equation (2.2). To this end, multiplying (2.2) with the coarse-graining function $\Delta(\mathbf{y} - \mathbf{x})$, integrating over the whole system \mathcal{R} , and taking the ensemble average yields

$$\int_{\Gamma} \int_{\mathcal{R}} \frac{\partial}{\partial \mathbf{x}} \cdot (\epsilon_0 \mathbf{e}(\mathbf{x}, t)) \Delta(\mathbf{y} - \mathbf{x}) f(\Gamma, t) \, d\mathbf{x} d\Gamma = \int_{\Gamma} \int_{\mathcal{R}} \rho^m(\mathbf{x}, t) \Delta(\mathbf{y} - \mathbf{x}) f(\Gamma, t) \, d\mathbf{x} d\Gamma. \quad (2.10)$$

The left hand side of (2.10) can be rewritten as

$$\begin{aligned} \int_{\Gamma} \int_{\mathcal{R}} \frac{\partial}{\partial \mathbf{x}} \cdot (\epsilon_0 \mathbf{e}(\mathbf{x}, t)) \Delta(\mathbf{y} - \mathbf{x}) f(\Gamma, t) \, d\mathbf{x} d\Gamma &= \int_{\mathcal{R}} \int_{\Gamma} \frac{\partial}{\partial \mathbf{x}} \cdot (\epsilon_0 \mathbf{e}(\mathbf{x}, t) \Delta(\mathbf{y} - \mathbf{x})) f(\Gamma, t) \, d\Gamma d\mathbf{x} \\ &\quad - \int_{\Gamma} \int_{\mathcal{R}} \epsilon_0 \mathbf{e}(\mathbf{x}, t) \cdot \frac{\partial}{\partial \mathbf{x}} \Delta(\mathbf{y} - \mathbf{x}) f(\Gamma, t) \, d\mathbf{x} d\Gamma \\ &= \int_{\partial \mathcal{R}} \int_{\Gamma} \epsilon_0 \mathbf{e}(\mathbf{x}, t) \cdot \mathbf{n} \Delta(\mathbf{y} - \mathbf{x}) f(\Gamma, t) \, d\Gamma d\mathbf{x} + \int_{\Gamma} \int_{\mathcal{R}} \epsilon_0 \mathbf{e}(\mathbf{x}, t) \cdot \frac{\partial}{\partial \mathbf{y}} \Delta(\mathbf{y} - \mathbf{x}) f(\Gamma, t) \, d\mathbf{x} d\Gamma \\ &= \frac{\partial}{\partial \mathbf{y}} \cdot \left(\epsilon_0 \int_{\Gamma} \int_{\mathcal{R}} \mathbf{e}(\mathbf{x}, t) \Delta(\mathbf{y} - \mathbf{x}) f(\Gamma, t) \, d\mathbf{x} d\Gamma \right), \end{aligned} \quad (2.11)$$

where the second equality is obtained by divergence theorem and property (2.6) and the third equality is obtained by employing assumption (iii) of the coarse-graining function.

Using (2.9) and (2.11), equation (2.10) can be reduced to

$$\begin{aligned} &\frac{\partial}{\partial \mathbf{y}} \cdot \left(\epsilon_0 \int_{\Gamma} \int_{\mathcal{R}} \mathbf{e}(\mathbf{x}, t) \Delta(\mathbf{y} - \mathbf{x}) f(\Gamma, t) \, d\mathbf{x} d\Gamma + \right. \\ &\left. \int_{\Gamma} \left(\sum_{m=1}^{N_m} \sum_{n=1}^{N_n^m} q_n^m \mathbf{x}_{nm} \Delta(\mathbf{y} - \mathbf{x}_m) - \sum_{m=1}^{N_m} \sum_{n=1}^{N_n^m} q_n^m \frac{\mathbf{x}_{nm} \otimes \mathbf{x}_{nm}}{2!} \cdot \frac{\partial}{\partial \mathbf{y}} \Delta(\mathbf{y} - \mathbf{x}_m) + \dots \right) f(\Gamma, t) \, d\Gamma \right) \\ &= \int_{\Gamma} \left[\sum_{f=1}^{N_f} q_f \Delta(\mathbf{y} - \mathbf{x}_f) + \sum_{m=1}^{N_m} \left(\sum_{n=1}^{N_n^m} q_n^m \Delta(\mathbf{y} - \mathbf{x}_m) \right) \right] f(\Gamma, t) \, d\Gamma = \rho_f^M(\mathbf{y}, t). \end{aligned} \quad (2.12)$$

Comparing equations (2.12) and (2.4), the electric displacement vector \mathbf{D} can be obtained as

$$\begin{aligned} \mathbf{D}(\mathbf{y}, t) &= \epsilon_0 \int_{\Gamma} \int_{\mathcal{R}} \mathbf{e}(\mathbf{x}, t) \Delta(\mathbf{y} - \mathbf{x}) f(\Gamma, t) \, d\mathbf{x} d\Gamma + \\ &\int_{\Gamma} \left(\sum_{m=1}^{N_m} \sum_{n=1}^{N_n^m} q_n^m \mathbf{x}_{nm} \Delta(\mathbf{y} - \mathbf{x}_m) - \sum_{m=1}^{N_m} \sum_{n=1}^{N_n^m} q_n^m \frac{\mathbf{x}_{nm} \otimes \mathbf{x}_{nm}}{2!} \cdot \frac{\partial}{\partial \mathbf{x}} \Delta(\mathbf{y} - \mathbf{x}_m) + \dots \right) f(\Gamma, t) \, d\Gamma \end{aligned} \quad (2.13)$$

Defining the macroscopic electric field $\mathbf{E}(\mathbf{y}, t)$ at the macroscale to be a spatial and ensemble average of the microscopic electric field,

$$\mathbf{E}(\mathbf{y}, t) \equiv \int_{\Gamma} \int_{\mathcal{R}} \mathbf{e}(\mathbf{x}, t) \Delta(\mathbf{y} - \mathbf{x}) f(\Gamma, t) \, d\mathbf{x} d\Gamma, \quad (2.14)$$

the electric displacement vector \mathbf{D} can be reduced to

$$\mathbf{D}(\mathbf{y}, t) = \epsilon_0 \mathbf{E}(\mathbf{y}, t) + \int_{\Gamma} \left(\sum_{m=1}^{N_m} \mathbf{p}_m \Delta(\mathbf{y} - \mathbf{x}_m) - \frac{\partial}{\partial \mathbf{y}} \cdot \sum_{m=1}^{N_m} \left(\mathbf{q}_m \Delta(\mathbf{y} - \mathbf{x}_m) \right) + \dots \right) f(\Gamma, t) d\Gamma, \quad (2.15)$$

where $\mathbf{p}_m = \sum_{n=1}^{N_n^m} q_n^m \mathbf{x}_{nm}$ and $\mathbf{q}_m = \sum_{n=1}^{N_n^m} q_n^m \frac{\mathbf{x}_{nm} \otimes \mathbf{x}_{nm}}{2!}$ are the molecular dipole and quadrupole moments of molecule m , respectively. Using the relation $\mathbf{D} = \epsilon_0 \mathbf{E} + \mathbf{P}$, the macroscopic polarization vector $\mathbf{P}(\mathbf{y}, t)$ is given by

$$\mathbf{P}(\mathbf{y}, t) = \int_{\Gamma} \left(\sum_{m=1}^{N_m} \mathbf{p}_m \Delta(\mathbf{y} - \mathbf{x}_m) - \frac{\partial}{\partial \mathbf{y}} \cdot \sum_{m=1}^{N_m} \left(\mathbf{q}_m \Delta(\mathbf{y} - \mathbf{x}_m) \right) + \dots \right) f(\Gamma, t) d\Gamma. \quad (2.16)$$

It can be seen from equation (2.16) that the macroscopic polarization vector contains contributions from the molecular dipole, quadrupole, and higher order moments. For solvents consisting only of dipoles in their bulk state, e.g. water, the contribution of dipole moments to the polarization density is larger than that of the quadrupole moments. However, molecules can have no net dipole moment but have a quadrupole moment which constitutes the main component of the polarization density and hence the dielectric constant, such as a square with alternating positive and negative charges at the vertices. Benzene is a real example of a molecule where the quadrupole moment contributes significantly. Also, the accuracy of the macroscopic polarization vector depends on the order of the polynomial used for the coarse-graining function. For example, if one uses a constant coarse-graining function then only the dipole moments can be recovered. Similarly, if the coarse-graining function is linear then the quadrupole moments may further be computed. MD simulations in this paper are limited to constant and linear coarse-graining functions.

2.3 Computational Framework

All MD simulations in this paper are performed using the LAMMPS software [106] and its Atomistic-to-Continuum (AtC) package [137]. The AtC method can be used to calculate spatial descriptions of the continuum variables such as stress, temperature, mass density, *etc.* In order to calculate these variables at various continuum points, the whole volume is subdivided into smaller regions, similar to the concept of a mesh in the Finite Element Method [137]. The mesh size may be chosen depending on the desired spatial resolution of the variables. Finally, the variables are calculated at the nodal points using coarse-graining functions centered at these points. This method in conjunction with MD simulations can perform only per-atom calculations and therefore can compute variables expressed in terms of per-atom quantities. However, the polarization density in (2.16) is expressed as a sum of per-molecule quantities. For this paper, the AtC method in [137] is extended to perform the per-molecule computations. Since the size of the system and therefore the total number of molecules required to obtain the polarization density are large, a novel parallelization strategy is presented which can efficiently perform the per-molecule computations.

The new approach developed in this work is specifically designed to scale for large collections of small molecules nearly as efficiently as established coarse-graining does for atomic quantities.

In MD simulations, molecules are often defined with bond lists that contain for each atom all the other atoms to which it is bonded. MD simulations also maintain lists of ghost atoms on each processor based on a user-specified cutoff radius (usually that of the interatomic potential) to account for the interactions with off-processor atoms. It is these data structures which are leveraged to create representations of molecules as collections of atoms (herein referred to as a molecule list), such that the sum over molecules and sum over atoms in a molecule (see (2.3)) may be computed using the following algorithm. When beginning to construct the molecule list, each atom is marked as unfound and the first local, *i.e.* non-ghost, atom on a processor, is placed in a first-in/first-out queue [21]. The algorithm gets the first atom in the queue and traverses its bond list, marking each atom as found and enqueueing it as it is discovered. This process is repeated until the queue is empty, including processor ghosts. A molecule is then defined as the collection of those atoms which were enqueued. The process repeats by placing the next unfound atom in another queue until all local atoms are marked as found. At this point, all molecules are characterized as local to a processor when at least one atom in the molecule is a local atom. Note this algorithm defines a “small” molecule such that the maximum distance between any two atoms is less than the cutoff radius, which guarantees that if a molecule contains at least one local atom then all the atoms in that molecule are either local or ghost atoms.

Until this point only the atom and bond lists were needed to construct the molecule list. Therefore, updating the local molecule list is only required when atoms are exchanged across processors, thereby requiring no additional parallel communication. To compute the correct coarse-grained quantities without incurring additional communication operations, the coarse-graining function in (2.8) is scaled by the fraction of local atoms in the molecule on the present processor. A final sum over all processors is required to assemble the molecular data into the coarse-grained continuum fields. However, this summation is also necessary even for strictly atomic data. With these operations, the run time scales as

$$\mathcal{O}((N_n^m N_m + N_c N_m) / N_p + N_c N_p), \quad (2.17)$$

with the notation N_p for number of processors and N_c for number of coarse-graining nodes. The first term represents operations which scale in parallel, while the second is associated with summation across all processors. Costs arising from accessing processor ghosts are neglected, assuming a dense system with $N_m \gg N_p$. A derivation of this result is provided in Appendix 2.6, as well as a comparison with existing molecular computes in LAMMPS. Efficiency is realized because there are significantly fewer coarse-graining points than atoms or molecules, and parallel data exchange is only applied to arrays of size equal to the number of continuum sample points. Thus, no additional processor communication is needed beyond that which already occurs in MD and AtC simulations. Redundant operations are only performed on the subset of molecules crossing processor boundaries. In this paper, this algorithm is applied to bulk water and an electrolyte solution using up to 64 processors.

2.4 Applications to Small Polar Molecules

2.4.1 Bulk Water

To verify the theory and software implementation, the proposed method is applied to calculate the bulk permittivity of water at a temperature of 300K and a density of $1000 \text{ kg}/\text{m}^3$. Water is modeled using the TIP3P interaction potential with its parameters given in [108]. Simulations are performed in a volume of $50\text{\AA} \times 50\text{\AA} \times 42.6919\text{\AA}$, consisting of 3158 molecules. The time-step is chosen to be 0.5 fs . Bond length and angle constraints for the water molecule are maintained using the SHAKE algorithm [116]. Lennard-Jones and short-range Coulombic forces are calculated using a cut-off radius of 13\AA . Long-range electrostatic forces are calculated using the PPPM method [45] with slab geometry [133]. Periodic boundary conditions are applied in the x and y directions whereas non-periodic boundary conditions are applied in the z direction. Boundaries in the z direction are modeled using unstructured walls governed by 10-4-3 Lennard-Jones interaction potential, where the characteristic distance and the characteristic energy are chosen to be 3.1507\AA and 0.1351 eV , respectively [87].

Simulations are performed under various external electric fields $\mathbf{E}_e = (0, 0, E_{ez})$ in the z -direction by adding the electrostatic force $q_i \mathbf{E}_{ext}$ to the total force on atom i . The system is initially equilibrated using a Nosé-Hoover thermostat [48] to maintain a temperature of 300K. Once the system reaches a steady state for a given external electric field, the resultant electric field $\mathbf{E} = (0, 0, E_z)$ at every microscopic point inside the system is obtained by applying Gauss' law in the z direction. This resultant electric field E_z is lesser in magnitude than the external field due to the alignment of water molecules under the action of the imposed field. Finally, the polarization vector is calculated at the center of the system by using (2.16), with constant and linear coarse-graining functions given by

$$\Delta(\mathbf{x} - \mathbf{x}_n) = \begin{cases} \frac{1}{2L_x L_y L}, & \text{if } |z - z_n| < L \\ 0, & \text{else} \end{cases} \quad (2.18)$$

and

$$\Delta(\mathbf{x} - \mathbf{x}_n) = \begin{cases} \frac{1}{LL_x L_y} \left(\frac{L - |z - z_n|}{L} \right), & \text{if } |z - z_n| < L \\ 0, & \text{else} \end{cases} \quad (2.19)$$

respectively. Here, L denotes the size of the averaging volume around a macroscopic point in the z direction, and L_x and L_y are the total lengths of the system in the x and y directions, respectively. It should be noted that the choice of center of the system for evaluating the polarization density is made so that assumption (iii) of the coarse-graining function is satisfied.

Using a constant coarse-graining function (2.18) to obtain the macroscopic polarization density includes contribution only from molecular dipole moments, as mentioned in Section 2.2. For this case, Figure 2.1 shows the running time-average of the polarization vector in the z direction at the center of box for various averaging volumes corresponding to $L = \{1\text{\AA}, 2\text{\AA}, 3\text{\AA}, 4\text{\AA}, 5\text{\AA}\}$ and external electric field of $E_{ez} = -0.72 \text{ V}/\text{\AA}$. It can be seen from Figure 2.1 that the polarization vector converges to a non-zero value for all averaging volumes, albeit more quickly for the larger

averaging volumes. Therefore, a region around the center can be defined as the bulk region where the polarization vector is a constant value.

It is already noted in Section 2.2 that by using a linear coarse-graining function given by equation (2.19), the polarization density consists of not only the molecular dipole moments but also the molecular quadrupole moments. In this case, Figure 2.2 shows the running time-average of the dipole and quadrupole moments at the center of the system for an averaging volume corresponding to $L = 5\text{\AA}$. It can be seen that the dipole moment contributions from the linear coarse-graining function is practically equal to the dipole moments from a constant coarse-graining function. Importantly, the contribution from the quadrupole moments is practically zero. This shows that the macroscopic polarization density is independent of the choice of coarse-graining function when one averages over a sufficiently large volume.

Finally, Figure 2.3 shows the relationship between the macroscopic polarization and the resultant electric field for a range of externally applied fields \mathbf{E}_{ext} . In every case, the polarization vector and the resultant electric fields are calculated using an averaging volume corresponding to $L = 5\text{\AA}$ at the center of the box. The dielectric constant of water $\epsilon = 1 + \chi_e$ is found to be 72 ± 3 , which is in agreement with the values obtained in [108]. It should be noted that the dielectric constant obtained using the polarization density is approximately the same as the ratio of the externally applied field to the resultant electric field in the linear range, which is found to be 79 ± 8 . Also, note that in calculating the dielectric constant of, for example, benzene, where the quadrupole moment contribution is significant, a similar procedure described in this section can be followed. In this case, at least a linear coarse-graining function should be used so that the quadrupole moments can be captured. The resultant bulk polarization density will not depend on the choice of the coarse-graining function when the averaging volume is sufficiently large, thereby yielding a size independent dielectric constant.

Another important example where quadrupole moments are of interest is the behavior of water at an interface. Specifically, it is hypothesized that the surface potential and dielectric constants contain significant contributions from the quadrupole moment [61, 60, 13]. However, to the best of our knowledge, there are no direct quantitative results explicitly showing the contribution of quadrupole moments in comparison with the dipole moments. The theoretical and computational procedure described in this paper enables such a direct calculation of the contributions of individual moments to the polarization vector. Figure 2.4 shows the spatial dipole and quadrupole moments across the length of the channel calculated using the first $\left(\int_{\Gamma} \sum_{m=1}^{N_m} \mathbf{p}_m \Delta(\mathbf{y} - \mathbf{x}_m) d\Gamma \right)$ and second $\left(\int_{\Gamma} \frac{\partial}{\partial \mathbf{y}} \cdot \sum_{m=1}^{N_m} \left(\mathbf{q}_m \Delta(\mathbf{y} - \mathbf{x}_m) \right) f(\Gamma, t) d\Gamma \right)$ terms of (2.16), respectively. A linear coarse-graining function (2.19) and an averaging window corresponding to $L = 0.05\text{\AA}$ are used. It can be seen in Figure 2.4 that the quadrupole moment is practically zero in the bulk region away from the interfaces. However, it is significant and non-zero close to both walls. Specifically, close to the left wall, which is similar to an interface with a negative charge, the quadrupole moment contribution to the polarization vector is in the direction opposite to the dipole moment. At the right wall, which is similar to an interface with positive charge, the quadrupole contribution is in the same

direction as the dipole densities. Note that the resultant polarization vector (2.16) is the dipole moment minus the quadrupole moment when the higher order terms are negligible. Using only the dipole and the quadrupole moments, the resultant polarization vector in the z direction is shown in Figure 2.5, where the density at the interface is significantly different from the bulk. Note that in resolving the peaks corresponding to the dipole and quadrupole moments close to the interface, it is important to use a sufficiently small averaging volume. If a large averaging volume is used, the resulting moments are excessively smeared and depend on the averaging volume. Moreover, for large averaging volumes, the assumption (iii) of the coarse-graining function is not satisfied and the calculated moments lack clear physical meaning close to the interface.

2.4.2 Solid Liquid Interface – Electrical Double Layer

To demonstrate the method in an intended application, the theory and the computational framework discussed in Sections 2.2 and 2.3 are applied to evaluate the spatially-varying polarization vector in systems with electrolyte solutions where EDLs are formed at a charged surface. As our goal is to study solvent effects in EDLs, a nanochannel with bounded walls in the z direction is chosen. The walls have equal and opposite surface charge of $0.12872 C/m^2$, which creates an external electric field in the interior of the system. The system consists of a 1:1 electrolyte fluid with water as the solvent. The width of the channel in the z direction is chosen so that the EDLs near the walls do not overlap creating a sufficiently large bulk region around the center of the system. Periodic boundary conditions are used in the x and y directions. Walls in the z direction are modeled as unstructured walls using the 10-4-3 Lennard-Jones interaction potential, as in the case of bulk water in Section 2.4.1. Ion concentration and water density in the bulk region are targeted to be $100 mM$ and $1000 kg/m^3$, respectively, while the temperature is held at $300K$ using the Nosé-Hoover thermostat. The Debye length of this system is approximately $1 nm$. The size of the simulated system is $25\text{\AA} \times 25\text{\AA} \times 150\text{\AA}$ consisting of 3120 water molecules, 10 positive and 10 negative ions. All the water molecules are modeled by TIP3P interaction potential as in the case of bulk water. All the ions are modeled using Lennard-Jones interaction potential where the characteristic energy and characteristic lengths are chosen to be that of the oxygen atom in the TIP3P interaction potential. The masses of the positive and negative ion are chosen to be $39.0983 g/mol$ and $35.4530 g/mol$, respectively. The simulations are carried out at a timestep of $0.5 fs$. Once the system reaches a steady state for the given surface charge, the polarization vector and the resultant electric field are evaluated as a function of space between the walls.

Figure 2.6 shows the z polarization density calculated using the constant coarse-graining function (2.18) for various averaging volumes corresponding to $L = \{0.05\text{\AA}, 0.1\text{\AA}, 0.5\text{\AA}, 1\text{\AA}, 2\text{\AA}, 4\text{\AA}\}$. The polarization values are obtained by time and ensemble averaging using five independent simulations corresponding to different initial conditions, each containing data from 10 million timesteps. It can be seen that the polarization density is non-zero very close to the walls and decays to zero towards the center of the system, which is expected since the electric field is completely screened by the ions present in the electrolytic solution. Figure 2.7 shows the polarization density close to the wall with negative surface charge. This zoom-in shows that for a short distance from the wall, the polarization density depends on the size of the averaging volume. This might be due

to the following reasons: (a) specific structure of the solvent at the surface, or (b) assumption (iii) of the coarse-graining function $\Delta(\mathbf{x} - \mathbf{y})$, which is used for obtaining (2.11), is not satisfied as one moves closer to the surface. However, beyond approximately 10\AA , the polarization density ceases to depend on the size of the averaging volume indicating an intermediate asymptotic length scale, where intensive material properties may be identified [7, 127]. More generally, for each intermediate asymptotic scale, the intensive variables at that scale are governed by a unique continuum or mean-field theory [7]. It can be seen in Figure 2.7 that the Poisson-Boltzmann mean-field theory matches well with the simulation results only in that part of the region where there exists an intermediate asymptotic length scale. This region is typically referred to as the diffuse layer [63]. The region between the wall and the diffuse layer is a combination of Stern and condensed layers [63]. The Stern layer is mainly due to adsorption effects adjacent to the surface. The condensed layer is mainly due to steric packing of ions adjacent to the Stern layer usually at moderate to high surface charges [63]. Therefore, by analyzing just the polarization vector, one may identify the length scales of layers with different physical effects in the composite EDL, making it a valuable tool for using MD simulations to guide design of new double layer models.

Another advantage of the present method is that the macroscopic polarization density is much easier to analyze than total resultant electric fields. For example, Figure 2.8 shows the resultant electric field calculated using Gauss' law along the width of the channel. The electric field values are obtained by time and ensemble averaging using 10 different simulations each consisting of 10 million timesteps, which is expensive compared to the polarization vector calculations. It can be seen from Figure 2.9 that the electric field oscillates between positive and negative values making it difficult to distinguish the length scales of the diffuse layer, where Poisson-Boltzmann theory is valid, from the condensed layer close to the surface. Additionally, the electric field values are not calculated accurately in the diffuse layer. On the other hand, the polarization vector yields information about these layers with lower computational cost.

2.5 Discussion

In this paper, a theoretical and computational framework for evaluating polarization vectors from MD simulations is presented by coarse-graining the microscopic charge density and electrostatic equation. It is shown that the polarization vector can be calculated to desired accuracy by means of changing the degree of coarse-graining function. It is also shown that the polarization vector is more amenable for analyzing electric double layers than electric fields, due to the poor signal-to-noise ratio involved in obtaining the local electric fields resulting from high dielectric constants. Specifically, it is shown that the higher order terms such as quadrupole moments are non-zero and significant in their contribution to the total polarization vector.

The computational framework presented in this paper will be applied to: (i) identify the contributions of other higher order terms such as octupole moments *etc.*, close to interfaces and (ii) identify length scales of compact and diffuse layers in any electrical double layer for relevant values of concentrations of solutions and surface charge densities. This will aid in multiscale electrical double layer simulations, which can guide design of new theories, where the length scales

corresponding to the Stern and condensed layers can be modeled by explicit molecular dynamics simulations, and continuum simulations can be used to model the diffuse layer and the bulk.

2.6 Run-Time Cost Estimate for Molecular Coarse-Graining Algorithm

The execution time associated with the molecular coarse-graining algorithm used in this work can be analyzed by considering the individual operations required by each sub-computation. Algorithm 1 shows the three main parts of the algorithm. The first two parts are performed locally on each processor, while the third part requires summation across all processors to obtain the polarization density at each coarse-graining node (the notation $|_l$ and $|_g$ denote local and global data, respectively). Total operations associated with the first two loops are $N_m N_n^m$ and $N_m N_c$, respectively. Because these loops act on distributed data, they will be inversely proportional to N_p as long as the number of molecules crossing processors is small which holds when $N_m \gg N_p$; a reasonable assumption for a set of dense molecules. Overall, the execution time scales as

$$\mathcal{O}(N_n^m N_m / N_p + N_c N_m / N_p + N_c N_p) \quad (2.20)$$

The key assumption making this algorithm attractive is that the vast majority of atoms are associated with small molecules, specifically $N_n^m \sim \mathcal{O}(1)$ and $N_n^m N_m \sim N_a$, N_a being the number of atoms. Parallel performance is then a byproduct of the underlying MD code's scalability. With this assumption, Algorithm 1 has run-time scaling of

$$\mathcal{O}(N_a(1 + N_c) / N_p + N_c N_p). \quad (2.21)$$

Advantages of Algorithm 1 for evaluating properties for large sets of small molecules can be seen in comparison to Algorithm 2, which implements the same functionality using existing per-molecule computations in LAMMPS. To the best of the authors' knowledge, these per-molecule algorithms represent the state of the art in MD with a terminal addition of the coarse-graining operation. Some additional efficiency could be realized by incorporating the coarse-graining into the third loop, followed by the cross-processor summation of Algorithm 1 on coarse-graining nodes. However, the fundamental problem remains: loops over the global number of molecules on each processor. The run-time scaling for Algorithm 2 is

$$\mathcal{O}(N_m + N_a / N_p + N_m N_p + N_m N_c). \quad (2.22)$$

Comparing the performance of the two algorithms for cases relevant to this work is accomplished by bringing the appropriate assumptions: $N_m \sim N_a$ and $N_n^m, N_c \sim \mathcal{O}(1)$. With this added constraint, Algorithm 1 has a run-time cost scaling like

$$\mathcal{O}(N_a / N_p + N_p), \quad (2.23)$$

while Algorithm 2 scales as

$$\mathcal{O}(N_a / N_p + N_a + N_a N_p). \quad (2.24)$$

Cost differences in the algorithms are partly attributable to dissimilar approaches in cross-processor summation, in which Algorithm 1 scales as N_p in contrast to the more expensive $N_a N_p$ scaling of Algorithm 2. Furthermore, Algorithm 2 has a constant time penalty on the order of the number of atoms absent from Algorithm 1. This savings is achieved because Algorithm 1 can compute molecular properties in parallel, as opposed to replicating information for each molecule across all processors. For the cases of interest here, i.e., MD simulations where almost every atom is part of a small molecule, Algorithm 1 makes realization of the theory developed in this work possible for large systems.

Algorithm 1 Molecular Coarse-Graining

```

    ▷ Compute Dipole Moment for all Molecules, Performed in Parallel
for  $m = 1$  to  $N_m|_l$  do
     $\mathbf{p}_m = 0$ 
    for  $n = 1$  to  $N_n^m$  do
         $\mathbf{p}_m += q_n^m \mathbf{x}_{nm}$ 
    end for
end for
    ▷ Coarse-Grain Dipole Moment, Performed in Parallel

for  $c = 1$  to  $N_c|_g$  do
     $\mathbf{P}_c^p = 0$ 
    for  $m = 1$  to  $N_m|_l$  do
         $\mathbf{P}_c^p += \mathbf{p}_m \Delta(\mathbf{y}_c - \mathbf{x}_m)$ 
    end for
end for
    ▷ Cross-Processor Summation

for  $c = 1$  to  $N_c|_g$  do
     $\mathbf{P}_c = 0$ 
    for  $p = 1$  to  $N_p|_g$  do
         $\mathbf{P}_c += \mathbf{P}_c^p$ 
    end for
end for

```

Algorithm 2 Molecular Coarse-Graining Using LAMMPS Per-Molecule Computes

▷ Initialization for the Total Number of Molecules, Occurring on Each Processor

```
for  $m = 1$  to  $N_m|_g$  do  
     $\mathbf{p}_m = 0$   
end for
```

▷ Compute Dipole Moment Contributions from Local Atoms, Performed in Parallel

```
for  $a = 1$  to  $N_a|_l$  do  
     $m = \text{map from atom to molecule of } a$   
     $\mathbf{p}_m^+ = q_a \mathbf{x}_a$   
end for
```

▷ Cross-Processor Summation for each Molecule

```
for  $m = 1$  to  $N_m|_g$  do  
     $\mathbf{p}_m = 0$   
    for  $p = 1$  to  $N_p$  do  
         $\mathbf{p}_m^+ = \mathbf{p}_m^p$   
    end for  
end for
```

▷ Coarse-Grain Dipole Moment, Performed on a Single Processor

```
for  $c = 1$  to  $N_c$  do  
     $\mathbf{P}_c = 0$   
    for  $m = 1$  to  $N_m|_g$  do  
         $\mathbf{P}_c^+ = \mathbf{p}_m \Delta(\mathbf{y}_c - \mathbf{x}_m)$   
    end for  
end for
```

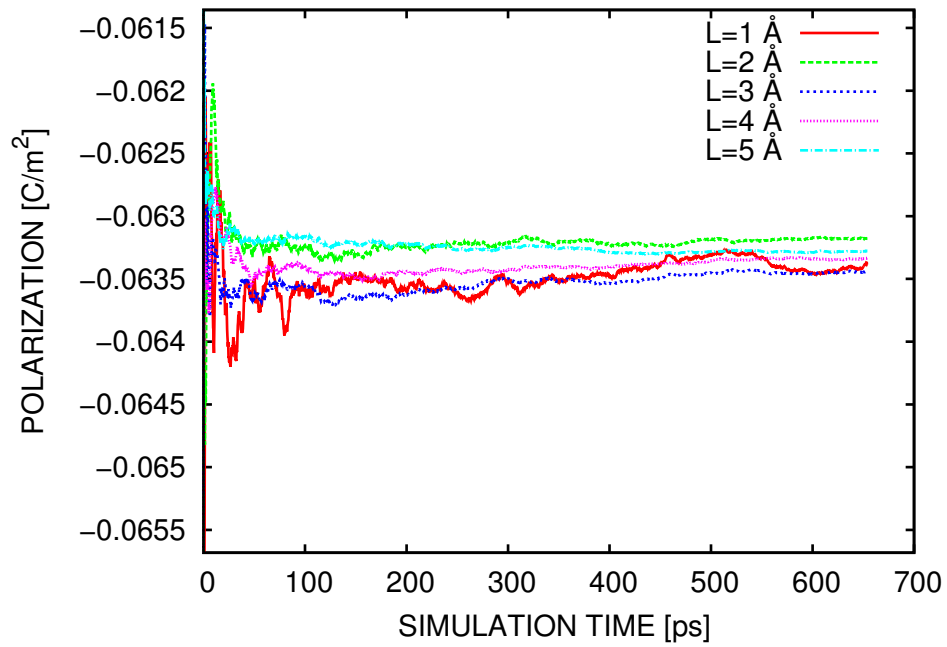
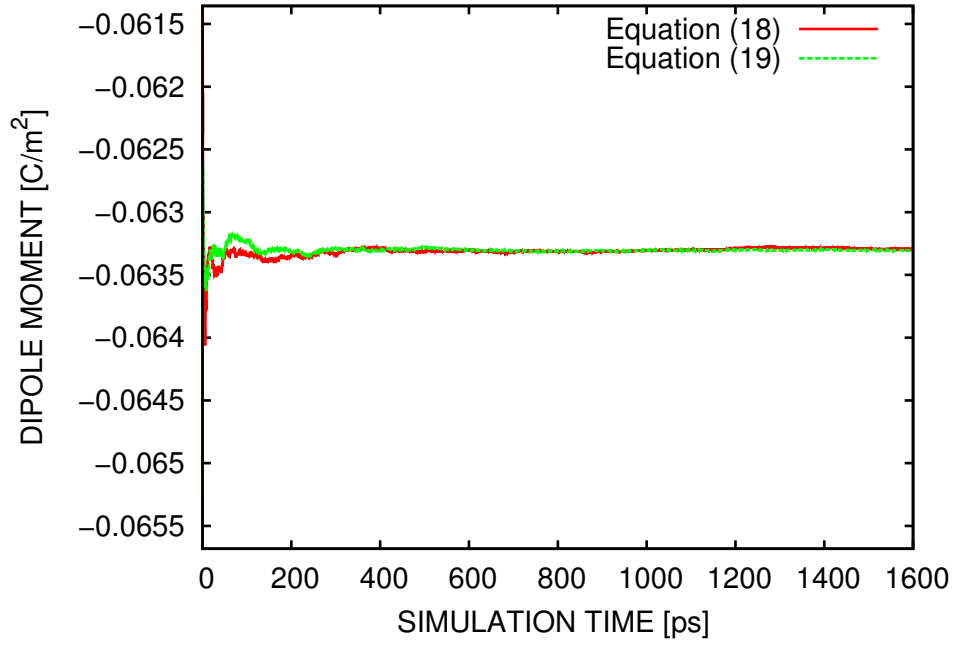
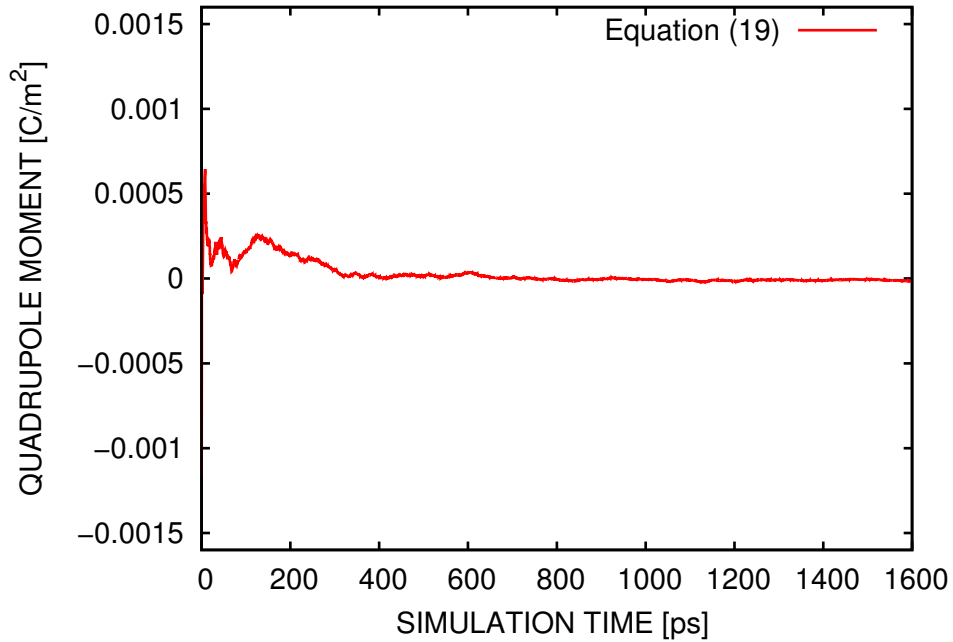


Figure 2.1. Bulk water: Running time-average of polarization vector in the z direction at the center of the system for several coarse-graining length scales and an applied electric field of $E_{ez} = -0.72 \text{ V}/\text{\AA}$ using a constant coarse-graining function (2.18).



(a) Average dipole moment



(b) Average quadrupole moment

Figure 2.2. Bulk water: Running time-average of the dipole and quadrupole moment contributions to the total polarization vector in the z direction at the center of the system for an applied electric field of $E_{ez} = -0.72 \text{ V/\AA}$ and a coarse-graining length of 5 \AA using constant and linear coarse-graining functions given by (2.18) and (2.19), respectively.

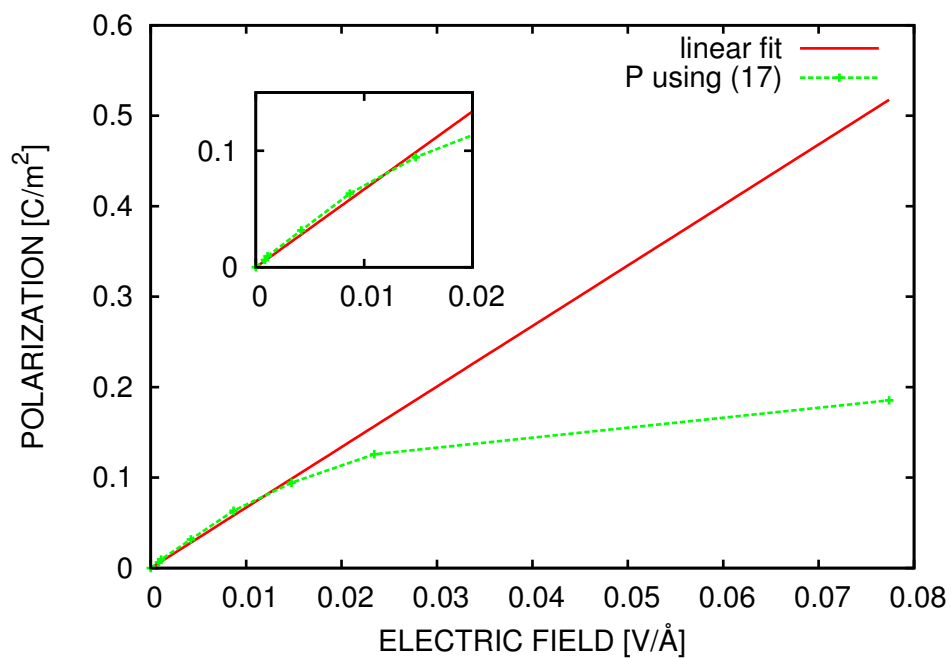


Figure 2.3. Bulk water: Magnitude of Polarization as a function of magnitude of local electric field. The solid red line shows a linear fit to the data in the range where polarization varies linearly with local electric field. The dielectric susceptibility constant which is the slope of the linear fit is found to be $\chi_e = 71 \pm 3$. Inset shows the range where the polarization density is linearly proportional to the resultant electric field.

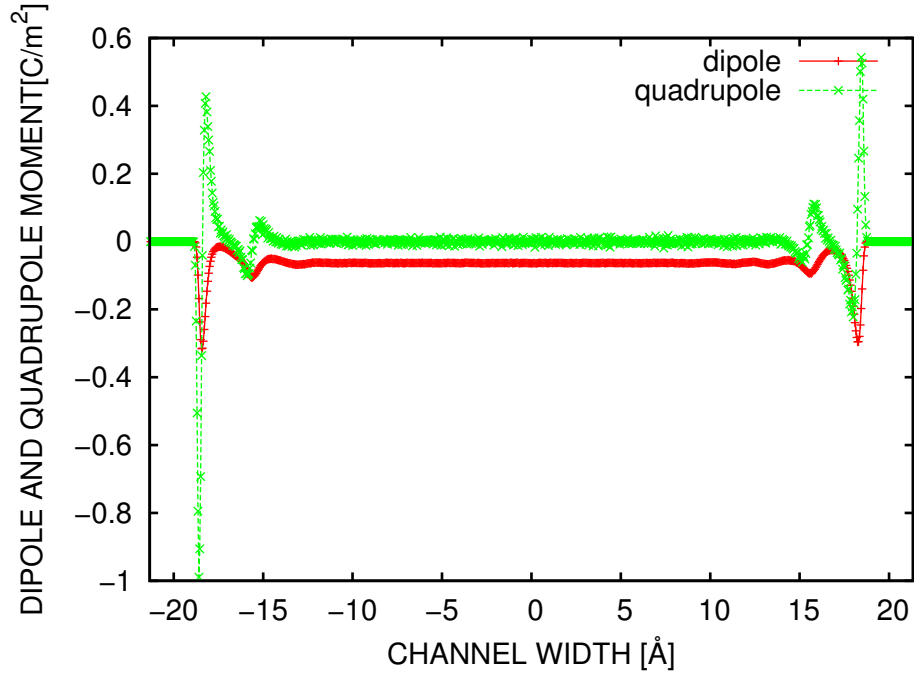


Figure 2.4. Bulk water: Spatially varying dipole $\left(\int_{\Gamma} \sum_{m=1}^{N_m} \mathbf{p}_m \Delta(\mathbf{y} - \mathbf{x}_m) d\Gamma \right)$ and quadrupole moment $\left(\int_{\Gamma} \frac{\partial}{\partial \mathbf{y}} \cdot \sum_{m=1}^{N_m} \left(\mathbf{q}_m \Delta(\mathbf{y} - \mathbf{x}_m) \right) f(\Gamma, t) d\Gamma \right)$ contributions to the total polarization density given by the first two terms on the right hand side of (2.16). A linear coarse-graining function corresponding to a coarse-graining length of 0.05 \AA is used. The left and right walls are located at -21.34595 \AA and 21.34595 \AA , respectively

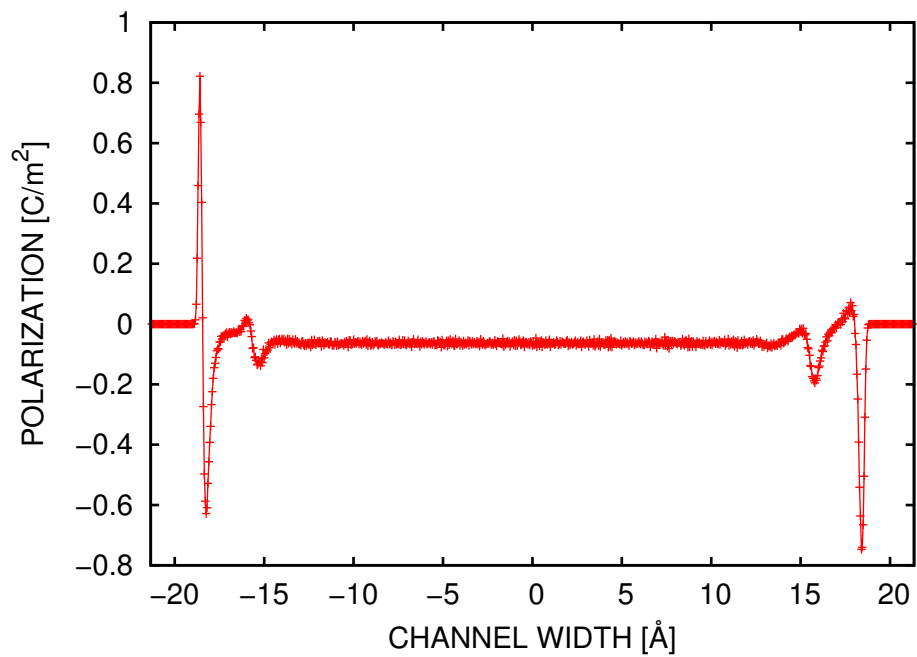


Figure 2.5. Bulk water: Resultant polarization vector containing contributions only from the dipole and quadrupole moments using a linear coarse-graining function (2.19) and a coarse-graining length of 0.05Å .

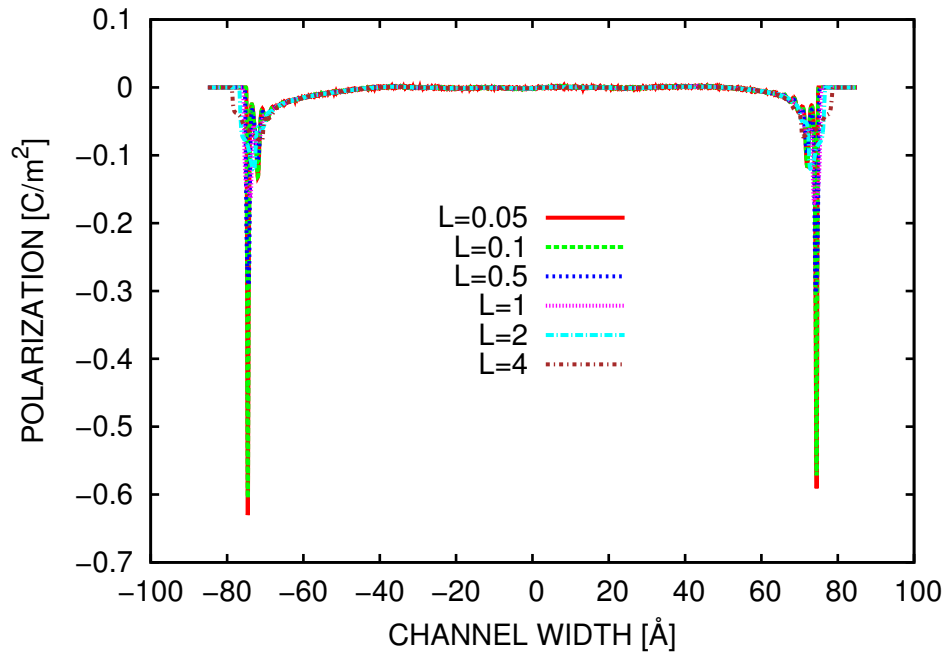


Figure 2.6. EDL: The wall-normal component of the polarization vector for several coarse-graining length scales using constant coarse-graining function (2.18).

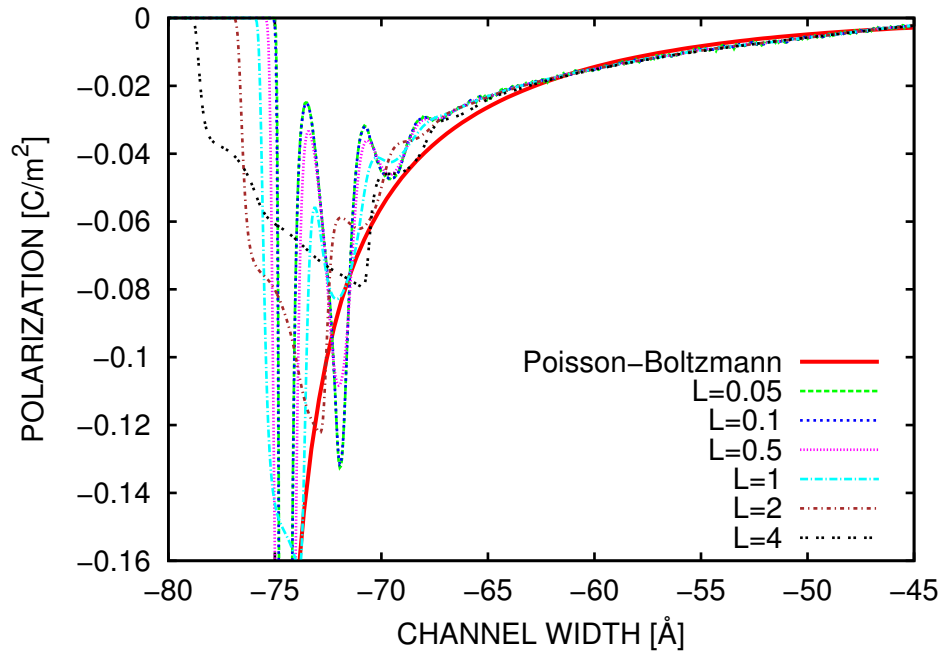


Figure 2.7. EDL: Close-up of the wall-normal component of the polarization vector near the negatively charged wall.

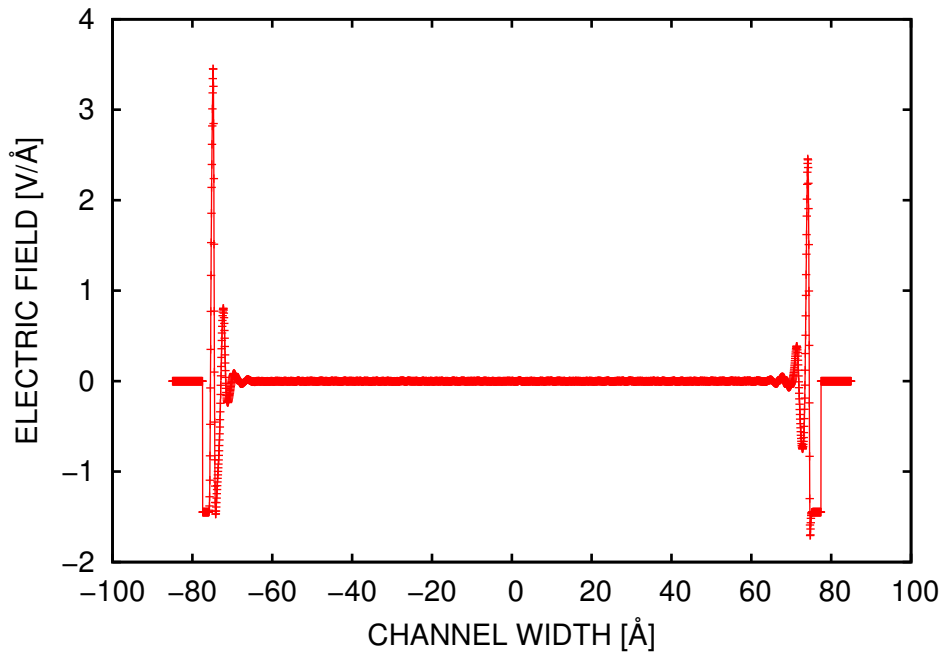


Figure 2.8. EDL: Spatially varying wall-normal component of the resultant (microscopic) electric field.

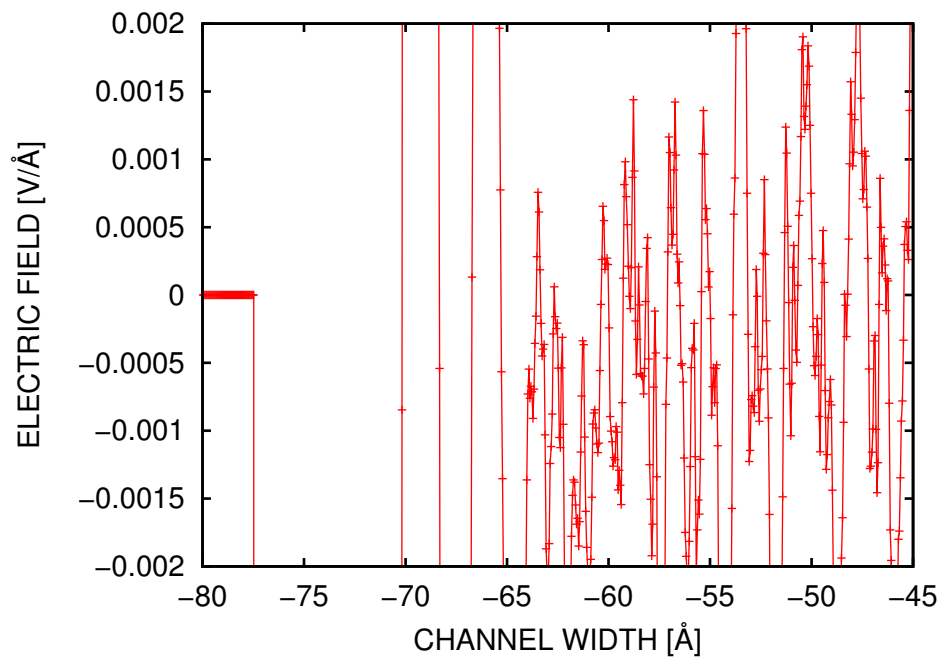


Figure 2.9. EDL: Close-up of the wall-normal component of the microscopic electric field near the negatively charged wall.

Chapter 3

A Fractional Step Method for Conserved Energy Exchange in Coupled Atomistic-Finite Element Simulations

3.1 Introduction

Increasing miniaturization of many engineering devices necessitates new simulation techniques capable of predictively modeling their behavior. As device scales reach the nanoscale, a multitude of phenomena, such as grain boundaries, defects, and surface effects, significantly impact performance. Nanotechnology is also leading to customized molecules and nanostructures which can be guided by simulation for specific designs. While continuum models have excelled at describing system behavior at the macroscale, they have thus far had difficulty capturing many of these effects peculiar to the nanoscale. At these small scales, continuum constitutive models such as Fourier's law for thermal diffusion can break down due to complex scattering processes and ballistic phonon propagation. Augmenting continuum models with atomistic processes suggest the use of multiscale coupling methods for atomic and continuous descriptions.

Atomistic-to-Continuum (AtC) modeling has emerged over the past two decades as a viable approach to providing enhanced fidelity to constitutive models, usually for finite elements (FE) and molecular dynamics (MD). The majority of this work has considered mechanical coupling in solids. For an overview and performance comparison of many of these methods, the interested reader is referred to the review by Miller & Tadmor [93] and the references therein. A focus in this area has been on defects, often to correctly capture their formation and propagation. However, there is a smaller body of literature regarding coupling atomistic and continuum descriptions of the temperature field. Finite temperature coupling schemes have been derived from several of these formulations: the quasi-continuum method [71], the bridging scale method [102], the bridging domain method [2], and domain decomposition methods for fluids [80].

The present work is based on the approach of Wagner *et al.* [129], which is most similar to the bridging scale method for mechanically coupling atoms and continua [130]. Its formulation generates two way interactions by 1) projecting the atomic degrees of freedom onto the FE basis, and 2) adding and removing energy from the atoms based on the FE heat flux at the FE/MD

The primary authors of this chapter are J. Templeton and R. Jones.

interface. Relevant to this work, the consistent heat flux between the FE and MD is enforced by expressing it as a constraint on the atomic dynamics, which leads to an enhanced MD force arising from Gauss' principle of least constraint. Additionally, the FE dynamics are separated into two terms based on the FE constitutive relation and the MD trajectories. An important distinction between that method and this work is that both terms were integrated in time using the Gear technique [35], while the atoms evolved using the velocity-Verlet algorithm [41]. These differences led to drift between the two systems of $O(\Delta t^2)$ because of the different temporal discretizations and how they evolved the intrinsic dynamics and the energy flux. It should be noted that numerical tests demonstrated that these errors were sufficiently small for many systems of interest.

Following on the previous study, Templeton *et al.* [123] used the same AtC formulation to apply standard FE boundary conditions to MD systems. Their main innovation was the derivation of a new constraint that enforced the MD temperature to equal the FE temperature; thus, Dirichlet and Neumann boundary conditions could both be used. However, Dirichlet conditions reduce the stability even further because drift between the FE and MD temperatures can lead to energy being incorrectly injected when it should be removed. In this work, it is desired to improve the stability of the algorithm such that Eulerian systems could be considered. Given the drift that can occur as atoms cross elements or due to errors in time integration involving shape function derivatives, a new algorithm is needed to improve the overall stability of the time integration. Additionally, it is desired to consider different temperature definitions than the kinetic definition. In many MD codes, it is not possible to directly evaluate the time derivative of these definitions, so the time integration algorithm must handle this difficulty as well.

The driving requirements for the time integration scheme, namely that it exactly satisfy the constraints associated with multiscale coupling and boundary conditions as well as provide exact integration of the projected MD motions suggest a specific time integration strategy: the fractional step method. Originally due to Chorin [18] to evolve the incompressible Navier-Stokes equations in time, fractional step integrators update hyperbolic or parabolic dynamics subject to elliptic constraints. While the equations of motion are subject to time integration error, the constraint is exactly satisfied for the particular realization. An added benefit is that these methods split different physics within differential equation so that each term can be updated using unique methods appropriate for its mathematical properties. As an example, in the Navier-Stokes equations the dynamic equations governing the momenta are constrained to conserve mass via the pressure, which satisfies a Poisson equation. The viscous and convective terms are also updated differently, for example using a Runge-Kutta scheme for convection and a semi-implicit update for the viscous stresses [65]. In this work, the analogies will be the algebraic constraint equation, which is mathematically has similarities to a Poisson equation, which enforces the energy constraint on the MD, and the use of different approaches to update the parts of the continuum right-hand side arising from the continuum constitutive relationship versus those informed by the MD. In the next section, the time-continuous equations will be derived, including the equation governing the coupling parameter. Section 3.3 will discretize these equations using a fractional step method. In section 4.5, some examples of the method will be presented followed by some closing remarks in section 4.6.

3.2 Derivation of the Temporally Continuous Equations

Consider the atomic energy density e_α , its continuous counterpart $e(\mathbf{x})$, and its finite element representation $e^h(\mathbf{x})$ defined as a linear combination of a finite set of shape functions, N_I :

$$e^h(\mathbf{x}) = \sum_I N_I(\mathbf{x}) e_I. \quad (3.1)$$

The FE and continuous representations are related by minimizing the L^2 error between them, i.e.

$$\int_{\Omega} \left(e(\mathbf{x}) - e^h(\mathbf{x}) \right)^2 dV. \quad (3.2)$$

Taking the variation of with respect to e^h and setting it equal to zero gives

$$\int_{\Omega} \delta e^h(\mathbf{x}) e^h(\mathbf{x}) dV = \int_{\Omega} \delta e^h(\mathbf{x}) e(\mathbf{x}) dV. \quad (3.3)$$

where e is known data and e^h is the unknown. These integrals can be split into integrals over the MD and FE domains:

$$\int_{\Omega_{fem}} \delta e^h(\mathbf{x}) e^h(\mathbf{x}) dV + \sum_{\alpha} \delta e^h(\mathbf{x}_{\alpha}) e^h(\mathbf{x}_{\alpha}) \Delta V_{\alpha} = \int_{\Omega_{fem}} \delta e^h(\mathbf{x}) e(\mathbf{x}) dV + \sum_{\alpha} \delta e^h(\mathbf{x}_{\alpha}) e_{\alpha} \Delta V_{\alpha}, \quad (3.4)$$

where ΔV_{α} is the quadrature volume associated with each atom. Thus the equations for the nodal variables are

$$\sum_J \left(\int_{\Omega_{fem}} N_I N_J e_J dV + \sum_{\alpha} N_{I\alpha} N_{J\alpha} e_J \Delta V_{\alpha} \right) = \int_{\Omega_{fem}} N_I e(\mathbf{x}) dV + \sum_{\alpha} N_{I\alpha} e_{\alpha} \Delta V_{\alpha}, \quad (3.5)$$

with the spatial dependence absorbed into the shape function notation for convenience.

The primary consideration of this work is thermal transport problems where the primary dependent variable is temperature. The equations will be derived for the energy density without kinetic components so energy density is assumed to have the functional form $e = \rho c T$ such that ρ is the mass density, c the specific heat capacity, and T is the temperature. Inserting this expression into projection (3.5) results in the following equation:

$$\sum_J \left(\int_{\Omega_{fem}} N_I N_J [\rho c T]_J dV + \sum_{\alpha} N_{I\alpha} N_{J\alpha} [\rho c T]_J \Delta V_{\alpha} \right) = \int_{\Omega_{fem}} N_I [\rho c T] dV + \sum_{\alpha} N_{I\alpha} e_{\alpha} \Delta V_{\alpha}. \quad (3.6)$$

To put the equations in a form more amenable to finite element (FE) analysis, we use the approximation that $E_I = [\rho c T]_I \approx \rho c T_I$ in the continuous integral and $[\rho c T]_I = \rho_{\alpha} c_{\alpha} T_I$ in the atomic sum to reflect the fact that the density and heat capacity will be given by equations of state appropriate

to either the continuous or atomic description. Next, the atomic quadrature volume is used in the expressions for both the mass density and energy density so that

$$\begin{aligned}\rho_\alpha &= \frac{m_\alpha}{\Delta V_\alpha} \\ e_\alpha &= \frac{E_\alpha}{\Delta V_\alpha},\end{aligned}$$

where E_α is the total energy of the atom (see the next subsection for further discussion) given by

$$E_\alpha = K_\alpha + P_\alpha = \frac{1}{2}m_\alpha \mathbf{v}_\alpha^2 + \phi_\alpha, \quad (3.7)$$

with K_α and P_α being the atomic kinetic and potential energies, respectively. Dividing the total potential energy amongst all atoms is not straightforward for complex interatomic potentials, but reasonable values can be chosen for most of them; a simple equipartition of the energy of a bond between the atoms that make constitute it is always available. The definition of E_α assumes that all the atomic energy is fluctuating so it can be represented by a temperature. Note that defining a temperature locally and instantaneously is not fully justified theoretically. This work, however, focuses on non-equilibrium calculations under the assumption for certain length and timescales, a temperature can be defined. It is these scales that define the FE mesh and the time filter window discussed later in this work.

As a rough approximation, the correlation distances and times of energy fluctuations provide a lower bound for the coarse-graining length and timescales. With these assumptions, the projection becomes

$$\sum_J \left(\int_{\Omega_{fem}} N_I N_J \rho c T_J dV + \sum_\alpha N_{I\alpha} N_{J\alpha} m_\alpha c_\alpha T_J \right) = \int_{\Omega_{fem}} N_I [\rho c T] dV + \sum_\alpha N_{I\alpha} E_\alpha. \quad (3.8)$$

A feature of these definitions is that the atomic volume is never required.

In writing the equations in this form, it is necessary to have an expression for the atomic heat capacity. If the temperature is above the Debye temperature, the Dulong-Petit expression for the specific heat capacity is reasonable: $c_\alpha = 3k_B/m_\alpha$. The result of these assumptions is to arrive at the following projection

$$\sum_J \left(\int_{\Omega_{fem}} N_I N_J \rho c dV + \sum_\alpha N_{I\alpha} N_{J\alpha} 3k_B \right) T_J = \int_{\Omega_{fem}} N_I [\rho c T] dV + \sum_\alpha N_{I\alpha} E_\alpha. \quad (3.9)$$

Finally, the dynamical equation for thermal transport is obtained by taking the time derivative:

$$\begin{aligned}\sum_J \left(\int_{\Omega_{fem}} N_I N_J \rho c dV + \sum_\alpha N_{I\alpha} N_{J\alpha} 3k_B \right) \frac{dT_J}{dt} = \\ - \int_{\Omega_{fem}} \nabla N_I \cdot \mathbf{q}^h dV + \int_{\partial\Omega_{fem}} N_I \mathbf{q}^h \cdot \mathbf{n}_{MD} dS + \sum_\alpha N_{I\alpha} \dot{E}_\alpha.\end{aligned} \quad (3.10)$$

The heat flux term, \mathbf{q} , has been integrated by parts which results in the additional boundary integral over the normal heat flux dotted with the inward normal vector \mathbf{n}_{MD} to the MD region (traditional boundary fluxes to the FE domain are ignored for clarity in this presentation, but trivial to incorporate into the method).

Finally, in order to obtain comparable timescales between the atomistic and continuum dynamics it is often necessary to filter the atomistic quantities in time as part of the interscale restriction operation. The filtering operation for T is defined by:

$$\langle T(t) \rangle = \int_{-\infty}^t \tau^{-1} T(t') e^{-(t-t')/\tau} dt', \quad (3.11)$$

where τ is the timescale of the filter (see [129] for a discussion of the benefits of this functional form). To derive the filtered equations, the filtering operator is applied to eq. (3.10):

$$\begin{aligned} \left\langle \sum_J \left(\int_{\Omega_{fem}} N_I N_J \rho c dV + \sum_{\alpha} N_{I\alpha} N_{J\alpha} 3k_B \right) \frac{dT_J}{dt} \right\rangle = \\ - \left\langle \int_{\Omega_{fem}} \nabla N_I \cdot \mathbf{q} dV \right\rangle + \left\langle \int_{\partial\Omega_{fem}} N_I \mathbf{q}^h \cdot \mathbf{n}_{MD} dS \right\rangle + \left\langle \sum_{\alpha} N_{I\alpha} \dot{E}_{\alpha} \right\rangle. \end{aligned} \quad (3.12)$$

Making the previous equation tractable requires assuming equivalence between filtered and unfiltered continuous terms, resulting in the governing equation for filtered variables:

$$\begin{aligned} \sum_J \left(\int_{\Omega_{fem}} N_I N_J \rho c dV + \left\langle \sum_{\alpha} N_{I\alpha} N_{J\alpha} 3k_B \right\rangle \right) \frac{dT_J}{dt} = \\ - \int_{\Omega_{fem}} \nabla N_I \cdot \mathbf{q} dV + \int_{\partial\Omega_{fem}} N_I \mathbf{q}^h \cdot \mathbf{n}_{MD} dS + \left\langle \sum_{\alpha} N_{I\alpha} \dot{E}_{\alpha} \right\rangle. \end{aligned} \quad (3.13)$$

To simplify the presentation in the next section, equations will be presented without time filtering but can be filtered in the same manner as eq. (3.13). The implications of time filtering on the numerical methods will be considered in Section 3.3.1.

3.2.1 Coupling with Thermostats

The previous section derived the set of ODEs governing the FE degrees of freedom that account for the molecular motions. In order to achieve two-way interactions, a set of constraints will be posed on the MD based on FE information. A notable distinction between this work and previous efforts ([129, 123]) is that the constraints are posed on conserved quantities rather than observed quantities, e.g., energy rather than temperature, which generalizes the systems it can be applied to. Specifically, the different formulation facilitates applying the method to fluid problems because the mass matrix appears on the right-hand side rather than embedded in the left-hand side matrix.

The first coupling mode considered is that for fixing the MD energy to match that of the FE. The constraint for the I th node can be written as

$$\sum_{\alpha} N_{I\alpha} \dot{E}_{\alpha} - \sum_J M_{IJ}^{MD} \dot{T}_J = 0, \quad (3.14)$$

where the following shorthand has been used:

$$M_{IJ}^{MD} = \sum_{\alpha} N_{I\alpha} N_{J\alpha} 3k_B.$$

In order to make further progress, it is necessary to substitute in eq. (3.7):

$$\sum_{\alpha} N_{I\alpha} (\mathbf{v}_{\alpha} \cdot \mathbf{f}_{\alpha} + \dot{\phi}_{\alpha}) - \sum_J M_{IJ}^{MD} \dot{T}_J = 0. \quad (3.15)$$

This is a constraint in \mathbf{f}_{α} that can be solved by applying Gauss' principle of least constraint [31] to the velocity to obtain (specifically $m_{\alpha}^{-1} (\mathbf{f}_{\alpha} - \mathbf{f}_{\alpha}^{MD})^2$ is minimized):

$$\mathbf{f}_{\alpha} = \mathbf{f}_{\alpha}^{MD} - \frac{m_{\alpha}}{2} \mathbf{v}_{\alpha} \sum_I N_{I\alpha} \lambda_I, \quad (3.16)$$

$$\sum_{\alpha} \sum_J N_{I\alpha} K_{\alpha} N_{J\alpha} \lambda_J = \sum_{\alpha} N_{I\alpha} (\mathbf{v}_{\alpha} \cdot \mathbf{f}_{\alpha}^{MD} + \dot{\phi}_{\alpha}) - \sum_J M_{IJ}^{MD} \dot{T}_J. \quad (3.17)$$

where \dot{T}_I is held constant. In eq. (3.17), the power added through $\mathbf{f}_{\alpha}^{\lambda}$ augments the local heat flux such that the MD temperature time derivative matches a prescribed value locally ("local" in this case is with respect to integration against FE shape functions). An advantage of the present framework can regulate the temperature for any definition of it that includes kinetic energy because the constraint minimizes the change in acceleration by the application of the thermostat.

Similarly, consider also the flux-based thermostat based on the constraint

$$\sum_{\alpha} N_{I\alpha} \left(\frac{\partial \Phi}{\partial \mathbf{x}_{\alpha}} \cdot \mathbf{v}_{\alpha} + \mathbf{v}_{\alpha} \cdot \mathbf{f}_{\alpha} \right) + \int_{\Gamma_{fem}} N_I \mathbf{q}^h \cdot \mathbf{n}_{MD} dS = 0, \quad (3.18)$$

which expresses the requirement that the total rate of change of energy in both systems must be equal and opposite. An important point is that the total potential energy is $\Phi \neq \sum_{\alpha} \phi_{\alpha}$ due to contributions from any ghost atoms (fixed atoms used to give the free atoms a full complement of neighbors) that are present. These atoms serve to apply an external potential that perfectly reflects phonons leaving the set of real atoms. In this capacity, these atoms do not add or subtract energy from the real atoms, i.e., they do no work because they are fixed. However, this form does enable using $\partial \Phi / \partial \mathbf{x}_{\alpha} \cdot \mathbf{v}_{\alpha} = -\mathbf{v}_{\alpha} \cdot \mathbf{f}_{\alpha}^{MD}$ to simplify the problem to one amenable to the application of Gauss' principle of least constraint to \mathbf{f}_{α} . It results in the following set of equations for λ_I :

$$\mathbf{f}_{\alpha} = \mathbf{f}_{\alpha}^{MD} - \frac{m_{\alpha}}{2} \mathbf{v}_{\alpha} \sum_I N_{I\alpha} \lambda_I, \quad (3.19)$$

$$\sum_{\alpha} \sum_J N_{I\alpha} K_{\alpha} N_{J\alpha} \lambda_J = \int_{\Gamma_{fem}} N_I \mathbf{q}^h \cdot \mathbf{n}_{MD} dS. \quad (3.20)$$

The unknown boundary heat flux \mathbf{q}^h can be computed by FE face quadrature or approximate L^2 projection citewagner08. However, in contrast to that previous work, this form will exactly cancel the MD/FE boundary energy flux from the FE equations because the kinetic definition of temperature is used. Since the same matrix equation arises for both types of constraints (the RHS is simply shifted based on the type), the cancelation will happen for both temperature and flux coupling.

This cancelation, combined with the change in the definition of the temperature, will improve the fidelity of the atomic temperature near the boundary.

Understanding how the cancellation of the boundary flux term in the FE equations occurs can be done by considering an arbitrary fluctuating energy definition,

$$E_\alpha = aK_\alpha + bP_\alpha, \text{ s.t. } a + b = 2,$$

The governing equation for λ , eq. (3.17) becomes

$$\sum_\alpha \sum_J N_{I\alpha} K_\alpha N_{J\alpha} \lambda_J = a^{-1} \left(\sum_\alpha N_{I\alpha} (a\mathbf{v}_\alpha \cdot \mathbf{f}_\alpha^{MD} + b\dot{\phi}_\alpha) - M_{MD} \dot{T}_I \right). \quad (3.21)$$

This change also has an effect on the overall governing FE equation, eq. (3.10). The term representing the MD contributions to the finite element equations can be expressed as:

$$\begin{aligned} \sum_\alpha N_{I\alpha} \dot{E}_\alpha &= \sum_\alpha N_{I\alpha} \left(a\mathbf{v}_\alpha \cdot \mathbf{f}_\alpha^{MD} + b\dot{\phi}_\alpha + a\mathbf{v}_\alpha \cdot \mathbf{f}_\alpha^\lambda \right) \\ &= \sum_\alpha N_{I\alpha} (a\mathbf{v}_\alpha \cdot \mathbf{f}_\alpha^{MD} + b\dot{\phi}_\alpha) - a \sum_\alpha N_{I\alpha} K_\alpha \sum_J N_{J\alpha} \lambda_J \\ &= \sum_\alpha N_{I\alpha} (a\mathbf{v}_\alpha \cdot \mathbf{f}_\alpha^{MD} + b\dot{\phi}_\alpha) - aRHS_I, \end{aligned}$$

where the *RHS* expression is used to denote the right-hand side of either constraint, i.e. eq. (3.20) or eq. (3.21). Hence, eq. (3.10) becomes

$$\begin{aligned} \sum_J \left(\int_{\Omega_{fem}} N_I N_J \rho c dV + \sum_\alpha N_{I\alpha} N_{J\alpha} 3k_B \right) \frac{dT_J}{dt} = \\ - \int_{\Omega_{fem}} \nabla N_I \cdot \mathbf{q} dV + \sum_\alpha N_{I\alpha} (a\mathbf{v}_\alpha \cdot \mathbf{f}_\alpha^{MD} + b\dot{\phi}_\alpha) \\ + \int_{\partial\Omega_{fem}} N_I \mathbf{q}^h \cdot \mathbf{n}_{MD} dS - aRHS_I. \quad (3.22) \end{aligned}$$

In the case of temperature coupling, the FE boundary flux is set to balance the energy added to the MD,

$$\int_{\partial\Omega_{fem}} N_I \mathbf{q}^h \cdot \mathbf{n}_{MD} dS = \left(\sum_\alpha N_{I\alpha} (a\mathbf{v}_\alpha \cdot \mathbf{f}_\alpha^{MD} + b\dot{\phi}_\alpha) - M_{MD} \dot{T}_I \right). \quad (3.23)$$

For flux-based coupling, the boundary flux must be computed to have a closed set of equations to solve. Denoting the nodes at which the flux constraint is enforced as $I_f \subset I$, the total evolution equation is

$$\begin{aligned} \sum_J \left(\int_{\Omega_{fem}} N_I N_J \rho c dV + \sum_\alpha N_{I\alpha} N_{J\alpha} 3k_B \right) \frac{dT_J}{dt} = \\ - \int_{\Omega_{fem}} \nabla N_I \cdot \mathbf{q} dV + \sum_\alpha N_{I\alpha} (a\mathbf{v}_\alpha \cdot \mathbf{f}_\alpha^{MD} + b\dot{\phi}_\alpha) \\ + (1-a) 1_{I \in I_f} \int_{\partial\Omega_{fem}} N_I \mathbf{q}^h \cdot \mathbf{n}_{MD} dS. \quad (3.24) \end{aligned}$$

For the case $a = 1$, the boundary flux terms will not appear in the FE governing equation

To complete all the needed functionality for this work with the new formulation, the rescaling thermostat must also be changed from its form in [129]. For each atom, its atomic velocity is rescaled using a local rescale parameter:

$$\mathbf{v}_\alpha = \sqrt{\psi_\alpha} \mathbf{v}_\alpha^{MD}. \quad (3.25)$$

To enforce a temperature field which varies on the FE scale, the rescale parameter will be represented using the FE basis,

$$\psi_\alpha = \sum_I N_{I\alpha} \psi_I. \quad (3.26)$$

The reciprocal of the atomic mass and weighted shape functions are used in eqs. (3.25) and (3.26) in order to have the result utilize the same thermostat matrix as the constraint-based thermostats. The constraint associated with the rescale is

$$\sum_\alpha N_{I\alpha} (aK_\alpha + bP_\alpha) = M_{MD} T_I. \quad (3.27)$$

By substituting eq. (3.25) into eq. (3.27), the equation for ψ_I is obtained

$$\sum_\alpha \sum_J N_{I\alpha} K_\alpha N_{J\alpha} \psi_I = a^{-1} \left(M_{MD} T_I - b \sum_\alpha N_{I\alpha} P_\alpha \right). \quad (3.28)$$

3.3 Fractional Step Time Advancement

3.3.1 Time Integration Scheme

Combining the temporal ODEs for the MD and FE degrees of freedom with the spatial differential equation for the coupling parameter λ form a closed set of equations governing the evolution of the entire system. However, developing a time integration scheme for this system poses several challenges. First, not all of the terms in it have a time derivative that can be directly evaluated, e.g., $\dot{\phi}_\alpha$. In addition, when the atomic shape functions $N_{I\alpha}$ are allowed to change with time (as for a fluid), then integrating their time derivative,

$$\dot{N}_{I\alpha} = \nabla N_{I\alpha} \cdot \mathbf{v}_\alpha, \quad (3.29)$$

will pose problems. If linear shape functions are used, then mass will not be conserved when atoms cross element boundaries. On the other hand, when using higher-order shape functions, integrating the above equation over a finite time step will lead to errors in the mass because $\Delta N_{I\alpha} \neq \Delta t \dot{N}_{I\alpha}$. A similar problem occurs if the time derivatives for the kinetic energy are directly used because the temperature is a non-linear function of velocity. For example, consider the velocity updated from step n to $n+1$ using explicit Euler:

$$\mathbf{v}_\alpha|_{n+1} = \mathbf{v}_\alpha|_n + \Delta t m_\alpha^{-1} \mathbf{f}_\alpha|_n. \quad (3.30)$$

The corresponding change in kinetic energy is

$$\begin{aligned}
K_\alpha|_{n+1} &= \frac{m_\alpha}{2} \mathbf{v}_\alpha^2|_{n+1} \\
&= \frac{m_\alpha}{2} (\mathbf{v}_\alpha|_n + \Delta t m_\alpha^{-1} \mathbf{f}_\alpha|_n)^2 \\
&= K_\alpha|_n + \Delta t \mathbf{v}_\alpha|_n \cdot \mathbf{f}_\alpha|_n + \Delta t^2 \frac{m_\alpha^{-1}}{2} \mathbf{f}_\alpha|_n \cdot \mathbf{f}_\alpha|_n \\
&= K_\alpha|_n + \Delta t \dot{K}_\alpha|_n + O(\Delta t^2)
\end{aligned}$$

Hence, application of the same time integration methods to both the MD and FE equations will result in a drift between them which is aggravated because the error is strictly positive. Particularly when using a fixed temperature constraint on the MD, temperature drift can lead to eventual instabilities as the coupling scheme will start incorrectly adding or removing energy. This analysis shows that the two difficulties in developing temporal integration techniques for these equations are the need to satisfy a constraint to numerical precision and the need to use different methods for different terms in the FE evolution. Such issues suggest development of a fractional step method [18] to enable their resolution.

Time integration of the continuous temperature consists of two parts. The first part comes from modifying the standard velocity Verlet integration scheme to incorporate the forces from the thermostat to integrate the position at time level n to time level $n+1$ and to predict the velocity at time level $n+1$ based on the velocity at time level n :

$$\hat{\mathbf{v}}_\alpha|_{n+1/2} = \mathbf{v}_\alpha|_n + \frac{\Delta t}{2} m_\alpha^{-1} \mathbf{f}_\alpha^\lambda|_n \quad (3.31)$$

$$\mathbf{v}_\alpha|_{n+1/2} = \hat{\mathbf{v}}_\alpha|_{n+1/2} + \frac{\Delta t}{2} m_\alpha^{-1} \mathbf{f}_\alpha^{MD}|_n \quad (3.32)$$

$$\mathbf{x}_\alpha|_{n+1} = \mathbf{x}_\alpha|_n + \Delta t \mathbf{v}_\alpha|_{n+1/2} \quad (3.33)$$

$$\hat{\mathbf{v}}_\alpha|_{n+1} = \mathbf{v}_\alpha|_{n+1/2} + \frac{\Delta t}{2} m_\alpha^{-1} \mathbf{f}_\alpha^{MD}|_{n+1} \quad (3.34)$$

$$\tilde{\mathbf{v}}_\alpha|_{n+1} = \hat{\mathbf{v}}_\alpha|_{n+1} + \frac{\Delta t}{2} m_\alpha^{-1} \mathbf{f}_\alpha^\lambda|_n \quad (3.35)$$

The notation used in the preceding equations is as follows. A \hat{q} indicates the first prediction of a quantity while the \tilde{q} denotes the second prediction. It is used in this case to represent the prediction of atomic velocity at time level $n+1$ based on the older coupling force to maintain the second order accuracy of the overall method. MD forces are determined by the atomic positions at time level $n, n+1$, etc., and are calculated independently of the present method. The coupling force is determined by the constraints, and is described in more detail in the next section.

In order to connect the atomic updates to the continuous system, first consider the change in energy of atom α through this process. For example, the change in kinetic energy induced by eq. (3.31) is

$$\begin{aligned}
\Delta \hat{K}_\alpha|_{n+1/2} &= \frac{m_\alpha}{2} \left(\hat{\mathbf{v}}_\alpha|_{n+1/2} \cdot \hat{\mathbf{v}}_\alpha|_{n+1/2} - \mathbf{v}_\alpha|_n \cdot \mathbf{v}_\alpha|_n \right) \\
&= \frac{\Delta t}{2} \mathbf{v}_\alpha|_n \cdot \mathbf{f}_\alpha^\lambda|_n + \frac{\Delta t^2}{8} m_\alpha^{-1} \mathbf{f}_\alpha^\lambda|_n \cdot \mathbf{f}_\alpha^\lambda|_n,
\end{aligned} \quad (3.36)$$

while the change in potential energy is simply due to the evaluation of the interatomic potential at time level $n + 1$:

$$\Delta P_\alpha|_{n+1} = \phi_\alpha|_{n+1} - \phi_\alpha|_n. \quad (3.37)$$

The total change in atomic energy is then

$$\Delta \tilde{E}_\alpha|_{n+1} = \Delta \hat{K}_\alpha|_{n+1/2} + \Delta K_\alpha|_{n+1/2} + \Delta P_\alpha|_{n+1} + \Delta \hat{K}_\alpha|_{n+1} + \Delta \tilde{K}_\alpha|_{n+1}. \quad (3.38)$$

The next step in developing the appropriate time integration algorithm is to relate eq. (3.38) to the exact PDE eq. (3.10). Throughout the remainder of this work, changes in atomic quantities will be considered as differences between quantities at different time levels rather than time derivatives. This point of view offers two advantages: the ability to account for any atomic quantity, e.g. ϕ_α , which may not have an evaluatable time derivative, and the definition of the numerically exact energy exchange between the FE and MD systems. Direct application of this definition yields a change in the FE temperature field of

$$\Delta \left(\sum_J M_{IJ} \tilde{T}_{J,\mathcal{A}} \right) \Big|_{n+1} = \Delta \left\langle \sum_\alpha N_{I\alpha} \tilde{E}_\alpha \right\rangle \Big|_{n+1}, \quad (3.39)$$

where the subscript \mathcal{A} denotes this is the temperature associated with the set of atoms. In addition, the terms multiplying T_J on the left-hand side of eq. (3.10) have been expressed succinctly as the mass matrix M_{IJ} . The expression in eq. (3.39) has dispensed with the assumptions of constant mass matrices consistent with atomic shape functions based on reference positions, making it appropriate for Eulerian frame calculations. To also account for the time filtering aspect of the interscale operations, consider the following relationship between the nodal temperature and the atomic energy as

$$\sum_J M_{IJ} T_{J,\mathcal{A}} = \left\langle \sum_\alpha N_{I\alpha} E_\alpha \right\rangle = \langle E_I \rangle, \quad (3.40)$$

which reduces atomic fluctuations to make the MD-FE coupling more appropriate for the FE constitutive laws. We now briefly present the important features of the filtering operation as it pertains to the time integration scheme.

The time filtering kernel takes the same form as in [129], i.e.,

$$\langle E_I(t) \rangle \equiv \int_{-\infty}^t \tau^{-1} E_I(t') e^{-(t-t')/\tau} dt'. \quad (3.41)$$

This form is advantageous because its time derivative can be written analytically as

$$\frac{d}{dt} \langle E_I \rangle = \frac{E_I - \langle E_I \rangle}{\tau} \quad (3.42)$$

which forms the basis of the discrete filter used in this work. Following the velocity Verlet algorithm, a two-stage explicit/implicit discretization is used:

$$\langle E_I \rangle|_{n+1/2} = \langle E_I \rangle|_n + \frac{\Delta t}{2\tau} (\langle E_I \rangle|_n - \langle E_I \rangle|_n) \quad (3.43)$$

$$\langle E_I \rangle|_{n+1} = \frac{1}{1 + \frac{\Delta t}{2\tau}} \left(\langle E_I \rangle|_{n+1/2} + \frac{\Delta t}{2\tau} E_I|_{n+1} \right). \quad (3.44)$$

The salient part of this update is that there exists constants ζ , β , γ such that

$$\langle E_I \rangle|_{n+1} = \zeta E_I|_n + \gamma E_I|_{n+1} + \beta \langle E_I \rangle|_n. \quad (3.45)$$

Then the change in the filtered quantity over a time step is

$$\Delta \langle E_I \rangle|_{n+1} = (\beta - 1) \langle E_I \rangle|_n + (\zeta + \gamma) E_I|_n + \gamma \Delta E_I|_{n+1}. \quad (3.46)$$

To separate out the change in temperature needed in the time integration process, consider

$$\begin{aligned} \Delta \tilde{T}_{I,\mathcal{A}}|_{n+1} &= \tilde{T}_{I,\mathcal{A}}|_{n+1} - \tilde{T}_{I,\mathcal{A}}|_n \\ &= \sum_J M_{IJ}^{-1}|_{n+1} \left\langle \sum_{\alpha} N_{I\alpha} \tilde{E}_{\alpha} \right\rangle|_{n+1} - \sum_J M_{IJ}^{-1}|_n \left\langle \sum_{\alpha} N_{I\alpha} \tilde{E}_{\alpha} \right\rangle|_n \\ &= \sum_J M_{IJ}^{-1}|_{n+1} \left(\left\langle \sum_{\alpha} N_{I\alpha} \tilde{E}_{\alpha} \right\rangle|_n + \Delta \left\langle \sum_{\alpha} N_{I\alpha} \tilde{E}_{\alpha} \right\rangle|_{n+1} \right) - \sum_J M_{IJ}^{-1}|_n \left\langle \sum_{\alpha} N_{I\alpha} \tilde{E}_{\alpha} \right\rangle|_n \\ &= \sum_J M_{IJ}^{-1}|_{n+1} \Delta \left\langle \sum_{\alpha} N_{I\alpha} \tilde{E}_{\alpha} \right\rangle|_{n+1} + \left(\sum_J M_{IJ}^{-1}|_{n+1} - \sum_J M_{IJ}^{-1}|_n \right) \left\langle \sum_{\alpha} N_{I\alpha} \tilde{E}_{\alpha} \right\rangle|_n \end{aligned}$$

Using eq. (3.46) with eq. (3.39) gives an expression for the change in restricted energy due to the atomic system:

$$\begin{aligned} \Delta \left\langle \sum_{\alpha} N_{I\alpha} \tilde{E}_{\alpha} \right\rangle|_{n+1} &= \\ &= (\beta - 1) \left\langle \sum_{\alpha} N_{I\alpha} \tilde{E}_{\alpha} \right\rangle|_n + (\zeta + \gamma) \left(\sum_{\alpha} N_{I\alpha} E_{\alpha} \right)|_n + \gamma \left(\sum_{\alpha} N_{I\alpha} \Delta \tilde{E}_{\alpha} \right)|_{n+1}. \end{aligned} \quad (3.47)$$

The second part of the time integration process accounts for the continuous scale contributions, which come through either in coupled simulation or through integrating boundary conditions and prescribed nodes. These are handled through a 3rd or 4th order Gear integration scheme, following [129] depending on whether or not time filtering is used. The 4th order scheme produces a predicted change in the temperature due to the set \mathcal{S} of FE nodes:

$$\Delta \tilde{T}_{I,\mathcal{S}}|_{n+1} = \Delta t \dot{T}_{I,\mathcal{S}}|_n + \left(\frac{\Delta t}{2} \right)^2 \ddot{T}_{I,\mathcal{S}}|_n + \left(\frac{\Delta t}{6} \right)^3 \dddot{T}_{I,\mathcal{S}}|_n \quad (3.48)$$

$$\Delta \tilde{\dot{T}}_{I,\mathcal{S}}|_{n+1} = \Delta t \ddot{T}_{I,\mathcal{S}}|_n + \left(\frac{\Delta t}{2} \right)^2 \dddot{T}_{I,\mathcal{S}}|_n \quad (3.49)$$

$$\Delta \tilde{\ddot{T}}_{I,\mathcal{S}}|_{n+1} = \Delta t \dddot{T}_{I,\mathcal{S}}|_n. \quad (3.50)$$

Finally, it is possible to arrive at a predicted nodal temperature field,

$$\tilde{T}_I|_{n+1} = T_I|_n + \Delta \tilde{T}_{I,\mathcal{A}}|_{n+1} + \Delta \tilde{T}_{I,\mathcal{S}}|_{n+1}, \quad (3.51)$$

with the FE temperature time derivatives updated in a similar manner.

The predicted temperature field is required for two reasons. First, as part of the Gear update, it enables the time derivative at level $n + 1$, $\dot{T}_{I,\mathcal{A}}|_{n+1}$, to be computed. From it, the correction to the temperature is applied using the Gear corrector step:

$$R|_{n+1} = \Delta t \left(\dot{T}_{I,\mathcal{A}}|_{n+1} - \tilde{\dot{T}}_{I,\mathcal{A}}|_{n+1} \right), \quad (3.52)$$

$$\Delta T_{I,\mathcal{A}}|_{n+1} = \Delta \tilde{T}_{I,\mathcal{A}}|_{n+1} + \frac{3}{8} R|_{n+1} \quad (3.53)$$

$$\Delta \ddot{T}_{I,\mathcal{A}}|_{n+1} = \Delta \tilde{\ddot{T}}_{I,\mathcal{A}}|_{n+1} + \frac{3}{2} \Delta t^{-2} R|_{n+1} \quad (3.54)$$

$$\Delta \ddot{\ddot{T}}_{I,\mathcal{A}}|_{n+1} = \Delta \tilde{\ddot{\ddot{T}}}_{I,\mathcal{A}}|_{n+1} + \Delta t^{-3} R|_{n+1}, \quad (3.55)$$

$$\hat{T}_I|_{n+1} = \tilde{T}_I + \Delta T_{I,\mathcal{A}}|_{n+1}. \quad (3.56)$$

With the correction to the FE temperature in place, the updated control variable λ^{n+1} and its associated force can be determined. The specific discrete form for this equation is presented in the next section, but for the purposes of time integration the germain points are that it depends either on $\hat{T}_I|_{n+1}$ or $\Delta \hat{T}_I|_{n+1}$. The only manner in which the control force can alter these quantities (as will be shown) is by changing the temperature at interior nodes adjacent to boundary nodes (the boundary flux cancels with the restricted control power at boundary nodes). However, by predicting the temperature, the correction is second order in time.

Once computed, the updated control variable $\lambda_I|_{n+1}$ is used to create the control force which updates the atomic state variables as follows:

$$\mathbf{v}_\alpha|_{n+1} = \tilde{\mathbf{v}}_\alpha|_{n+1} + \frac{\Delta t}{2} m_\alpha^{-1} \mathbf{f}_\alpha^\lambda|_{n+1} \quad (3.57)$$

$$\Delta KE_\alpha^\lambda|_{n+1} = \frac{\Delta t}{2} \tilde{\mathbf{v}}_\alpha|_{n+1} \cdot \mathbf{f}_\alpha|_{n+1} + \frac{\Delta t^2}{2} \mathbf{f}_\alpha^\lambda|_{n+1} \cdot \mathbf{f}_\alpha^\lambda|_{n+1} \quad (3.58)$$

$$E_\alpha|_{n+1} = \tilde{E}_\alpha|_{n+1} + \Delta KE_\alpha^\lambda|_{n+1}. \quad (3.59)$$

The continuous temperature field at time level $n + 1$ can then be fully determined by

$$M_{IJ}|_{n+1} \Delta T_{J,\mathcal{A}}|_{n+1} = \sum N_{I\alpha}|_{n+1} \Delta KE_\alpha^\lambda|_{n+1} \quad (3.60)$$

$$T_I|_{n+1} = \hat{T}_I|_{n+1} + \Delta T_{I,\mathcal{A}}|_{n+1}. \quad (3.61)$$

Note that eqns. (3.48)-(3.61) could be solved iteratively in conjunction with the thermostat to improve the estimate of the FE temperature, although no advantage to such an approach has been observed.

While the above algorithm is more complex than previous work through the use of multiple prediction steps and a direct form for the atomic contribution to the FE field, the additional complexity is justified by its advantages. It is more stable because there is only very limited drift between the FE and MD temperatures in overlapping regions. The effect is reduced error in the right-hand side of eq. (3.17). In addition, energy is conserved to machine precision in the exchange

between the FE and MD systems. The other benefit derived by this time integration scheme is that it is appropriate for temperature definitions which cannot access an explicit time derivative, e.g., if the time derivative analogous to eq. (3.37) cannot be evaluated from the MD code.

There is one final advantage to this algorithm: it is appropriate for Eulerian frame calculations in which $N_{I\alpha}$ is a function of time rather than held constant in the referential frame. This is because direct calculation of the time derivative:

$$\dot{N}_{I\alpha} = (\nabla N_{I\alpha}) \cdot \mathbf{v}_\alpha \quad (3.62)$$

can lead to large errors when atoms move out of the support of a shape function. Additionally, the shape functions need not be updated every time step to reduce computational costs, at the expense of the continuous time evolution for the atomic shape functions. Therefore, the present algorithm enables an entirely new class of problems to be considered within the present AtC framework.

3.4 Thermostat Framework for Energy Conservation

3.4.1 Discrete Thermostats

While understanding the continuous form of the thermostats is useful, arbitrary discretizations of their application during the time integration will not, in general, realize the exact enforcement of the constraints. The principal problem is that the temperature is a quadratic function of the atomic velocity. This can add a biased error between T_I and the coarse-grained atomic temperature proportional to $\Delta t^2 \lambda_I^2$ if λ_I is computed directly from the continuous equations. If uncorrected, this error grows and eventually leads to instability, particularly when Gaussian isokinetic thermostatting is used.

For nodes with temperature coupling without time filtering, the change in temperature arising from application of the thermostat must satisfy the equation

$$M_{IJ}^{MD} \Delta T_{J,C}|_{n+1} = \sum_{\alpha} N_I^{\alpha} \Delta \hat{E}_{\alpha}|_{n+1} + \sum_{\alpha} N_I^{\alpha} \Delta K_{\alpha}^{\lambda}|_{n+1}. \quad (3.63)$$

The constraint equation at each node becomes

$$-\sum_{\alpha} N_I^{\alpha} \Delta K_{\alpha}^{\lambda}|_{n+1} = \sum_{\alpha} N_I^{\alpha} \Delta \hat{E}_{\alpha}|_{n+1} - M_{IJ}^{MD} \Delta T_{J,C}|_{n+1} \equiv L|_{n+1}. \quad (3.64)$$

Using the restriction operator allows us to write a system of equations governing λ_J :

$$\Delta t \sum_{\mathcal{I}} N_I^{\alpha} \tilde{K}_{\alpha}|_{n+1} \sum_{\mathcal{J}} N_J^{\alpha} \lambda_J - \frac{\Delta t^2}{4} \sum_{\mathcal{I}} N_I^{\alpha} \tilde{K}_{\alpha}|_{n+1} \left(\sum_{\mathcal{J}} N_J^{\alpha} \lambda_J \right) \left(\sum_{\mathcal{K}} N_K^{\alpha} \lambda_K \right) = L|_{n+1}. \quad (3.65)$$

For small time steps, the problem can be solved iteratively. The initial guess can be found by solving the linear system and right hand side, ie:

$$\sum_{\mathcal{I}} N_I^{\alpha} \tilde{K}_{\alpha}|_{n+1} \sum_{\mathcal{J}} N_J^{\alpha} \lambda_J^0 = \frac{L|_{n+1}}{\Delta t}, \quad (3.66)$$

which yields the standard equation for λ in the limit of $\Delta t \rightarrow 0$. The i th iteration will then satisfy

$$\sum_{\mathcal{A}} N_I^\alpha \tilde{K}_\alpha \Big|_{n+1} \sum_{\mathcal{J}} N_J^\alpha \lambda_J^i = \frac{L|_{n+1}}{\Delta t} + \frac{\Delta t}{4} \sum_{\mathcal{A}} N_I^\alpha \tilde{K}_\alpha \Big|_{n+1} \left(\sum_{\mathcal{J}} N_J^\alpha \lambda_J^{i-1} \right) \left(\sum_{\mathcal{K}} N_K^\alpha \lambda_K^{i-1} \right). \quad (3.67)$$

Due to the quadratic term this method is not guaranteed to converge. However, for sufficiently small Δt ($\Delta t \lambda \ll 1$), an asymptotic solution does exist. Therefore, if the solver is initialized with the solution without the term linear in Δt , convergence is guaranteed as the time step is refined. This is a consequence of using a linear Gaussian Least constraint in the continuous formulation.

While we have derived the discrete thermostat for the isokinetic case, we can also transform the flux thermostat by determining the amount of energy added by the flux. The continuous equation reads:

$$M_{IJ} \dot{T}_J = \int_{\Gamma} N_I \mathbf{q} \cdot \mathbf{n} dA + \int_{\Omega} N_I g dV, \quad (3.68)$$

which accounts for boundary heat fluxes, \mathbf{q} , due to coupling or prescription, as well as prescribed volumetric heat sources g . Then, the amount of energy input into the system over the time step can be used to compute ΔT_I due to the fluxes. This can then be used on the right-hand side of the equation for λ_I to discretely add the correct amount of energy.

This formulation fits directly within the framework of (3.63) if the total filtered thermostat contribution is applied as the correction to the filtered temperatures:

$$-\Delta \left\langle \sum_{\alpha} N_I^\alpha K_\alpha^\lambda \right\rangle \Big|_{n+1} = L|_{n+1}, \quad (3.69)$$

In the continuous sense, the right-hand side would be the filtered power due to λ , but in the discrete sense the total change with each timestep update must be retained. The filtered contribution from λ is determined with an implicit update in the second half of the timestep. Upon substitution of eq. (3.44),

$$-\frac{\Delta t/\tau}{1 + \Delta t/\tau} \sum_{\alpha} N_I^\alpha K_\alpha^\lambda \Big|_{n+1} = L|_{n+1} + \frac{1}{1 + \Delta t/\tau} \left\langle \sum_{\alpha} N_I^\alpha K_\alpha^\lambda \Big|_n \right\rangle. \quad (3.70)$$

This equation allows λ , which acts in the instantaneous sense on the MD, to be related with the continuous equations which act on the filtered scale. Note that this is slightly different that when continuous equations are used. This right-hand side plays a similar role to the filter inverse present in the continuous equations, but accounts for the discrete dynamics and filter updates that necessarily occur in a simulation.

When the filter is used, the target atomic temperature must also be computed. It is integrated identically to the MD contribution to the continuous temperature except that it is updated using the restricted atomic power rather than the integrated one. This enables the corresponding error to be computed between the purely atomic and continuous temperatures for use with the thermostat. As discussed in [123], it is possible to apply both forms of control simultaneously, however in that work, it was not possible to do so with the control effects localized to the boundary. In Appendix 3.7 a framework is presented which proves there exists such an objective function with the required properties, and provides an algorithm for computing an approximation of it.

3.5 Example Problems

3.5.1 Thermal Conductivity of Liquid Argon

The first application demonstrates how the method can be used to perform non-equilibrium MD calculations to estimate thermal conductivities of atomic fluids. A quasi-1D configuration is arranged, as shown in Fig. 3.1, with dimensions $64.86 \times 32.43 \times 32.43$ Å. The FE mesh is truncated to only overlap the AtC atoms. Fixed boundary atoms are used to constrain the fluid, while the internal atoms are initially arranged in a FCC lattice with a length scale of 6.5 Å. The rescaling thermostat, eq. 3.25, is used to thermalize the system to an initial temperature of 100K by being applied every 10 time steps over a run of 200 time steps (the time step size is 2 fs). Atoms interact with each other using the Lennard-Jones (LJ) potential based on the pairwise distance r^{ij} between atoms i and j ,

$$U^{ij}(r^{ij}) = 4\epsilon \left[\left(\frac{\sigma}{r^{ij}} \right)^{12} - \left(\frac{\sigma}{r^{ij}} \right)^6 \right]. \quad (3.71)$$

The energy, ϵ , is 0.238 Kcal/mole while the length scale, σ , is 3.405 Å. A 13.5 Å cut-off radius is used.

Following the thermal equilibration phase, the temperature at the left-most node is prescribed to rise from 100K to 120K over 40000 fs using the temperature based constraints, eq. (3.16). Time filtering is used to smooth this transition, with a timescale of $\tau = 10000$ fs. By averaging the heat flux applied by the thermostat and the known temperature difference, the thermal conductivity can be estimated to be 1.54×10^{-9} AMU/fs³ K. The resulting temperature profile is shown in Fig. 3.2.

3.5.2 Multiscale Liquid Argon

The conductivity estimated in the previous example can be used to inform a multiscale model. Using the same configuration, except with the FE mesh extended as in Fig. 3.1, a similar problem is considered. Following equilibration, the temperature of the left-most node, which is strictly in Ω_{FE} , is ramped up to 120 K over 40000 fs. Coupling is achieved by means of the flux-based thermostat eq. (3.20). Figure 3.3 illustrates the resulting velocity profile.

3.6 Conclusions

In this work, a fractional step method has been developed for accurately and robustly computing coupled FE/MD problems involving heat transport. Fractional step methods have a significant advantage for multiscale problems due to the attendant different dynamics exhibited at each scale: different physics can be integrated in time using the method most appropriate for each. In this case, the coarse-grained atomic temperature was treated differently from the FE temperature in order to achieve consistency between the dynamic temperature field and the measured temperature

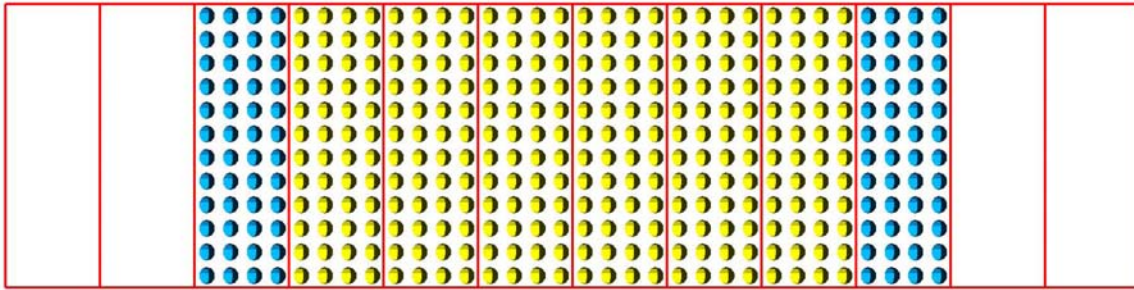


Figure 3.1. Schematic of the quasi-1D test cases used in this work. Atoms which are part of the AtC method are yellow while boundary atoms used to confine the atoms and reflect phonons are in blue. The FE mesh is in red.

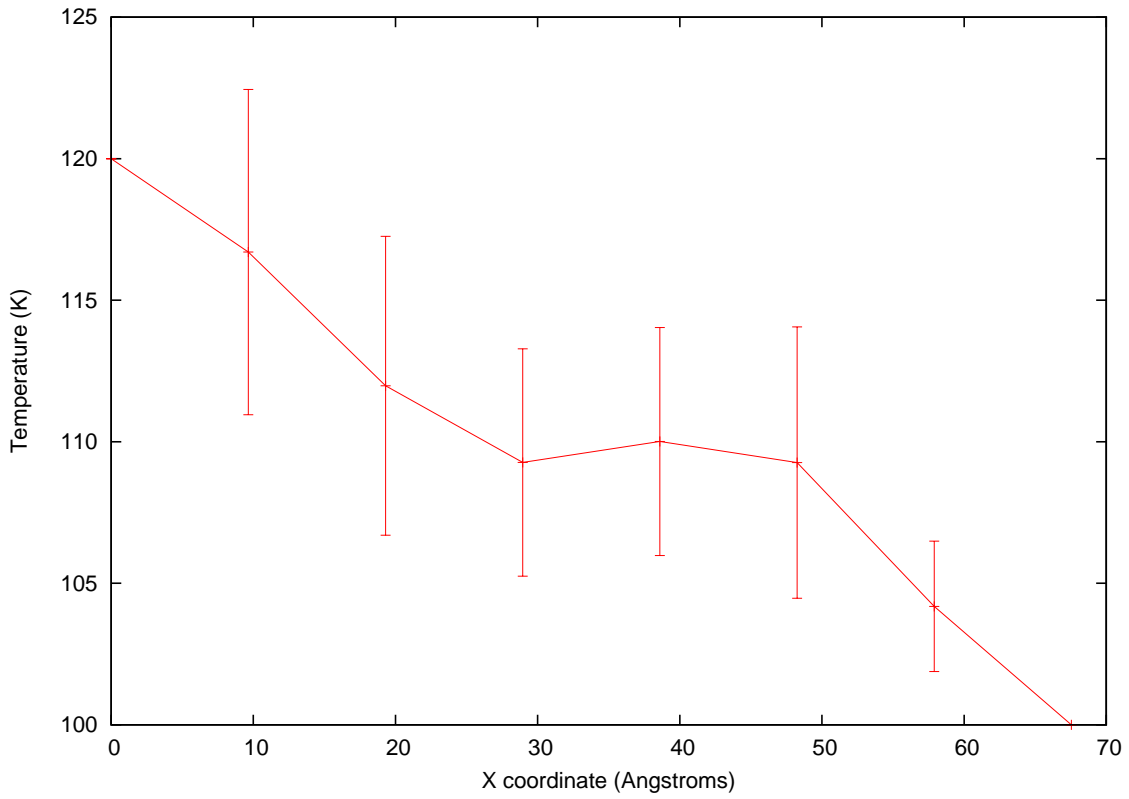


Figure 3.2. Mean and standard deviation of the temperature profile using fixed .

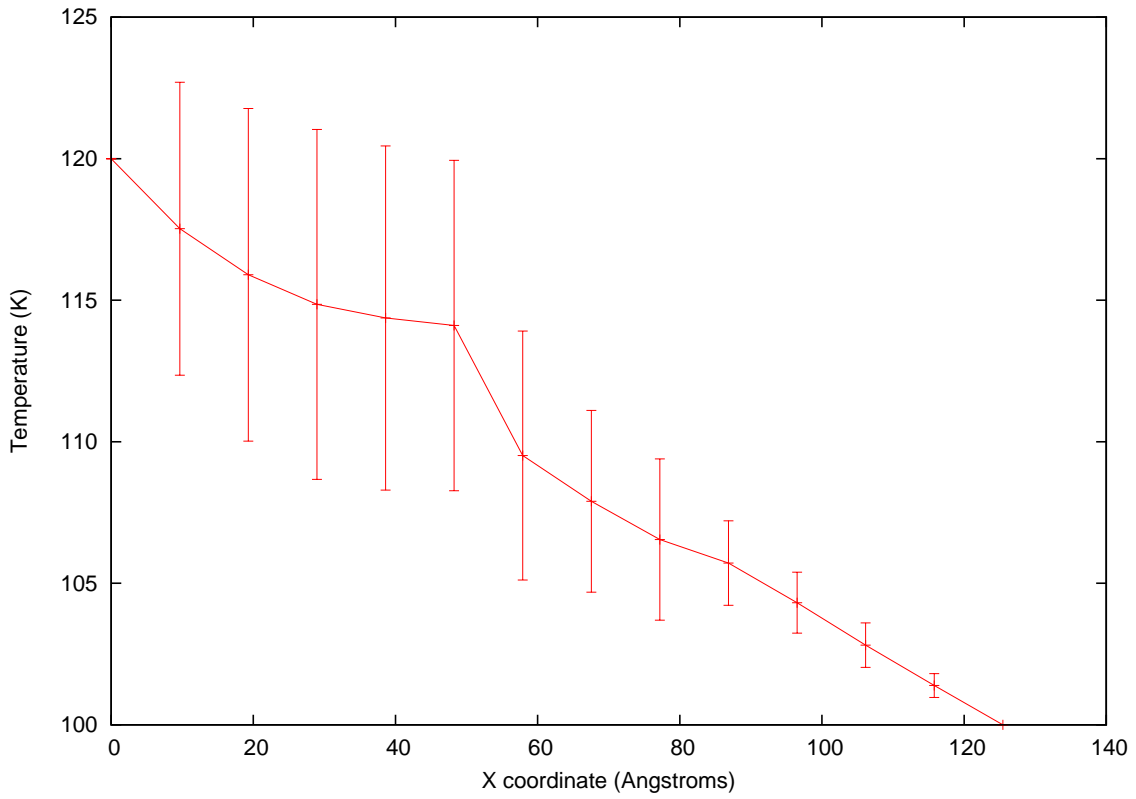


Figure 3.3. Mean and standard deviation of the temperature profile.

of the atoms, leading to long-term numerical stability. Additionally, the approach enabled the use of temperature definitions including the potential energy. As was shown, arbitrary temperature definitions are compatible with this method and an explicit formula for the time derivative is not required.

The fractional step approach also has an advantage in that it prescribes how to subject dynamical equations to constraint in which partial derivatives with respect to time do not appear. For multiscale simulation, this is advantageous because the coupling conditions need not satisfy time evolution equations. The present coupling approach is based on specifying constraints at each time step. By solving for these constraints and applying them in a consistent manner with the fractional step method, they can be enforced to machine precision. Thus, drift between the FE and MD systems is minimized for fixed temperature constraints, while energy can be exactly conserved in exchange between the two. Both properties contribute to enhanced stability as well.

As a demonstration of the method, it was applied to several stressing problems involving both solid and liquid phases. The accuracy of method was demonstrated to be second order in time for the most chaotic cases. Uses of the method were shown to include direct thermal conductivity measurements, transient heating of a liquid, and heat transport at a fluid/solid interface. Future work will apply these techniques to problems of more scientific and technological significance.

3.7 Consistent Formulation for Combined Fixed Temperature/Energy Flux Localized Thermostats

It is important to demonstrate that there exists a unified constraint such that the Dirichlet and Neumann boundary conditions can be used together in a localized constraint. To prove that such a constraint exists, let $\mathcal{C} = \mathcal{C}_D \cup \mathcal{C}_N$ be the set of all nodes at which a constraint is not trivially satisfied, where \mathcal{C}_D and \mathcal{C}_N are non-intersecting sets of nodes at which the matching acceleration (Dirichlet) and stress (Neumann) constraints are desired, respectively. The set of free nodes will be denoted by $\mathcal{F} = \mathcal{I} \setminus \mathcal{C}$. In order to retain the notion of a Gaussian least constraint, the mathematical structure must retain the form of

$$\sum_{\alpha} N_{I\alpha} \sum_J N_{J\alpha} \lambda_J = P_I \quad \forall I, J \in \mathcal{C}. \quad (3.72)$$

Note in this equation λ_I is only non-zero for nodes in \mathcal{C} and zero otherwise. The right-hand side vector P denotes momentum rate of change need to enforce a constraint. It can be decomposed by constraint as

$$P_I = P_I^D + P_I^N \quad (3.73)$$

where only one of P_I^D or P_I^N is non-zero for a given node. These equations can be written succinctly over the subspace \mathcal{C} in matrix notation:

$$M_{\mathcal{C}} \lambda_{\mathcal{C}} = \mathbf{P}_{\mathcal{C}}^D + \mathbf{P}_{\mathcal{C}}^N, \quad (3.74)$$

which due to its linearity admits superposition of solutions

$$\lambda_{\mathcal{C}}^D = M_{\mathcal{C}}^{-1} \mathbf{P}_{\mathcal{C}}^D \quad (3.75)$$

$$\lambda_{\mathcal{C}}^N = M_{\mathcal{C}}^{-1} \mathbf{P}_{\mathcal{C}}^N \quad (3.76)$$

Given this formulation, one mathematical preliminary remains: defining the projection operator from \mathcal{I} to \mathcal{C} . This operator is

$$R = \begin{bmatrix} I_{\mathcal{C}_D} & 0 & 0 \\ 0 & I_{\mathcal{C}_N} & 0 \end{bmatrix} \quad (3.77)$$

where each identity matrix is appropriately sized based on the dimensionality of its sub-space. The matrix R^T then takes a vector in \mathcal{C} to \mathcal{I} with zero entries in the non-coincident nodes. It will be of use later to write

$$R^T R = \begin{bmatrix} I_{\mathcal{C}_D} & 0 & 0 \\ 0 & I_{\mathcal{C}_N} & 0 \\ 0 & 0 & 0 \end{bmatrix}, \quad (3.78)$$

which transforms a vector in \mathcal{I} back to a vector in \mathcal{C} with zero entries at unconstrained nodes.

To begin the analysis, consider the statement of global energy conservation in matrix notation is

$$\mathbf{1} \cdot M \lambda^N = \mathbf{1} \cdot \mathbf{P}^N, \quad (3.79)$$

where the equation is defined over all the nodes, M is the standard matrix in the equation for λ (e.g., in eq. (3.17)), and $\mathbf{1}$ is a row vector of 1's with length corresponding to the cardinality of \mathcal{I} . This equation can be related to eq. (3.74) by using eq. (3.77):

$$\mathbf{1} \cdot MR^T \lambda_{\mathcal{C}}^N = \mathbf{1} \cdot \mathbf{P}^N, \quad (3.80)$$

and further by using eq. (3.76):

$$\mathbf{1} \cdot MR^T M_{\mathcal{C}}^{-1} \mathbf{P}_{\mathcal{C}}^N = \mathbf{1} \cdot \mathbf{P}^N. \quad (3.81)$$

Inspired by this form, assume a relationship between the localized and global forces to be

$$\mathbf{P}_{\mathcal{C}}^N = M_{\mathcal{C}} R \tilde{M}^{-1} \mathbf{P}^N. \quad (3.82)$$

What remains is to determine an approximate mass matrix, \tilde{M} such that eq. (3.79) is satisfied.

To begin, substitute eq. (3.82) into the left-hand side of eq. (3.81):

$$\begin{aligned} \mathbf{1} \cdot MR^T M_{\mathcal{C}}^{-1} \mathbf{P}_{\mathcal{C}}^N &= \mathbf{1} \cdot MR^T M_{\mathcal{C}}^{-1} M_{\mathcal{C}} R \tilde{M}^{-1} \mathbf{P}^N \\ &= \mathbf{1} \cdot MR^T R \tilde{M}^{-1} \mathbf{P}^N. \end{aligned}$$

To proceed further, note that the symmetric mass matrix is

$$M = \begin{bmatrix} M_{\mathcal{C}} & M_{\mathcal{F}\mathcal{C}} \\ M_{\mathcal{F}\mathcal{C}}^T & M_{\mathcal{F}} \end{bmatrix}. \quad (3.83)$$

Therefore,

$$\begin{aligned}
\mathbf{1} \cdot MR^T M_{\mathcal{C}}^{-1} \mathbf{P}_{\mathcal{C}}^N &= \mathbf{1} \cdot \begin{bmatrix} M_{\mathcal{C}} & M_{\mathcal{F}\mathcal{C}} \\ M_{\mathcal{F}\mathcal{C}}^T & M_{\mathcal{F}} \end{bmatrix} \begin{bmatrix} I_{\mathcal{C}} & 0 \\ 0 & 0 \end{bmatrix} \tilde{M}^{-1} \mathbf{P}^N \\
&= \mathbf{1} \cdot \begin{bmatrix} M_{\mathcal{C}} & 0 \\ M_{\mathcal{F}\mathcal{C}}^T & 0 \end{bmatrix} \tilde{M}^{-1} \mathbf{P}^N \\
&= \mathbf{1} \cdot \begin{bmatrix} M_{\mathcal{C}} & 0 \\ M_{\mathcal{F}\mathcal{C}}^T & 0 \end{bmatrix} \begin{bmatrix} \tilde{M}_{\mathcal{C}} & \tilde{M}_{\mathcal{F}\mathcal{C}} \\ \tilde{M}_{\mathcal{C}\mathcal{F}} & \tilde{M}_{\mathcal{F}} \end{bmatrix}^{-1} \begin{bmatrix} \tilde{\mathbf{P}}_{\mathcal{C}}^N \\ 0 \end{bmatrix}.
\end{aligned}$$

Here the notation $\tilde{\mathbf{P}}_{\mathcal{C}}^N = \mathbf{R}\mathbf{P}^N$ is used to denote the original non-zero constraint values, distinct $\mathbf{P}_{\mathcal{C}}^N$ as defined by eq. (3.82). Given the form of the equation, only $\tilde{M}_{\mathcal{C}}$ will be of importance in the final expression, so let $\tilde{M}_{\mathcal{F}\mathcal{C}} = \tilde{M}_{\mathcal{C}\mathcal{F}} = 0$ and $\tilde{M}_{\mathcal{F}} = I_{\mathcal{F}}$. Then the expression is reduced to

$$\begin{aligned}
\mathbf{1} \cdot MR^T M_{\mathcal{C}}^{-1} \mathbf{P}_{\mathcal{C}}^N &= \mathbf{1} \cdot \begin{bmatrix} M_{\mathcal{C}} & M_{\mathcal{F}\mathcal{C}} \\ M_{\mathcal{F}\mathcal{C}}^T & M_{\mathcal{F}} \end{bmatrix} \begin{bmatrix} \tilde{M}_{\mathcal{C}}^{-1} & 0 \\ 0 & I_{\mathcal{F}} \end{bmatrix} \begin{bmatrix} \tilde{\mathbf{P}}_{\mathcal{C}}^N \\ 0 \end{bmatrix} \\
&= \mathbf{1} \cdot \begin{bmatrix} M_{\mathcal{C}} & M_{\mathcal{F}\mathcal{C}} \\ M_{\mathcal{F}\mathcal{C}}^T & M_{\mathcal{F}} \end{bmatrix} \begin{bmatrix} \tilde{M}_{\mathcal{C}}^{-1} \tilde{\mathbf{P}}_{\mathcal{C}}^N \\ 0 \end{bmatrix} \\
&= \mathbf{1} \cdot \begin{bmatrix} M_{\mathcal{C}} \tilde{M}_{\mathcal{C}}^{-1} \tilde{\mathbf{P}}_{\mathcal{C}}^N \\ M_{\mathcal{F}\mathcal{C}}^T \tilde{M}_{\mathcal{C}}^{-1} \tilde{\mathbf{P}}_{\mathcal{C}}^N \end{bmatrix}.
\end{aligned}$$

The two terms in the final matrix have clear interpretations. The first term is the fraction of the constraint force that will remain local to the constrained nodes after application to the atoms, while the second term is amount that will “leak” to adjacent nodes. In this context, adjacent nodes means nodes in \mathcal{F} whose support overlaps nodes in \mathcal{C} . In order to correctly account for this leakage, define the lumping matrix L which takes vectors in \mathcal{F} to \mathcal{C} such that the sum of each column is unity, i.e., it partitions the components amongst nodes in \mathcal{F} while maintaining the total sum. If $\mathbf{1}_{\mathcal{C}}$ is vector of ones with length corresponding to the cardinality of \mathcal{C} , then

$$\begin{aligned}
\mathbf{1} \cdot MR^T M_{\mathcal{C}}^{-1} \mathbf{P}_{\mathcal{C}}^N &= \mathbf{1}_{\mathcal{C}} \cdot (M_{\mathcal{C}} \tilde{M}_{\mathcal{C}}^{-1} \tilde{\mathbf{P}}_{\mathcal{C}}^N + LM_{\mathcal{F}\mathcal{C}}^T \tilde{M}_{\mathcal{C}}^{-1} \tilde{\mathbf{P}}_{\mathcal{C}}^N) \\
&= \mathbf{1}_{\mathcal{C}} \cdot (M_{\mathcal{C}} + LM_{\mathcal{F}\mathcal{C}}^T) \tilde{M}_{\mathcal{C}}^{-1} \tilde{\mathbf{P}}_{\mathcal{C}}^N
\end{aligned}$$

which satisfies energy conservation if (but not only if)

$$\tilde{M}_{\mathcal{C}} = M_{\mathcal{C}} + LM_{\mathcal{F}\mathcal{C}}^T. \quad (3.84)$$

For this to be a general method, it is also necessary for the boundary flux computations (see Eq. 45 in [129]) to be localized as well due to the presence of the consistent mass and stiffness matrices on its right-hand side. To demonstrate how this quantity can also be localized, consider the unknown finite element heat flux, \mathbf{q}^h , is given by

$$\int_{\partial\Omega_{fem}} N_I \mathbf{q}^h \cdot \mathbf{n}_{MD} dS = - \int_{\Omega_{md}} N_I \nabla \cdot \mathbf{q}^h dV - \int_{\Omega_{md}} \nabla N_I \cdot \mathbf{q}^h dV. \quad (3.85)$$

To estimate the unknown heat flux divergence, a finite element approximate function is used:

$$\mathbf{L}(\mathbf{x}) = \sum_I N_I \mathbf{L}_I \approx \nabla \cdot \mathbf{q}^h, \quad (3.86)$$

which must satisfy

$$\int_{\Omega} N_I \sum_J N_J \mathbf{L}_J dV \approx \int_{\Omega} N_I \nabla \cdot \mathbf{q}^h dV, \quad (3.87)$$

which is further approximated using row-sum lumping:

$$\int_{\Omega} N_I \mathbf{L}_I dV = \int_{\Omega} N_I \nabla \cdot \mathbf{q}^h dV, \quad (3.88)$$

Noting that \mathbf{q}^h is zero by construction on the boundaries, row-sum lumping of the left-hand side and integration by parts of the right-hand side provides an expression for the unknown function

$$\mathbf{L}_I = -V_I^{-1} \int_{\Omega} \nabla N_I \cdot \mathbf{q}^h dV, \quad (3.89)$$

where V_I^{-1} is the inverse of the lumped mass matrix. Substituting Eq. (3.89) into Eq. (3.88), and that result into Eq. (3.85), a localized approximate reconstruction is obtained:

$$\int_{\partial\Omega_{fem}} N_I \mathbf{q}^h \cdot \mathbf{n}_{MD} dS = \int_{\Omega_{md}} N_I V_I^{-1} \left(\int_{\Omega} \nabla N_I' \cdot \mathbf{q}^h dV' \right) dV - \int_{\Omega_{md}} \nabla N_I \cdot \mathbf{q}^h dV. \quad (3.90)$$

This equation can be simplified into weighted integrals of the FE heat flux in Ω_{fem} and Ω_{md} which provides a more illuminating and computationally straightforward equation for the heat flux from the FE region into the MD region:

$$\int_{\partial\Omega_{fem}} N_I \mathbf{q}^h \cdot \mathbf{n}_{MD} dS = \frac{V_I^{MD}}{V_I} \int_{\Omega_{fem}} \nabla N_I \cdot \mathbf{q}^h dV + \left(\frac{V_I^{MD}}{V_I} - 1 \right) \int_{\Omega_{md}} \nabla N_I \cdot \mathbf{q}^h dV \quad (3.91)$$

Inspired by this result, a more efficient approach is taken in which a two step approach will be used to guarantee locality and global energy conservation. However, this approximation will not exactly correspond to a Gaussian least constraint problem posed at the nodes. The first step solves the Neumann problem by fully lumping the mass matrix, followed by a fully matrix solution of the Dirichlet problem including the Neumann nodes with zeros in the right-hand side.

Chapter 4

A Method for Atomistic-to-Continuum Combined Thermal and Mechanical Coupling

4.1 Introduction

Increasing interest in nanotechnology motivates development of simulation capabilities which can investigate and assess device performance in the context of physics which are greatly different than those at the macroscale. One avenue to account for these differences is multiscale modeling, which in the context of nanosystems implies utilization of an expensive discrete model in regions where the dynamics of atoms are important, and a less expensive continuum model where materials can be effectively modeled using field theories. An important distinction between these types of physics are that continuum models can represent only a small number of the governing state variables, e.g. velocity, while other variables such as temperature are only accounted for implicitly through constitutive models. By contrast, atomic descriptions of matter require all the state variables to be specified because the trajectory of each particle must be simulated.

In terms of atomistic-to-continuum (AtC) modeling, this implies that even only one set of variables is of interest, all must be included in the computation for the atoms to have accurate dynamics. A simple example is the canonical shear flow in which a fluid is driven across a no-slip boundary by means of a slip velocity above it, referred to as Couette flow. The continuum solution can be obtained solely by considering the fluid's velocity, with the temperature only informing the equations through the thermodynamic properties of density and viscosity. Because work is continuously being done on the fluid, energy is transformed into heat on a continuous basis. Continuum Navier-Stokes models omitting the degrees of freedom of the temperature are well-posed, however, an atomic model will eventually break-down due to infinite addition of heat, which implies increasingly large atomic kinetic energy. Hence, a means to correctly remove heat is required. Common thermostats, e.g. Nose-Hoover [47], are inappropriate for such an inhomogeneous system because the effective fluid viscosity increases within a few nanometers of the wall due to discrete packing effects, so heat is non-uniformly generated while the thermostat removes heat uniformly.

The solution proposed in this paper is to develop an AtC framework which can transfer momen-

The primary authors of this chapter are J. Templeton, R. Jones, and J. Zimmerman.

tum and energy between a molecular dynamics (MD) representation of the atoms and a continuum finite element (FE) description of velocity and temperature fields. This approach builds upon the substantial progress made in AtC modeling within the last two decades. In particular, many techniques exist for quasi-zero temperature mechanical coupling, often motivated by capturing the impact of material defects on devices. A review article by Miller & Tadmor [93] compares and contrasts many of these methods. Generally speaking, they categorize them into methods which interact via forces versus those which interact via energy, usually by modifying the system Hamiltonian. This work favors the former approach, as writing a continuum Hamiltonian including temperature is non-trivial. For comparative purposes, the momentum equations within the present method are most similar to the bridging scale method [130], which performed well in Miller & Tadmor’s test suite.

While less mature, AtC methods for temperature have also been proposed. The popular quasi-continuum method was modified for using temperature as a primary variable by Kulkarni *et al.* [71]. An extension of the bridging scale method has also been made for simulating heat transfer between and MD and FE region [102]. Recently, Anciaux *et al.* [2] developed a temperature coupling scheme based on the bridging domain method. The preceding methods focused on temperature coupling in solids. Iterative AtC approaches for fluid mechanics have also been constructed [80, 131]. For the reasons previously given, these approaches use thermostats to regulate the MD temperature and eliminate the excess energy generated by shear.

In a series of recent papers, Kobayashi *et al.* [68, 69] developed a concurrent finite temperature mechanical coupling method a hybrid molecular dynamics/coarse-grained particle method. Their primary motivation was crack propagation, which requires treatment of waves moving between the MD and coarse-grained region which are of sufficiently small frequency to be unrepresentable at the continuum scale. Their approach used a Langevin thermostat applied to a set of “extra” atoms with the difference between the continuum and atomistic velocities used to inform the dissipation terms. 2D Lennard-Jones and graphene crack growth problems have thus far been treated using this technique. Rizzi *et al.* [110] have also derived a method to simultaneously prescribe a temperature and velocity to atoms within a specified region and applied their method to simulate salt water flow through a nanopore. Their method also provides for the concentration of constituent species to be regulated in this region. However, the approach is based on fixed volumes within the MD domain rather than being derived for multiscale modeling.

The framework proposed in this paper is based upon combining previous efforts in MD/FE coupling for temperature ([129, 123]. Both approaches consider a domain Ω fully overlaid with a FE mesh with a subset containing atoms, with approximation of the integral over the atoms given by appropriate summations. Coupling is achieved by integrating by parts in the continuum, which provides a surface flux from the FE to MD regions. The flux is imposed on the atoms by means of modifying the forces they experience to conserve the desired quantity. Section 4.2 provides the unified mathematical description of the combined MD/FE system tracking both momentum and energy. Correctly coupling the MD and FE regions necessitates developing a regulation scheme which can exactly and locally provide an exact stress or heat flux to the atoms, and is presented in Section 4.3. Details are provided on the time integration schemes used to advance the equations in Sections: integration, followed by some example problems in Section 4.5. Finally, a few concluding

thoughts are offered in Section 4.6.

4.2 Coupled Finite Element/Atomistic Momentum and Temperature Equations

In developing the present multiscale formalism, we follow the approach of [129] and present the results for the displacement and velocity, which have not been previously derived in this framework. The temperature equation is nearly identical to that found in Chapter 3, and the result will be quoted at the end of this section with emphasis on the ways it differs when performing combined thermal/mechanical coupling. First, consider a finite element space spanned by shape functions (basis functions) N_I such that all functions in the space can be expressed as:

$$\mathbf{P}^h(\mathbf{x}) = \sum_I N_I(\mathbf{x}) \mathbf{P}_I, \quad (4.1)$$

where \mathbf{P}_I are the nodal values of the finite element momentum density field. They are obtained by minimizing the mean-squared difference between the continuous field \mathbf{P} and the FE approximation:

$$\min_{\mathbf{P}_I} \int_{\Omega} \left(\mathbf{P}(\mathbf{x}) - \mathbf{P}^h(\mathbf{x}) \right)^2 dV. \quad (4.2)$$

The nodal velocities are then given by the least-squares solution

$$\sum_J \int_{\Omega} N_I N_J \mathbf{P}_J dV = \int_{\Omega} N_I \mathbf{P}(\mathbf{x}) dV. \quad (4.3)$$

In order to relate the integral on the right-hand side of eq. (4.3) to a set of discrete atomic momenta, it is necessary to define an equivalent momentum density associated with an atom. This is done by considering atom α to have an associated volume ΔV_{α} , enabling the definition of the atomic momentum density to be

$$\mathbf{P}(\mathbf{x}_{\alpha}) \approx \delta(\mathbf{x}_{\alpha}) \rho_{\alpha} \mathbf{v}_{\alpha}, \quad (4.4)$$

where ρ_{α} is the approximate mass density of atom α , \mathbf{c}_{α} is its velocity, \mathbf{x}_{α} is its reference position, and δ is the Dirac delta function. When applied to eq. (4.3), a mathematical connection is established between the continuous FE field and the discrete representation of the atoms

$$\sum_J \sum_{\alpha} N_I \alpha N_J \alpha \mathbf{P}_J \Delta V_{\alpha} \approx \sum_{\alpha} N_I \alpha \rho_{\alpha} \mathbf{v}_{\alpha} \Delta V_{\alpha} \quad (4.5)$$

by using an approximate quadrature for the integral. The shorthand $N_{I\alpha} = N_I(\mathbf{x}_{\alpha})$ has been used to simplify the notation.

To complete the mathematical framework, the assumption that the volume for each atom is

chosen to be consistent with the density, e.g.. $\rho_\alpha = m_\alpha/\Delta V_\alpha$. Then letting $\mathbf{P}_\alpha = \rho_\alpha \mathbf{V}_I$, with \mathbf{V}_I being the nodal velocities,

$$\sum_J \sum_\alpha N_{I\alpha} N_{J\alpha} m_\alpha \mathbf{V}_I \approx \sum_\alpha N_{I\alpha} m_\alpha \mathbf{v}_\alpha. \quad (4.6)$$

For an extended domain in which the finite elements cover Ω while the atoms exist within a subset $\Omega_{MD} \subset \Omega$, the integral over the entire system is divided into part over the FE domain, $\Omega_{FE} = \Omega \setminus \Omega_{MD}$:

$$\int_\Omega N_I N_J \mathbf{P}_J dV \equiv \int_{\Omega_{FE}} N_I N_J \rho \mathbf{V}_J dV + \sum_\alpha N_{I\alpha} N_{J\alpha} m_\alpha \mathbf{V}_I \quad (4.7)$$

To incorporate dynamics, let

$$\rho \dot{\mathbf{V}}(\mathbf{x}) = \nabla \cdot \boldsymbol{\sigma}(\mathbf{x}) \quad (4.8)$$

$$m_\alpha \dot{\mathbf{v}}_\alpha = \mathbf{f}_\alpha \quad (4.9)$$

Then the nodal variable dynamics are given by

$$\sum_J \left(\int_{\Omega_{FE}} N_I N_J \rho \dot{\mathbf{V}}_J dV + \sum_\alpha N_{I\alpha} N_{J\alpha} m_\alpha \dot{\mathbf{V}}_J \right) = \int_{\Omega_{FE}} N_I \nabla \cdot \boldsymbol{\sigma}(\mathbf{x}) dV + \sum_\alpha N_{I\alpha} \mathbf{f}_\alpha. \quad (4.10)$$

However, this equation cannot be solved computationally since $\boldsymbol{\sigma}(\mathbf{x})$ is not known. Instead, this quantity is approximated with its FE representation, and in this work, either linear elasticity,

$$\boldsymbol{\sigma}(\mathbf{x}) \approx \kappa \sum_J \nabla N_J \mathbf{U}_J, \quad (4.11)$$

or linear viscosity,

$$\boldsymbol{\sigma}(\mathbf{x}) \approx \mu \sum_J \nabla N_J \mathbf{V}_J, \quad (4.12)$$

Note that using this definition leads to the following expression for conservation of mass

$$\begin{aligned} \int_{\Omega_{md}} N_I N_J \rho_J dV &\approx \sum_\alpha N_{I\alpha} N_{J\alpha} \rho_J \Delta V_\alpha = \sum_\alpha N_{I\alpha} \rho_\alpha \Delta V_\alpha \\ &= \sum_\alpha N_{I\alpha} m_\alpha, \end{aligned}$$

while the atomic volumes would satisfy a consistency constraint,

$$\int_{\Omega_{md}} N_I N_J dV = \sum_\alpha N_{I\alpha} N_{J\alpha} \Delta V_\alpha.$$

However, neither are needed when using eq. (4.6). Also note there is no explicit constraint forcing the atomic tributary volume used to assess the atomic mass density to equal the atomic quadrature volume used to approximate volumetric integrals as discrete atomic sums. Doing so is a choice which simplifies the mathematics but also results in consistency between the finite element projection and standard averaging operators.

will be used for the stress tensor. Additionally, density in the MD domain will be assumed constant in Lagrangian frame calculations. Therefore, after integrating the stress term by parts, the FE governing equation is

$$\sum_J \left(\int_{\Omega_{FE}} N_I N_J \rho \dot{\mathbf{V}}_J dV + \sum_{\alpha} N_{I\alpha} N_{J\alpha} m_{\alpha} \dot{\mathbf{V}}_J \right) = - \int_{\Omega_{FE}} \nabla N_I \otimes \boldsymbol{\sigma} dV + \int_{\partial\Omega_{MD}} N_I \boldsymbol{\sigma} \otimes \mathbf{n}_{MD} dA + \sum_{\alpha} N_{I\alpha} \mathbf{f}_{\alpha}. \quad (4.13)$$

The unknown stress across the the boundary of the FE and MD regions, $\partial\Omega_{MD}$, will be determined in the next section.

The coupled FE equations used in this work are those for the nodal velocities, \mathbf{V}_I , for which eq. (4.13) can be written using the short-hand

$$\frac{\partial}{\partial t} M_{IJ}^V \mathbf{V}_J = - \int_{\Omega_{FE}} \nabla N_I \otimes \boldsymbol{\sigma} dV + \int_{\partial\Omega_{FE}} N_I \boldsymbol{\sigma} \otimes \mathbf{n} dS + \sum_{\alpha} N_{I\alpha} \mathbf{f}_{\alpha}, \quad (4.14)$$

and the temperature equation for the nodal temperatures, T_I , as derived in Chapter 3,

$$\frac{\partial}{\partial t} M_{IJ}^T T_J = - \int_{\Omega_{FE}} \nabla N_I \cdot \mathbf{q} dV + \int_{\partial\Omega_{FE}} N_I \mathbf{q} \cdot \mathbf{n} dS + \sum_{\alpha} N_{I\alpha} e'_{\alpha}. \quad (4.15)$$

The mass matrices are also decomposed between the FE and MD domains, and when using the Galerkin procedure [49] they are:

$$M_{IJ}^V = \int_{\Omega_{FE}} N_I \rho N_J + \sum_{\alpha} N_{I\alpha} m_{\alpha} N_{J\alpha} \quad (4.16)$$

$$M_{IJ}^T = \int_{\Omega_{FE}} N_I \rho c_p N_J + \sum_{\alpha} N_{I\alpha} 3k_B N_{J\alpha}. \quad (4.17)$$

In the preceding equations, N_I is the shape function associated with the I th node evaluated a spatial location while $N_{I\alpha}$ is evaluated at the location of atom α , $\boldsymbol{\sigma}$ is the stress, \mathbf{q} the heat flux, ρ the density, c_p the specific heat capacity, k_B is the Boltmann constant, \mathbf{f}_{α} is the force on atom α , while e'_{α} is a measure of its fluctuating energy. Derivation of these equations can be found in the indicated references.

In order to develop the present theoretical framework, a definition is required for e'_{α} . For simplicity, a kinetic definition will be used which is reasonable if equipartition holds and I th shape function's support contains a large number of atoms. Kinetic temperatures are based on multiples of the kinetic energy only, in this case two times it:

$$e'_{\alpha} = m_{\alpha} |\mathbf{v}'_{\alpha}|^2, \quad (4.18)$$

where m_{α} is the atomic mass and \mathbf{v}'_{α} is the atom's fluctuating velocity. (Using more general definitions of temperature, i.e. including potential energy contributions, can be fit into this framework

in a straightforward manner by using the procedure in Chapter 3.) A convenient choice for the fluctuating velocity is first to define the “mean” velocity of an atom based on the FE velocity:

$$\bar{\mathbf{v}}_\alpha \equiv \sum_I N_{I\alpha} \mathbf{V}_I. \quad (4.19)$$

The deviation of the atomic velocity, \mathbf{v}_α from this “mean” is the fluctuating velocity

$$\mathbf{v}'_\alpha = \mathbf{v}_\alpha - \bar{\mathbf{v}}_\alpha. \quad (4.20)$$

This definition of the fluctuating kinetic energy, while not completely consistent with temperature as a thermodynamic variable, nonetheless is consistent and meaningful within the multiscale context. It enables the kinetic energy of an atom, $k_\alpha = 1/2m_\alpha |\mathbf{v}'_\alpha|^2$, to be decomposed into mean and fluctuating parts via the following equations

$$\dot{k}_\alpha = \bar{\mathbf{v}}_\alpha \cdot \mathbf{f}_\alpha \quad (4.21)$$

$$k'_\alpha = \mathbf{v}'_\alpha \cdot \mathbf{f}_\alpha. \quad (4.22)$$

Most notably in contrast to thermodynamic theory, the fluctuating kinetic energy, and hence the temperature, is not independent of the length scales associated with the FE mesh. However defining it in terms of the FE basis will have advantages in modifying the MD forces to enable coupling with the FE.

Before turning to adjustment of the MD forces based on the FE state, it is important to note that in this work all the mass matrices are row-sum lumped [49]. While this was also the case in the previously cited works, doing so has specific implications in this effort. Row-sum lumping is used to diagonalize mass matrices by summing all the entries in a row and “lumping” the result on the diagonal:

$$M_{IJ}^V = \delta_{IJ} \left(\int_{\Omega^{FE}} N_I \rho + \sum_\alpha N_{I\alpha} m_\alpha \right) \quad (4.23)$$

$$M_{IJ}^T = \delta_{IJ} \left(\int_{\Omega^{FE}} N_I \rho c_p + \sum_\alpha N_{I\alpha} 3k_B \right), \quad (4.24)$$

with δ_{IJ} being one if $I = J$ and zero otherwise. In AtC approaches, it has the advantage of localizing the effects of the atoms such that each atom only contributes to shape functions whose support overlaps with the element in which they reside. This is particularly useful in that when modifying the atoms to be consistent with the FE state, only those atoms in elements near $\partial\Omega^{FE}$ must be adjusted so that the majority of atoms can evolve according to their unadulterated equations of motion. However, row-sum lumping means that the FE approximation to a function is no longer a project, i.e., $\bar{\mathbf{v}}$ and \mathbf{v}' are not orthogonal with respect to functions in the FE basis. As a result, a spatially-varying kinetostat cannot be derived independently of the existing spatially-varying thermostats in [129, 123] meaning a combined coupling algorithm is required.

4.3 Combined Kinetostat/Thermostats

4.3.1 Direct Temperature and Velocity Imposition

Considering the extraction of the FE variables as an approximate projection of MD quantities only, the nodal fields are

$$M_{IJ,\alpha}^T T_J = \sum_{\alpha} N_{I\alpha} m_{\alpha} (\mathbf{v}_{\alpha} - \bar{\mathbf{v}}_{\alpha})^2 \quad (4.25)$$

$$M_{IJ,\alpha}^V \mathbf{V}_J = \sum_{\alpha} N_{I\alpha} m_{\alpha} \mathbf{v}_{\alpha}, \quad (4.26)$$

where the mass matrix notation is short-hand for the atomic contribution in eqs. (4.23) and (4.24),

$$M_{IJ,\alpha}^V \mathbf{V}_J \equiv \sum_{\alpha} N_{I\alpha} m_{\alpha} \mathbf{V}_I$$

$$M_{IJ,\alpha}^T T_J \equiv \delta_{IJ} \sum_{\alpha} N_{I\alpha} 3k_B T_I,$$

Following the derivation of successful regulation of atomic velocities to conform to specified FE temperatures [129], assume a modified atomic velocity of the form

$$\mathbf{v}_{\alpha}^* = \sqrt{r_{\alpha}} \mathbf{v}'_{\alpha} + \mathbf{s}_{\alpha}, \quad (4.27)$$

recalling $\mathbf{v}'_{\alpha} \equiv \mathbf{v}_{\alpha} - \bar{\mathbf{v}}_{\alpha}$, such that $r_{\alpha} \equiv \sum_I N_{I\alpha} r_I$ is a velocity rescaling factor while $\mathbf{s}_{\alpha} \equiv \sum_I N_{I\alpha} \mathbf{s}_I$ corrects the streaming velocity.

When applying this regulation scheme, the FE fields are held fixed so the equations for the rescaling and streaming parameters are

$$M_{IJ,\alpha}^V \mathbf{V}_J = \sum_{\alpha} N_{I\alpha} m_{\alpha} (\sqrt{r_{\alpha}} \mathbf{v}'_{\alpha} + \mathbf{s}_{\alpha}), \quad (4.28)$$

$$M_{IJ,\alpha}^T T_J = \sum_{\alpha} N_{I\alpha} m_{\alpha} (\sqrt{r_{\alpha}} \mathbf{v}'_{\alpha} + \mathbf{s}_{\alpha} - \bar{\mathbf{v}}_{\alpha})^2. \quad (4.29)$$

Because $\bar{\mathbf{v}}_{\alpha} \equiv \sum_I N_{I\alpha} \mathbf{V}_I$, it does not change as a result of applying this transformation. The temperature equation can be rewritten as

$$M_{IJ,\alpha}^T T_J = \sum_{\alpha} N_{I\alpha} m_{\alpha} \left(r_{\alpha} \mathbf{v}'_{\alpha}{}^2 + 2\sqrt{r_{\alpha}} \mathbf{v}'_{\alpha} \cdot (\mathbf{s}_{\alpha} - \bar{\mathbf{v}}_{\alpha}) + |\mathbf{s}_{\alpha} - \bar{\mathbf{v}}_{\alpha}|^2 \right). \quad (4.30)$$

It is anticipated that the difference between the streaming atomic velocity and the streaming correct term will be small, which suggests an iterative solution process. Begin by setting $\mathbf{s}_I = \mathbf{V}_I$. Then put eq. 4.30 into a form which can be solved for the next iteration of r_I :

$$\sum_{\alpha} N_{I\alpha} m_{\alpha} \mathbf{v}'_{\alpha}{}^2 \sum_J N_{J\alpha} r_J^{n+1} = M_{IJ,\alpha}^T T_J - \sum_{\alpha} N_{I\alpha} m_{\alpha} \left(2\sqrt{r_{\alpha}} \mathbf{v}'_{\alpha} \cdot (\mathbf{s}_{\alpha}^n - \bar{\mathbf{v}}_{\alpha}) + |\mathbf{s}_{\alpha}^n - \bar{\mathbf{v}}_{\alpha}|^2 \right). \quad (4.31)$$

Equation 4.28 can then be used to solve for the streaming correction:

$$\sum_{\alpha} N_{I\alpha} m_{\alpha} \sum_J N_{J\alpha} \mathbf{s}_J^{n+1} = M_{IJ,\alpha}^V \mathbf{V}_J - \sum_{\alpha} N_{I\alpha} m_{\alpha} \sqrt{r_{\alpha}^{n+1}} \mathbf{v}'_{\alpha} \quad (4.32)$$

Adjusting these equations to account for more general temperature definitions, so long as they contain a kinetic energy contribution, is straightforward (Chapter 3).

4.3.2 Constraint-Based Atomistic-to-Continuum Coupling

Following previous efforts [129, 123], coupling between the MD and FE representations can be effectively mediated by satisfying coupling constraints. These constraints arise from two sources: 1) ensuring the evolution of the FE and coarse-grained atomistic fields' primary variables is consistent, or 2) by preserving fluxes of conserved quantities across the MD/FE interface. The first set of constraints is

$$g_I^{V,1} = \frac{\partial}{\partial t} \left(\sum_{\alpha} N_{I\alpha} m_{\alpha} \mathbf{v}_{\alpha} - M_{IJ,\alpha}^V \mathbf{V}_J \right) \equiv \sum_{\alpha} N_{I\alpha} \mathbf{f}_{\alpha}^* - \frac{\partial}{\partial t} M_{IJ,\alpha}^V \mathbf{V}_J = 0, \quad (4.33)$$

$$g_I^{T,1} = \frac{\partial}{\partial t} \left(\sum_{\alpha} N_{I\alpha} m_{\alpha} |\mathbf{v}'_{\alpha}|^2 - M_{IJ,\alpha}^T T_J \right) \equiv \sum_{\alpha} N_{I\alpha} \mathbf{v}'_{\alpha} \cdot \mathbf{f}_{\alpha}^* - \frac{1}{2} \frac{\partial}{\partial t} M_{IJ,\alpha}^T T_J = 0. \quad (4.34)$$

The \cdot^* notation is used to denote the modified atomic velocity satisfying the constraints, while short-hand expressions for the atomic momentum and kinetic energy have been introduced to aid in connecting the different coupling methodologies to a common mathematical framework.

Constraints of the second type are based conserved quantities, in this case momentum and energy:

$$g^{V,2} = \frac{\partial}{\partial t} \left(\sum_{\alpha} \mathbf{p}_{\alpha} + \sum_I \int_{\Omega^{FE}} M_{IJ}^V \mathbf{V}_J dV \right) = 0 \quad (4.35)$$

$$g^{T,2} = \frac{\partial}{\partial t} \left(\sum_{\alpha} k_{\alpha} + \Phi + \sum_I \int_{\Omega^{FE}} M_{IJ}^T T_J dV \right) + \sum_I \int_{\Omega^{FE}} \left(\mathbf{V}_I \cdot \frac{\partial}{\partial t} M_{IJ}^V \mathbf{V}_J + \mathbf{V}_I \nabla N_I \sigma \right) dV = 0. \quad (4.36)$$

The total potential is taken to be the potential energy due to interactions of atoms in \mathcal{A} with each other as well as with ghost atoms. Additionally, the FE kinetic and potential energies have been included. Upon application of the time derivative to the MD terms in both constraints, they reduce to

$$g^{V,2} = \sum_{\alpha} \mathbf{f}_{\alpha}^{\lambda} - \sum_{\gamma} \mathbf{f}_{\gamma}^{MD} + \frac{\partial}{\partial t} \sum_I \int_{\Omega^{FE}} M_{IJ}^V \mathbf{V}_J dV = 0 \quad (4.37)$$

$$g^{T,2} = \sum_{\alpha} \mathbf{v}'_{\alpha} \cdot \mathbf{f}_{\alpha}^{\lambda} + \sum_{\alpha} \bar{\mathbf{v}}_{\alpha} \cdot \mathbf{f}_{\alpha}^{\lambda} + \sum_I \int_{\Omega^{FE}} \left(\frac{\partial}{\partial t} M_{IJ}^T T_J dV + \mathbf{V}_I \cdot \frac{\partial}{\partial t} M_{IJ}^V \mathbf{V}_J + \mathbf{V}_I \nabla N_I \sigma \right) dV = 0. \quad (4.38)$$

The total potential of the MD system is included and therefore ghost atoms must be included in the kinetic energy summation. The conservative form of the FE equations implies

$$\sum_I \frac{\partial}{\partial t} \int_{\Omega^{FE}} M_{IJ}^V \mathbf{V}_J dV = \sum_I \int_{\partial\Omega^{FE}} N_I \sigma \cdot \mathbf{n} dS \quad (4.39)$$

$$\sum_I \frac{\partial}{\partial t} \int_{\Omega^{FE}} M_{IJ}^T T_J dV = \sum_I \int_{\partial\Omega^{FE}} N_I \mathbf{q} \cdot \mathbf{n} dS. \quad (4.40)$$

The mean kinetic energy equation is also

$$\sum_I \int_{\Omega^{FE}} \left(\mathbf{V}_I \cdot \frac{\partial}{\partial t} M_{IJ}^V \mathbf{V}_J + \mathbf{V}_I \nabla N_I \boldsymbol{\sigma} \right) dV = \sum_I \int_{\partial\Omega^{FE}} \mathbf{V}_I N_I \boldsymbol{\sigma} \cdot \mathbf{n} dS. \quad (4.41)$$

By re-arranging terms in eq. (4.38), the mean component of the kinetic energy can also be included:

$$g^{T,2} = \sum_{\alpha} \mathbf{v}'_{\alpha} \cdot \mathbf{f}_{\alpha}^{\lambda} + \sum_I \frac{\partial}{\partial t} \int_{\Omega^{FE}} M_{IJ}^T T_J dV + \sum_I \left(\sum_{\alpha} N_{I\alpha} \mathbf{V}_I \cdot \mathbf{f}_{\alpha}^{\lambda} + \int_{\partial\Omega^{FE}} \mathbf{V}_I N_I \boldsymbol{\sigma} \cdot \mathbf{n} dS \right). \quad (4.42)$$

Substituting these expressions back into eqs. (4.37) and (4.38) and applying the locally by FE shape function rather than as a summation, a set of constraints associated with each FE node is derived:

$$g_I^{V,2} = \sum_{\alpha} N_{I\alpha} \mathbf{f}_{\alpha}^{\lambda} - \sum_{\gamma} N_{I\gamma}^* \mathbf{f}_{\gamma}^{MD} + \int_{\partial\Omega^{FE}} N_I \boldsymbol{\sigma} \cdot \mathbf{n} dS = 0 \quad (4.43)$$

$$g_I^{T,2} = \sum_{\alpha} N_{I\alpha} \mathbf{v}'_{\alpha} \cdot \mathbf{f}_{\alpha}^{\lambda} + \int_{\partial\Omega^{FE}} N_I \mathbf{q} \cdot \mathbf{n} dS + \left(\sum_{\alpha} N_{I\alpha} \mathbf{V}_I \cdot \mathbf{f}_{\alpha}^{\lambda} + \int_{\partial\Omega^{FE}} \mathbf{V}_I N_I \boldsymbol{\sigma} \cdot \mathbf{n} dS \right) = 0. \quad (4.44)$$

By taking the inner product of \mathbf{V}_I with eq. (4.43), eq. (4.44) can be reduced to

$$g_I^{T,2} = \sum_{\alpha} N_{I\alpha} \mathbf{v}'_{\alpha} \cdot \mathbf{f}_{\alpha}^{\lambda} + \int_{\partial\Omega^{FE}} N_I \mathbf{q} \cdot \mathbf{n} dS + \sum_{\gamma} N_{I\gamma}^* \mathbf{V}_I \mathbf{f}_{\gamma}^{MD} = 0. \quad (4.45)$$

The modified shape function N_I^* is a partially lumped shape function for localizing restriction of ghost atom quantities is defined as $N_{I\gamma}^* = \beta^{-1} N_{I\gamma}$ such that $\sum_{I \in I^*} N_{I\gamma} = \beta$. The set of nodes I^* are those with both real and ghost atoms in their support.

As both constraint sets involve time derivatives of the restricted atomic momenta and kinetic energy, a general application of Gaussian least-constraints can be applied to the force using an arbitrary target value for the FE data. In this case, the deviation of the atomic forces from the ones from the MD force solver alone. Lagrange multipliers are used to augment this cost function into one that can be minimized subject to the constraints:

$$J = \sum_{\alpha} \frac{1}{2m_{\alpha}} |\mathbf{f}_{\alpha}^* - \mathbf{f}_{\alpha}^{MD}|^2 + \sum_I \lambda_I^V \left(\sum_{\alpha} N_{I\alpha} \mathbf{f}_{\alpha}^{\lambda} + \mathbf{R}_I^V \right) + \sum_I \lambda_I^T \left(\sum_{\alpha} N_{I\alpha} \mathbf{v}'_{\alpha} \mathbf{f}_{\alpha}^{\lambda} + R_I^T \right) \quad (4.46)$$

Setting the variation of J with respect to f_{α}^* to be zero, the equation for the modified force is obtained

$$\mathbf{f}_{\alpha}^* = \mathbf{f}_{\alpha}^{MD} - m_{\alpha} \sum_I \lambda_I^V N_{I\alpha} - m_{\alpha} \sum_I \lambda_I^T N_{I\alpha} \mathbf{v}'_{\alpha}. \quad (4.47)$$

The last two terms are $\mathbf{f}_{\alpha}^{\lambda}$. From eq. (4.47), the alterations to the MD force consist of a uniform acceleration and a drag force proportional to the fluctuating velocity. Note for flux-based constraints the cost function is equivalent to minimizing the magnitude of the coupling force such that the constraints are enforced.

Equation (4.47) also determines the equations for the Lagrange multipliers. The modified force is substituted into each constraint to obtain the following system of equations for λ_I^V and λ_I^T :

$$\sum_{\alpha} N_{I\alpha} m_{\alpha} \sum_J N_{J\alpha} \lambda_I^V + \sum_{\alpha} N_{I\alpha} m_{\alpha} \mathbf{v}'_{\alpha} \sum_J N_{J\alpha} \lambda_J^T = \mathbf{R}_I^V \quad (4.48)$$

$$\sum_{\alpha} N_{I\alpha} m_{\alpha} \mathbf{v}'_{\alpha} \cdot \sum_J N_{J\alpha} \lambda_I^V + \sum_{\alpha} N_{I\alpha} m_{\alpha} |\mathbf{v}'_{\alpha}|^2 \sum_J N_{J\alpha} \lambda_J^T = R_I^T \quad (4.49)$$

The resulting matrix for λ_I has the form

$$\begin{bmatrix} M & C \\ C^T & 2K \end{bmatrix} \begin{bmatrix} \lambda^V \\ \lambda^T \end{bmatrix} = \begin{bmatrix} \mathbf{R}^V \\ R^T \end{bmatrix} \quad (4.50)$$

Being a symmetric matrix, it can be solved iteratively using a conjugate gradient method. However, the coupling matrix C is small in this case. If the Galerkin procedure were used to construct the FE equations without row-sum lumping, it would be zero because it contains the product of the difference between the true and FE velocities and a function represented on the FE basis, and the two would be orthogonal with respect to any function spanned by the FE basis. Use of row-sum lumping for localization implies that C is non-zero, but is still small. Therefore, an iterative solution is preferred. Beginning with the previous value of λ^V , the temperature multiplier is updated, which is then used to update the velocity multiplier. This approach is beneficial as the fractional step update scheme necessitates an iterative solution for λ^T (Chapter 3). Note also that localization of the multipliers to the boundary nodes and use of combinations of fixed-value and flux-based constraints can be performed using the same approaches as for the isolated constraints in previous works ([123], Chapter 3).

4.4 Temporal Integration Scheme

In this section the velocity integration scheme for the atoms and nodal velocity and displacement field is provided when solving problems in the Lagrangian frame. The temperature is always advanced using the fractional step method from Chapter 3, as is the velocity field in Eulerian frame calculations. Following the standard velocity-Verlet algorithm [41], the velocities are first updated:

$$\mathbf{v}_{\alpha}^{n+1/2} = \mathbf{v}_{\alpha}^n + \frac{\Delta t}{2} \frac{\mathbf{f}_{\alpha}^n}{m_{\alpha}} \quad (4.51)$$

$$\mathbf{V}_I^{n+1/2} = \mathbf{V}_I^n + \frac{\Delta t}{2} \dot{\mathbf{V}}_I^n, \quad (4.52)$$

where $\dot{\mathbf{V}}$ is given by eq. (4.14). At this point, both the atomic positions and continuous displacement are updated a full time step:

$$\mathbf{x}_{\alpha}^{n+1} = \mathbf{x}_{\alpha}^n + \Delta t \mathbf{v}_{\alpha}^{n+1/2} \quad (4.53)$$

$$\mathbf{U}_I^{n+1} = \mathbf{U}_I^n + \Delta t \dot{\mathbf{U}}_I^{n+1/2}. \quad (4.54)$$

Given \mathbf{x}_α^{n+1} and \mathbf{D}^{n+1} , both \mathbf{f}_α^{n+1} and $\dot{\mathbf{V}}^{n+1}$ can be determined. Therefore, the atomic and continuous velocities can finish updating according to the last step of the Verlet algorithm:

$$\mathbf{v}_\alpha^{n+1,*} = \mathbf{v}_\alpha^{n+1/2} + \frac{\Delta t}{2} \frac{\mathbf{f}_\alpha^{n+1}}{m_\alpha} \quad (4.55)$$

$$\mathbf{V}_I^{n+1,*} = \mathbf{V}_I^{n+1/2} + \frac{\Delta t}{2} \dot{\mathbf{D}}_I^{n+1}. \quad (4.56)$$

The superscript $(\cdot)^{n+1,*}$ indicates a predicted quantity at time step $n+1$. This is again where a constraint can be applied to the atomic velocities by solving eq. (4.50). As a result, the atomic forces are modified according to eq. (4.47), so the the velocities must be corrected:

$$\mathbf{v}_\alpha^{n+1} = \mathbf{v}_\alpha^{n+1,*} - \frac{\Delta t}{2} \left(\sum_I \lambda_I^V N_{I\alpha} + \sum_I \lambda_I^T N_{I\alpha} \mathbf{v}'_\alpha \right) \quad (4.57)$$

$$\mathbf{V}_I^{n+1} = \mathbf{V}_I^{n+1,*} + \frac{\Delta t}{2} (M_{IJ}^V)^{-1} \left(N_{I\alpha} \sum_J \lambda_J^V N_{J\alpha} + N_{I\alpha} \sum_J \lambda_J^T N_{J\alpha} \mathbf{v}'_\alpha \right). \quad (4.58)$$

4.5 Examples

4.5.1 Couette Flow

Couette flow is a canonical problem in fluid mechanics in which shear flow is generated by means of applying a fixed velocity at a plane a finite distance above a no-slip plane. Here it is used to demonstrate the use of field-based constraints, eq. (4.33) and eq. (4.34), to impose a specified boundary condition. The system considered is $32.43 \times 32.43 \times 64.86$ Å box containing 3564 atoms. Periodic boundary conditions are used in the y and y directions while a layer of artificial atoms above and below the system in the z direction is used to confine the atoms and provide the no-slip condition at the lower boundary. Atoms interact using the Lennard-Jones (LJ) potential energy based on the pairwise distance r^{ij} between atoms i and j ,

$$U^{ij}(r^{ij}) = 4\epsilon \left[\left(\frac{\sigma}{r^{ij}} \right)^{12} - \left(\frac{\sigma}{r^{ij}} \right)^6 \right], \quad (4.59)$$

with an energy of $\epsilon = 0.238$ Kcal/mole and a length scale of $\sigma = 3.405$ Å truncated at 13.5 Å. Each atom's mass is 39.95 g/mole. Interactions between the internal atoms and boundary atoms use $\epsilon = 0.15$ Kcal/mole and $\sigma = 10$ Å. A schematic of the MD system is provided in Figure 4.1. All examples in this paper were run using the LAMMPS MD simulator [106].

To determine a physically realistic initial configuration, each atom is assigned a randomly generated velocity drawn from a Gaussian distribution corresponding to 100 K and run with a Nosé-Hoover [99, 47] thermostat for 1 million time steps of size 5 fs. The rescaling formulation eq. (4.27) is applied every 10 steps over a 2000 step equilibration to maintain this temperature while obtaining a more thermodynamically correct state. Simultaneously, all velocity components at all

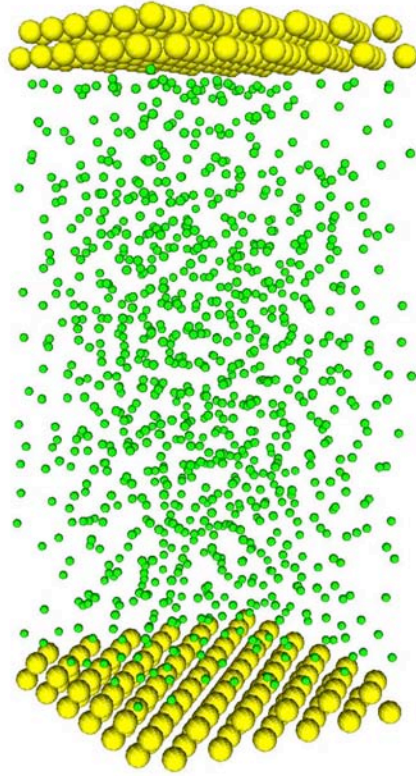


Figure 4.1. Schematic of the Couette flow MD configuration. Surface atoms are yellow while fluid atoms are green.

nodes is fixed at 0 except for the top node, which has the x velocity fixed at $0.1 \text{ \AA}/\text{fs}$. Following equilibration, the rescaling controller are removed from all nodes. The top node is then subject to the field-based constraints to maintain the parallel velocity as previously stated and the temperature at 100 K. The system is then allowed to relax, producing the velocity profile in Figure 4.2 over 1 ns.

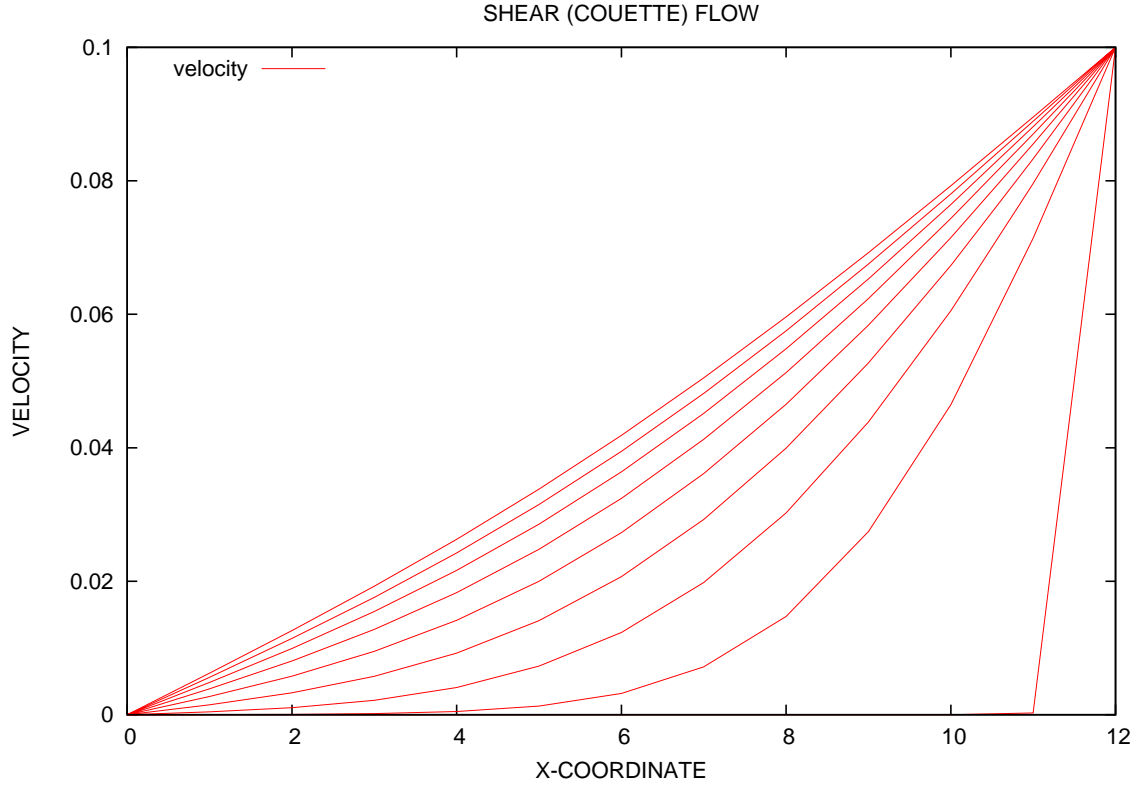


Figure 4.2. Time evolution of Couette flow.

4.5.2 Electro-osmotic Flow

To demonstrate the method using the conservation constraints, eq. (4.43) and eq. (4.45), an ionic solution driven by an electric field is considered. A coarse-grained salt-water model is used based on the model obtained by [77]. The MD domain size is $48.96 \times 48.96 \times 51.69 \text{ \AA}$ while the FE domain extends to 102 \AA in the z direction. A total of 4000 solvent atoms are used in addition to 150 negative and 50 positive ions. They are augmented by an explicitly modeled substrate consisting of 2016 atoms in a three layer deep FCC lattice with spacing 4.08 \AA . Atoms are confined to the MD region by use of a 9/3 LJ wall positioned at the top of the MD domain,

$$U^{iw}(r^{iw}) = \epsilon^w \left[\frac{2}{15} \left(\frac{\sigma^2}{r^{iw}} \right)^9 - \left(\frac{\sigma^2}{r^{iw}} \right)^3 \right] \quad (4.60)$$

using an energy of $\epsilon^w = 0.1351$ eV, a length scale of $\sigma^w = 3.188$ Å, and a 13 Å cut-off radius. Parameters for the inter-atomic LJ self interactions are provided in Table 4.1 with interspecies interactions computed using the Lorentz-Berthelot mixing rules [83, 11]. Electrical interactions were computed using Coulomb’s law within the cut-off radius and the particle-particle/particle-mesh algorithm [46] with a slab geometry correction [134], all of which incorporated a relative dielectric constant of 80. Figure 4.3 illustrates the system setup.

Table 4.1. Self-interaction LJ potentials for all species used in Section 4.5.2.

Atom	mass (g/mol)	ξ_{LJ} (eV)	d_{LJ} (Å)	q (e)
Solvent	18.0154	0.004423	3.188	0
Negative Ion	35.453	0.004336	4.401	+1
Positive Ion	39.0983	0.004336	3.331	-1
Substrate	196.967	0.7244	2.598	0.3472 (first layer)/0 (other layers)

Similarly to the previous section, the atomic velocities are rescaled and shifted using eq. (4.27) to maintain a local temperature of 100 K with no mean velocity, both as measured by the FE mesh. Timestep size, rescaling frequency, and run time are all identical to those used in Section 4.5.1. Following equilibration, flux-based constraints eq. (4.43) and eq. (4.44) are used to couple the MD and FE systems using a localization approximation [123]. An external electric field is also applied in the x direction with magnitude 0.05 V/Å. The velocity profile’s evolution over 50 ps is shown in Figure 4.4.

4.6 Conclusion

This work presents the formulation for combined thermo-mechanical AtC coupling. As opposed to strictly interpreting the atomic velocity as either a center-of-mass velocity or a thermal velocity, it must be decomposed into a mean and a fluctuating component. The FE basis functions are used to generate this decomposition by approximately projecting the atomic velocities onto them. A lumped mass matrix is used which localizes the effects of the atoms to only those nodes whose support they are in, but the result is that the mean and fluctuating velocities are no longer orthogonal with respect to the FE basis.

Due to this lack of orthogonality, previously derived methods for coupling the MD and FE systems cannot be directly applied. Instead, a holistic approach is taken to derive three coupling schemes: direct control of the mean and fluctuating atomic velocities using a modified rescaling thermostat, AtC coupling using the primary variables, and AtC coupling using boundary fluxes. The latter method is readily set up as an iterative problem with error terms in the right-hand sides accounting for “leakage” between the restricted mean and fluctuating velocities due to the approximate nature of the projection. This method is primarily used to set physically reasonable initial

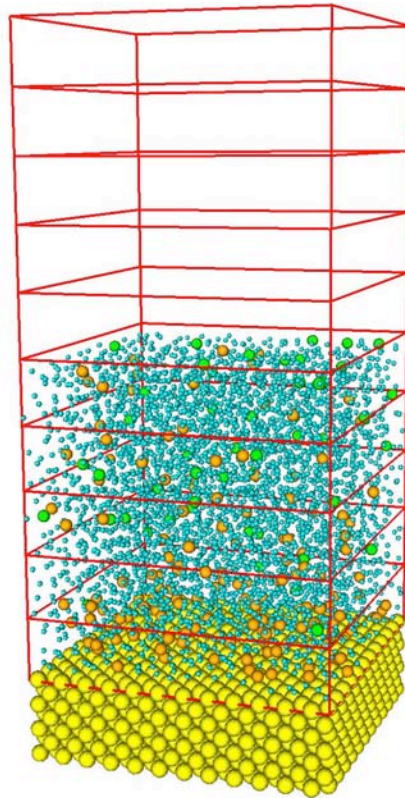


Figure 4.3. Schematic of the electrokinetic flow model configuration. Surface atoms are yellow while fluid atoms are blue, positively charged ions are green, and negatively charged ions are orange. The FE mesh is shown in red.

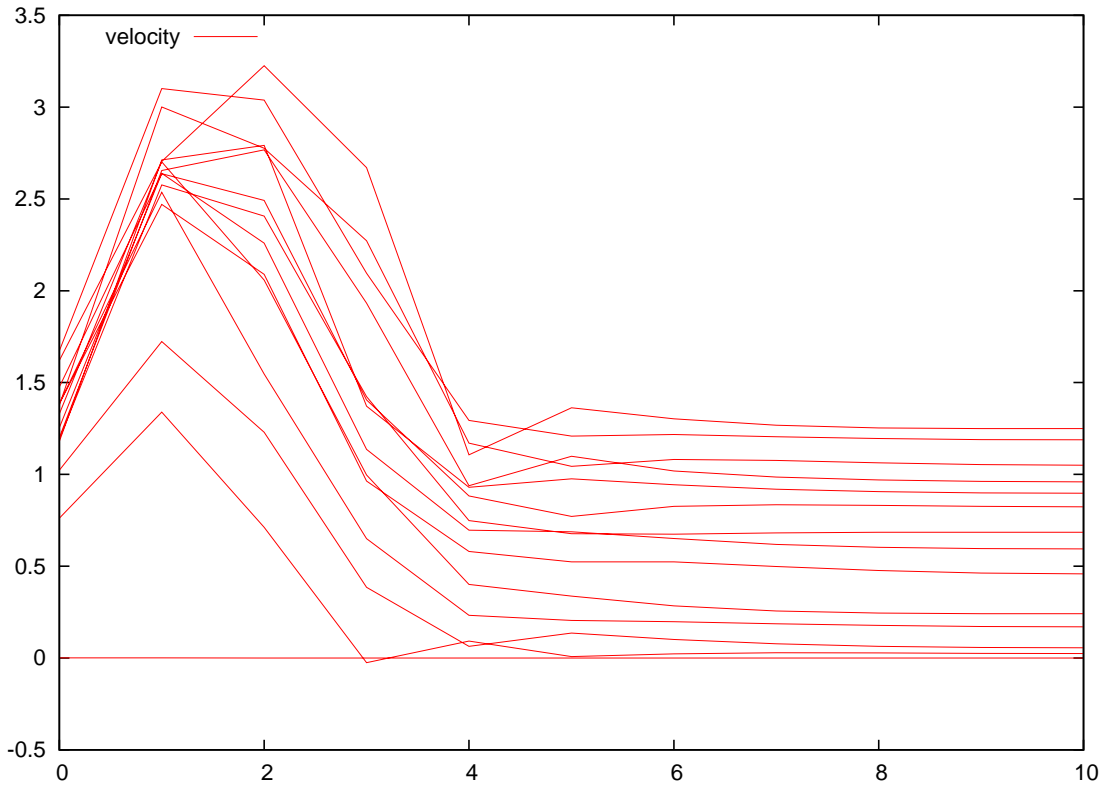


Figure 4.4. Time evolution of the electrokinetic flow.

conditions on the atomistic system such that they spatially vary consistently with the desired FE initial conditions.

AtC coupling algorithms result in symmetric linear systems for a set of Lagrange multipliers which impose constraints to make the FE and MD systems consistent. Because the fractional step update requires a second order solution for the Lagrange multipliers associated with the temperature constraint, an iterative approach is preferred for these equations as well. Again, modification of the right-hand side is necessary. When using flux-based constraints, both momentum and energy are conserved, although part of the energy flux incorporates mean work on the ghost atoms.

This page intentionally left blank.

Chapter 5

Sensitivity to physical parameters in MD simulations of concentration driven ionic flow through a silica nanopore

5.1 Introduction

Synthetic nanopores, which are inspired by their biological counterparts, are widely used in the industry, e.g. in the form of nanoporous membranes applied for desalination or other separation tasks. Of particular interest in these applications is the control of transport through the nanopores, namely by identifying and manipulating some of their properties or modulating key physical processes, see e.g. Refs. [109, 121, 24, 97, 81, 10, 20, 1, 58, 105, 62, 96] and references therein.

Examples include directly manipulating the pore size during the fabrication process such that, based on the target application, only certain molecules or ions can pass through. In this case, nanopores are fabricated with a diameter just slightly larger than the size of the target molecule and such that they can effectively differentiate the flow of (larger) secondary components. Nanoporous membranes of this type are widely used in combination with electrophoretic methods, which involve the transport of solute ions from a source stream into a sink stream, and are applied to water purification or desalination systems.

The selective control of the pore flow can also be achieved by modulating the interactions between the transported ions (or molecules) and the pore walls. In particular, the manipulation of the surface charge on the nanopore walls, see e.g. Refs. [97, 81, 10, 58], has a direct influence on the ionic transport by electrostatic interactions. A nanopore with a negative surface charge distribution favors the permeation of positive ions (cations), while a positive charge distribution favors the flow of negative ions (or anions). The surface charge is also referred to as “gating charge”, due to the fact that its value can cause the nanopore to switch between an open and closed state toward a target ionic species. Such nanopores thus become ion-selective, since the sign of the charge on the pore surface can be chosen to allow the flow of a specific ionic species.

A key factor to leverage in designing optimal membranes is the strong dependence of their per-

The primary authors of this chapter are F. Rizzi, R. Jones, B. Debusschere and O. Knio. It was originally published in [110]. This project supported R. Jones.

meability on the physical processes characterizing nanopore flows. A detailed uncertainty quantification (UQ) analysis of nanopore flows to characterize and describe their complexity can thus be important for improving design capabilities, allowing one to better understand the main physical processes involved in these systems by accounting for the effect of potential uncertainties in the system.

In general, molecular dynamics (MD) simulations of nanopore flows are not new, see e.g. Refs. [22, 124, 125, 4, 28, 29, 100, 79, 84, 51], but the application of UQ to this important system is novel. UQ plays an important role particularly for complex, highly non-linear systems, where even small input uncertainties can be amplified to yield substantial uncertainties in the observations or model predictions [95, 74]. We distinguish between two main sources of uncertainty: parametric uncertainty and intrinsic noise. Parametric uncertainty arises when some model parameters and/or boundary conditions are assumed to be uncertain. Intrinsic noise, on the other hand, is inherently present in MD simulations due to thermal molecular fluctuations. A complete UQ analysis thus needs to properly describe and quantify these two sources of uncertainty. This task becomes particularly challenging for problems where the two sources combine, yielding a complex setting where the model predictions are both *noisy*, due to the effect of thermal fluctuations, and *random*, since they depend on parametric uncertainty. Previous work in this context can be found in Refs. [118, 117] and [111, 112]. In the latter, e.g., the authors focused on analyzing the effect of parametric uncertainty and intrinsic noise in isothermal, isobaric MD simulations of TIP4P water.

In this work, we focus on a system involving a silica nanopore connecting two reservoirs with a binary electrolyte, namely salt (NaCl) water. The heterogeneous nature of the system, due to the several components involved, compounds the inherent complexity of the system. The crystalline silica employed is suitable for the purposes of the present work; however, we envision a future study with an amorphous (glassy) silica model like those obtained by annealing in Refs. [23, 84]. Also, unlike Brownian dynamics simulations such as in Ref. [52], we have chosen to explicitly represent the water solvent in order to model steric effects accurately. In order to create a concentration driven ionic flow through the dense solvent and the silica pore, we developed an efficient, charge-neutral *ad hoc* concentration control algorithm. With this algorithm, concentration gradients of the ions are controlled such that the net flow of the Na^+ ions is opposite to the flow of the negative ions Cl^- . The efficiency of this approach was necessary to make the scope of this study feasible.

The UQ analysis presented in this article is organized into two separate parts, each focusing on a specific aspect. First, we explore the dependence of the pore flow to the pore diameter, and, secondly, we investigate its sensitivity to a gating charge. In this work, we rely on Polynomial Chaos (PC) expansions [132, 37, 74] to represent random variables. To determine the PC coefficients of the stochastic model response, we apply a Bayesian inference approach [38, 118, 111], which allows us to isolate the impact of parametric uncertainty on the noisy, random MD predictions by properly accounting for the effect of MD thermal noise.

The article is organized as follows. In § 5.2, we discuss the atomistic system, the MD setting and the concentration control algorithm. In § 5.3 we illustrate the dependence of the flow on the pore diameter, while 5.4 presents the UQ analysis for the gating charge. Conclusions are presented in § 5.5.

5.2 Atomistic system and MD simulations

In this section we describe the system configuration, the force-field, the concentration control algorithm and other details of the MD computations.

5.2.1 Atomistic system

We constructed a silica pore model connecting two reservoirs of a solution of sodium (Na^+) and chloride (Cl^-) ions in water, as illustrated schematically in Figure 5.1.

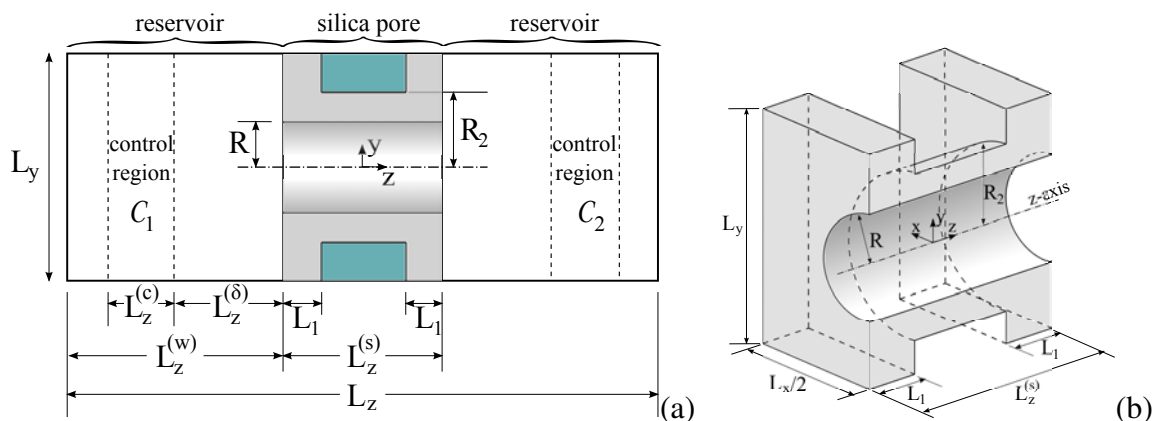


Figure 5.1. (a) Schematic of the dual-reservoir nanopore system. The silica is a rectangular block with a cylindrical pore of nominal radius R . Only few surface layers of the silica block have dynamics (gray), shown in panel (b), while the rest comprises the “frozen” atoms (green). The volume of fluid is nominally $V_f = (2L_xL_yL_z^{(w)} + \pi R^2L_z^{(s)})$.

To build the silica structure, we took the primitive cell of the α -quartz crystal structure from [75], and replicated it $n_x = 11$, $n_y = 14$, and $n_z = 6$ times along x , y , and z respectively, to yield a bulk crystal silica of dimensions (xyz) $L_x \approx 54$, $L_y \approx 60$ and $L_z^{(s)} \approx 32$ Å. Next, we removed silica within a cylindrical region of radius R , such that the resulting pore axis is aligned with the z -axis. The proper stoichiometry is then ensured by adding/removing a few atoms to enforce a ratio of two oxygen atoms per one silicon. The removal procedure leaves some under-coordinated/dangling oxygen and silicon atoms which have to be saturated [23, 84]. To this end, any surface oxygen atom with a dangling bond is saturated with a hydrogen, while any surface silicon atom with one or more dangling bonds is capped with a corresponding number of hydroxyl groups (OH^-), to yield the fully hydroxylated crystal silica model shown in Figure 5.2. Note that the capping of the pore surface defects causes the final silica model to have an effective radius slightly smaller than the nominal value R . The widths of the silica model along the x and y directions, i.e. $L_x \approx 54$ Å and

$L_y \approx 60 \text{ \AA}$, are chosen to be larger than: (a) the maximum pore diameter studied in this work, and (b) the largest cutoff radius used for the potential (defined in § 5.2.2), to prevent the pore feeling the effect of its images [4].

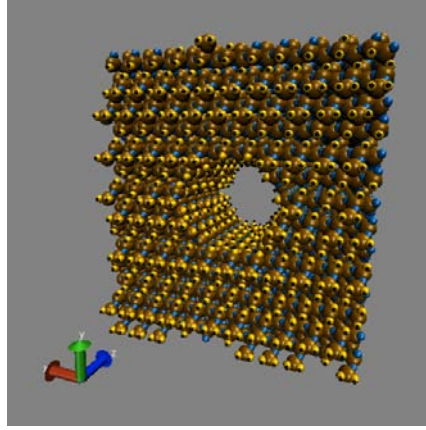


Figure 5.2. Silica pore model of dimensions (x,y,z) $L_x \approx 54$, $L_y \approx 60$ and $L_z^{(s)} \approx 32 \text{ \AA}$ obtained from a bulk crystal silica structure after carving a pore of nominal radius R , ensuring stoichiometry, and hydroxylating the surface and pore defects. Color legend: silicon Si (ochre), bulk oxygens O_{bulk} (blue), hydroxide oxygens O_{hy} (yellow) and hydroxide hydrogens H_{hy} (black).

Next, we constructed the two connected reservoirs each having dimensions $L_x \approx 54$, $L_y \approx 60$ and $L_z^{(w)} \approx 36.75 \text{ \AA}$. The width, $L_z^{(w)}$, of each reservoir should ideally be chosen as large as possible with respect to the pore radius, R . This choice, however, is constrained by the associated computational cost. For the present system, we found $L_z^{(w)} \approx 36.75 \text{ \AA}$ to be a suitable compromise between the two requirements. Indeed, $L_z^{(w)}$ is more than twice the largest radius explored in this study. The two reservoirs and the silica pore were then filled with water molecules such that the total density is of order $\sim 1000 \text{ kg/m}^3$, and, subsequently, a subset of these molecules is randomly chosen and replaced with Na^+ and Cl^- ions to achieve a desired concentration of 1.5 (mol/l). We anticipate that based on the four different pore diameters explored in this work, the water density varies by nearly 1.5%. The resulting system has final length $L_z \approx 105.5 \text{ \AA}$, and is shown schematically in Figure 5.1 (a).

To account for momentum exchange between the aqueous solution and the silica surfaces and to reduce computational expense, only few surface layers of the silica are allowed to have finite-temperature dynamics. To this end, we define two sub-regions of the silica model, one identifying the atoms with dynamics, and one including the “frozen” atoms. The geometry of the sub-region having dynamics is shown in Figure 5.1 (b). The thickness of the surface layer with dynamics is set to 6 \AA , i.e. $L_1 = 6 \text{ \AA}$ and $R_2 = R + 6 \text{ \AA}$.

As alluded to, it is crucial that the two reservoirs of the system must communicate only through

the pore. To effect this, we used hard wall reflectors at the right and left borders of the domain, to contain the fluid. In addition, we minimized the long-range Coulombic interaction of the system with its images along the z axis using the so-called ‘‘slab’’ particle-particle particle-mesh (PPPM) method [46, 134], which employs a vacuum buffer region and a dipole correction. This approach enables us to properly represent the concentration and electric potential gradients, and also the representation of only one pore, as opposed to the two needed in a system that is truly periodic in the flow direction.

The remaining parameters in Figure 5.1 are related to the concentration control algorithm which will be discussed in § 5.2.3 and in the Appendix.

5.2.2 Force-field

The main complexity of the total potential energy Φ is due to the heterogeneous nature of the system, which contains water, silica, and sodium and chloride ions. We represent Φ , with a functional form,

$$\Phi = \Phi_{bonded} + \underbrace{\Phi_{LJ} + \Phi_{Coul}}_{non-bonded}, \quad (5.1)$$

commonly used to describe both pre-defined intra-molecular (*bonded*) interactions and inter-molecular (*non-bonded*) contributions that depend on proximity. Physically, the bonded interactions result from covalent bonds which involve the stretching of pairs of atoms, bending of triplets of atoms, and twisting of quadruplets of atoms. In the present study, all three contributions are modeled with harmonic potentials.

The non-bonded contribution is due to Van der Waals interactions, Φ_{LJ} , and electric forces, $\Phi_{Coulomb}$:

$$\Phi_{LJ} = \sum_{i=1, j>i}^N 4\varepsilon_{ij} \underbrace{\left[\left(\frac{\sigma_{ij}}{r_{ij}} \right)^{12} - \left(\frac{\sigma_{ij}}{r_{ij}} \right)^6 \right]}_{\Phi_{LJ}(r_{ij})}, \quad (5.2)$$

$$\Phi_{Coulomb} = \sum_{i=1, j>i}^N \frac{q_i q_j}{4\pi\varepsilon_0 r_{ij}}, \quad (5.3)$$

where N is the total number of atoms, r_{ij} is the distance between the i -th and j -th atoms, $\{\varepsilon_{ij}, \sigma_{ij}\}$ are the Lennard-Jones (LJ) well depth and reference distance, q_i is the charge of atom i , and ε_0 is the vacuum permittivity. The non-bonded interactions are multiplied by a transition function that acts in the range $r_{ij} \in [r_{c_0}, r_{c_1}]$, as in Ref. [86] and references therein, to ensure a smooth decay to zero between the inner, r_{c_0} , and outer cutoff, r_{c_1} . For the cutoffs, we assume $r_{c_0} = 8 \text{ \AA}$ and $r_{c_1} = 10 \text{ \AA}$, which should be adequate and efficient given that the largest LJ parameter σ is 4.04470 \AA , see Table 5.1. The remaining long-range Coulomb interaction is enacted using the PPPM solver [46].

As commonly done, we define the LJ parameters for the self interactions, and use the Lorentz-Berthelot mixing rules to calculate the cross-species interaction parameters. For the *silica*, the

		ϵ [eV]	σ [Å]	Reference	Charge $ e $	Reference
Water	H _w	0.0	0.0	[56, 88]	0.520	[56, 88]
	O _w	0.006721438	3.15365	[56, 88]	-1.040	[56, 88]
Silica	O _{hy}	0.006595682	3.15380	[82]	-0.51	[82]
	H _{hy}	0.00199475	0.40000	[82]	0.32	[82]
	Si	0.02602000	3.91996	[82]	bond incrementally	[23, 84]
	O _{bulk}	0.006595682	3.15380	[82]	-0.70	[82]
Ions	Na ⁺	0.002033777	2.42990	[104]	+1	[104]
	Cl ⁻	0.006504600	4.04470	[104]	-1	[104]

Table 5.1. Lennard-Jones parameters (ϵ, σ) and Coulombic charge, in multiples of the electron charge $|e|$, for each atom type present in the system: $\{H_w, O_w\}$ are water hydrogen and oxygen atoms, respectively, $\{H_{hy}, O_{hy}\}$ are hydrogen and oxygen atoms appearing in an hydroxide group, O_{bulk} are oxygen atoms in the bulk of the silica, Si are silicon atoms and $\{Na^+, Cl^-\}$ are the salt ions. The Lorentz-Berthelot mixing rules $\sigma_{\alpha\beta} = \frac{1}{2}(\sigma_\alpha + \sigma_\beta)$, and $\epsilon_{\alpha\beta} = \sqrt{\epsilon_\alpha \epsilon_\beta}$ are used to define the interspecies Lennard-Jones interactions. For the remaining set of force-field parameters, refer to Ref. [82] for *silica*, to Ref. [56, 88] for *water* and to Ref. [104] for the *ions*.

potential parameters defining the bonded and LJ interactions are extracted from Lopes *et al.* [82]. All the partial atomic charges of the silica are also obtained from Ref. [82], except for those of the silicon atoms. Some of these atoms are part of the bulk silica while others are bonded to hydroxide groups. To account for these differences in the silica structure, we followed an approach similar to Refs. [23, 84], by assigning the partial atomic charges to the silicons using a bond incremental fashion, see e.g. Refs. [91, 92, 32]. Specifically, the charge of a silicon atom is equal to half the sum of the charges of the atoms that are bonded to it. This method has the following advantages: (a) the charge on each atom takes into account the nature of the other atoms to which it is bonded, and (b) charge conservation is automatically ensured [91, 92, 32]. For *water*, we adopt the TIP4P model [56, 57, 88]. Finally, for the *ions*, which are only subject to non-bonded interactions, all the parameters are obtained from Ref. [104]. Table 5.1 summarizes the LJ parameters and the atomic charges for each atom type.

5.2.3 MD simulations

The MD simulations are performed with LAMMPS [107, 106]. Each simulation consists of an equilibration stage, followed by a data collection stage where the concentration control (CC) algorithm is turned on. All simulations are run at $T = 298.15$ K. The bond lengths and angles for each water molecule are held fixed using the SHAKE algorithm [116], as required by the TIP4P model [56, 57]. In addition, we use a Verlet time integrator [128] with a time step $\Delta t = 1.5$ fs for the equilibration, and $\Delta t = 1.25$ fs for the concentration driven flow.

Equilibration

In the equilibration phase, we use Nosé-Hoover thermostat [98] to control the temperature of the silica pore, and a velocity rescale to enforce the temperature constraint on the water molecules and the ions. Specifically, the temperature rescaling is applied to the water molecules during the full equilibration run, whereas the ion velocities are only rescaled during the first 5×10^5 steps of the total equilibration run of 1.5×10^6 time steps (2.25 ns). We found this approach most efficient in forcing the overall system to equilibrium and the duration of 2.25 ns suitable for all cases considered.

Concentration Control

The equilibrated system is used as an initial condition for the data collection stage of the simulation, where the concentration control (CC) algorithm is applied. During this CC stage, the role of the two control regions \mathcal{C}_1 and \mathcal{C}_2 shown in Figure 5.1(a) is twofold: (a), they are the regions where the ions are inserted or deleted such that the target concentration difference $|\overline{\Delta c}|$ is achieved; (b), they are used to control the temperature and momentum of the atoms that enter these regions (see the Appendix for more details). In other words, during the measurement stage, only the fluid molecules inside the two control regions are subject to temperature and momentum control, while in rest of the system the fluid follows Newtonian dynamics.

To establish a concentration driven ionic flow through the pore, we did not employ the dual-control volume grand-canonical molecular dynamics (GCMD) algorithm typically used [42, 4]. Instead, we developed a more efficient *ad hoc* approach to control the *concentration* (as opposed to the chemical or electrochemical potential) in a charge-neutral manner compatible with the PPPM Poisson solver. The algorithm, described in detail in the Appendix, borrows aspects of GCMD [101, 42, 119] and thermodynamic integration [67, 33], as in Ref. [12]. It is based on the assumption that if the control regions are as far away as feasible, taking into account the long-range Coulomb effects, the proper concentrations and fluctuations occur near the pore entrance and the dynamics represent physically accurate ion flow fields. As shown in Ref. [17], the electric potential and the concentration profiles relax to constant values when the separation between the reservoirs and the pore entrance is on the order of 10-100 Å. For the system under study, the distance from the reservoir, where the charge density is effectively constant, to the pore surface is set to $L_z^{(\delta)} \approx 20$ Å, which is within this range (10-100 Å), and is as large as feasible for a study of this complexity. Furthermore, $L_z^{(\delta)}$ is larger than the maximum value of the pore radius investigated, and twice as large as the cut-off used for the potential describing the interactions. Most importantly, the observed flow rates were insensitive to $L_z^{(\delta)} > 20$ Å in preliminary studies. With reference to Figure 5.1(a), the width, $L_z^{(c)}$, of each control region is set to 10 Å, which was sufficiently large to make the results insensitive also to this parameter.

For a given ionic species Na^+ or Cl^- , we define the corresponding concentration difference

$$\Delta c(t) = c_2(t) - c_1(t) = \frac{N_2(t)}{V_2} - \frac{N_1(t)}{V_1}, \quad (5.4)$$

in terms of the molar concentrations $c_1(t)$ and $c_2(t)$ at time t in two measurement regions \mathcal{M}_1 and \mathcal{M}_2 . Here, N_1 and N_2 are the number of ions in volumes V_1 and V_2 , respectively. As in GCMD, $\Delta c(t)$ is controlled by injecting or removing ions in the two control regions $\mathcal{E}_i \subset \mathcal{M}_i$, $i = 1, 2$, shown in Figure 5.1 (a). In the present study, we employed a target concentration difference $|\overline{\Delta c}| = 60/V_f$ (V_f is the nominal volume of fluid, refer to Figure 5.1a) for each ionic species such that counter flow of oppositely charged ions is effected by opposing chemical gradients. Exchanges of excess ions between the control regions occurred every 100 time steps. The target difference and exchange interval were chosen to facilitate temporarily smooth flow of the ions through the pore, while remaining as close to the linear response regime as possible. Additional parameters and rationale for their values are specified in the Appendix.

The magnitude of the ionic flux $J(t)$ is estimated with the running average

$$J(t) = \frac{1}{tA} N_{exchanges}(t), \quad (5.5)$$

where $N_{exchanges}(t)$ is the (net) number of exchanges (or swaps) of the particular ionic type over the total data collection time t , and A is the cross-sectional area of the pore. We monitored $J(t)$ during the unsteady transient flow, and once steady flow is established, $N_{exchanges}$ is reset to zero. Steady state was determined by the coefficient of variation of the ionic flux based on the previous 500 samples. When it was below 1% for both Na^+ and Cl^- we assumed the transient phase was complete. This transient stage was on the order of 5×10^5 steps, which was followed by 5×10^6 steps where the time averaged ionic fluxes and associated spatially resolved average flow data were collected. Given that $|\Delta c_{\text{Na}^+}| = |\Delta c_{\text{Cl}^-}|$, we defined an effective pore conductance

$$G(t) = \frac{J(t)}{|\Delta c|}. \quad (5.6)$$

for each ionic species .

5.3 Dependence on the pore diameter

In this section we quantify the relationship between the nanopore flow and the nominal pore diameter, $D = 2R$, by considering four values $D = 12.5, 17, 21$ and 27 \AA . The four values of D yield

Note that we validated this method against a steady flux measured via integration of the velocity profiles of the ions over the cross-section of the pore, but for brevity the comparison is omitted from the present discussion.

Here, for example, $G_{\text{Na}^+} = G_{++} + G_{+-}$, with G_{++} being the contribution to the Na^+ conductance due to a gradient in c_{Na^+} only, while G_{+-} is the contribution to the Na^+ conductance due to a gradient in c_{Cl^-} . Given that the flux, J , is measured relative to the pore area, G is primarily a property of the *pore*, not of the membrane, since increasing the area of the membrane, while keeping the pore density in the membrane fixed, is expected to result in only small changes in G . Given the limits on computational resources, the additional studies for $(\Delta c_{\text{Na}^+} > 0, \Delta c_{\text{Cl}^-} = 0)$, and $(\Delta c_{\text{Na}^+} = 0, \Delta c_{\text{Cl}^-} > 0)$, needed to estimate the other contributions, i.e. G_{++} , G_{--} , are left for future work.

Recall that the nominal value, D , identifies the pore size at the stage before the pore defects are saturated with hydroxide groups. During the MD simulation, the effective pore diameter, D_{eff} , is equal, on average, to $D_{\text{eff}} = D - 2(r_0^{O_{\text{hy}}+H_{\text{hy}}})$, where $r_0^{O_{\text{hy}}+H_{\text{hy}}}$ is the equilibrium length of a hydroxide group. Considering that D_{eff} changes during the

four systems with total number of atoms, N , ranging from $N = 32124$ for $D = 12.5 \text{ \AA}$, to 31630 for $D = 27 \text{ \AA}$, and are shown in Figure 5.3. The smallest D was chosen as the smallest practical diameter that, for the present system, yields a measurable non-zero ionic flux through the pore. The largest D was chosen such that the effects of the periodic images of the system along x and y remain small. To account for the effect of the intrinsic (thermal) noise, for each value of D five replica simulations are run, each of which used different initial velocities and a different random seed for the stochastic insertion/deletion aspect of the CC.

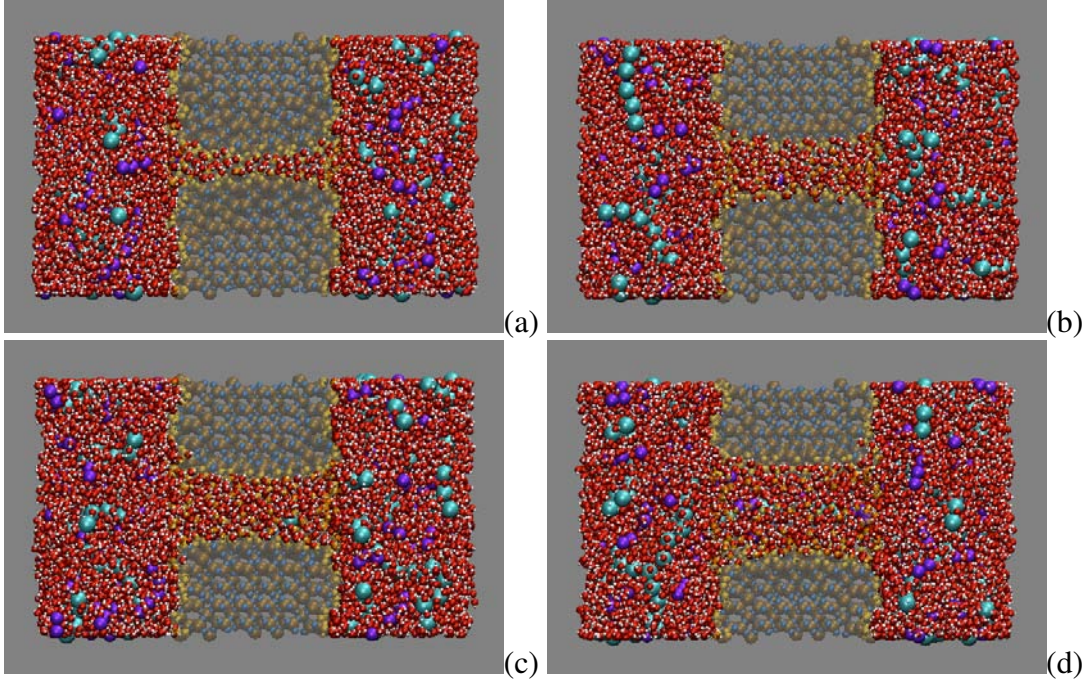


Figure 5.3. Snapshots of cross-sectional views of the systems for $D = 12.5$ (a), 17 (b), 21 (c) and 27 \AA (d), taken during the steady state of the CC stage. Color legend: Si (ochre), O_{bulk} (blue), O_{hy} (yellow), H_{hy} (black), O_w (red), H_w (white), Na^+ (purple), Cl^- (cyan). The silica is nearly transparent for visualization convenience.

5.3.1 Velocity profiles

In this section, we examine the radial and axial profiles of the axial velocity, v_z , of the fluid, i.e. water and ions. These profiles are extracted using standard binning techniques and these coarse-grained values are subsequently time-averaged using a window of 100 time steps to produce a time series.

simulation due to thermal effects and depends on the hydroxide bonds equilibrium distances, the effective diameter, D_{eff} , is a well-defined quantity only as a thermal average. Hence, in the results section, we will always refer to the nominal diameter, D , since it is known upon construction.

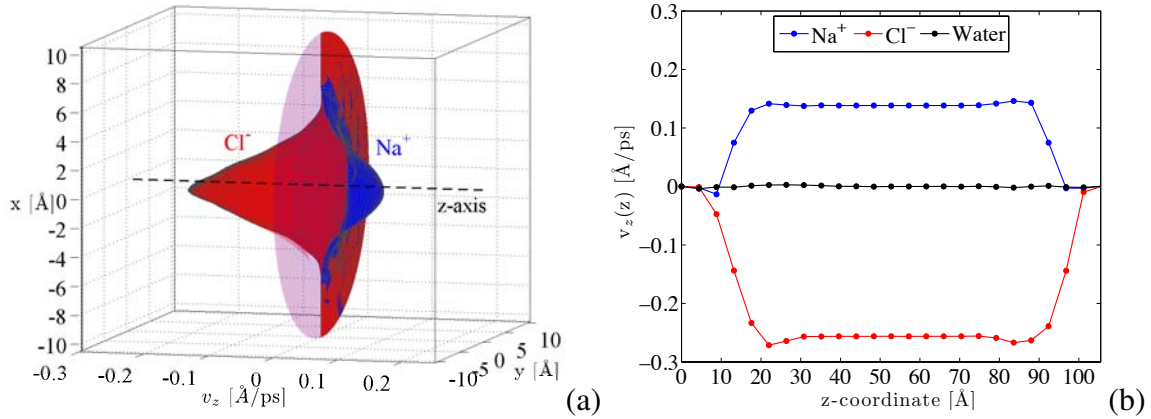


Figure 5.4. (a) Time/bin-averaged radial profile of the axial velocity v_z , for Na^+ and Cl^- computed for one replica of the case $D = 21 \text{ \AA}$ during the steady phase of the CC stage. (b) Time/bin-averaged axial velocity v_z plotted as a function of the z -coordinate computed for one replica of $D = 21 \text{ \AA}$ at the final step of the CC stage for water, Na^+ and Cl^- . In (a), for the sake of visualization, the data obtained from the spatial binning are interpolated over a finer mesh. In (b) the filled circles are plotted at the location of the 24 bins.

To construct the radial profile, we discretize the pore volume with thin, long 3D boxes of square cross-sectional area equal to 1.5^2 \AA^2 , thus resembling a “tessellation” method. Figure 5.4 (a) shows the result of the radial dependence of the axial velocity v_z computed for Na^+ and Cl^- from one replica of the case $D = 21 \text{ \AA}$. The circular section displayed in the plot corresponds to the nominal pore cross-section. Clearly, the profiles obtained for both Na^+ and Cl^- peak near the pore axis, and decay to zero in the region closer to the pore walls. Although both profiles display nearly radial symmetry, the Na^+ profile is parabolic-like, whereas the Cl^- profile displays a more cone-like form. This difference suggests that the Na^+ ions tend to flow across the full pore cross-section, whereas the Cl^- tend to be more concentrated near the pore centerline (probably due to their larger size), thus yielding a more peaked profile. Note that v_z decays to zero before the walls, due to the fact that cross-section plotted in Figure 5.4 (a) corresponds to the nominal diameter, D , while the effective pore diameter during the MD, as anticipated before, is smaller due to the presence of the hydroxide groups saturating the pore surface. A key observation is that the area under the v_z -profile of Cl^- is larger than that of Na^+ , thus indicating that the Cl^- flux is larger than that of the sodium. The physical explanation behind this result is addressed in more detail in § 5.3.2.

For the second quantity of interest, i.e. the z -dependence of the axial velocity, we discretize the domain with 24 slabs orthogonal to the z -axis that span the full domain length along x and y , and each slab has width, L_{bin} , along z equal to $L_{bin} = L_z/24 \approx 4.4 \text{ \AA}$. Figure 5.4 (b) shows the time/bin-averaged axial velocity for water, Na^+ and Cl^- as a function of the z -coordinate, obtained using the data from one replica of $D = 21 \text{ \AA}$. The profiles of both ions are nearly zero in two narrow

regions near the upper and lower domain boundaries, followed by an upward trend in the regions of the reservoirs close to the pore entrances and finally settle into a constant trend that extends along the entire pore length. This result indicates that the ions are essentially quiescent in the reservoirs, then undergo a gradual change in velocity as they move toward to pore, and, finally, they maintain a constant velocity in the pore. When the ions approach the pore, there is a weak deceleration, which can be explained as follows. While some ions enter the pore in a neighborhood of its central axis, other approach the pore from regions closer to the silica atoms, thus interacting with the latter more strongly. This effect causes these ions to decelerate while approaching the pore. Hence, since each velocity data point is obtained by averaging the contribution of all ions inside each slab, the decelerating ions tend to lower the global slab-averaged velocity. The plot also reveals an evident symmetry about the pore vertical mid-plane, thus indicating that the same dynamics and physical processes occur on both sides of the pore and that the transport is in a linear regime. The ion profiles also indicate that the Cl^- -flux is larger than that for Na^+ , confirming the same observation extracted from panel (a). Finally, Figure 5.4 (b) shows a nearly zero axial velocity $v_z(z)$ for water, suggesting that at steady state the water molecules are on average stationary. Similar results are obtained for the other three diameter values, but are omitted for brevity.

5.3.2 Ionic conductance

The top row of Figure 5.5 shows the time evolution of the running average of the conductance, $G(t)$, computed for (a) Na^+ and (b) Cl^- , obtained for all 5 replicas at each diameter value. In all cases, $G(t)$ becomes essentially constant, as is characteristic of a steady state. Figure 5.5 shows that the pore diameter, D , has two main effects on the $G(t)$. First, as the diameter D increases, the estimated value of the conductance G substantially increases. Second, D only weakly affects the needed sampling time in the running average such that a longer duration is needed to obtain a steady value for smaller D , where fewer ions are passing through the pore.

Figure 5.6 (a) shows the steady-state value of G obtained for Na^+ and Cl^- plotted as a function of the nominal pore diameter, D , for all 5 replicas. Clearly, for both ions, the conductance increases as a function of D , but a distinct difference is observed in the slope of the trend, which is sharper for the (effective) Cl^- conductance, G_{Cl^-} . Figure 5.6 (b) shows that the coefficient of variation, σ/μ , monotonically decreases as the pore diameter, D , increases from 12.5 Å to 27 Å. In fact, the value of σ/μ computed for Cl^- is larger than the one obtained for Na^+ for $D = 12.5, 17$ and 21 Å, while the trend reverses for $D = 27$ Å. For both ions, the observed trend of σ/μ suggests that the variance in the replicas remains approximately constant as D varies and, also, on average, the variance computed for G_{Na^+} is smaller than that for G_{Cl^-} .

The mean trends shown in Figure 5.6 (a) allow us to make a key physical observation. They indicate that for $D \geq 17$ Å, the average Cl^- conductance is substantially larger than that for Na^+ , the values are comparable for $D = 12.5$ Å. This is the result of an interplay between size (steric) effects and ionic mobility. For $D = 12.5$ Å, the cross-section of the pore limits the number of water molecules that can enter it, see Figure 5.7 (a), and, thus, the water molecules tend to arrange in a chain-like structure [136]. As a consequence, since these water molecules cannot effectively surround the ions inside the pore, they cannot form a complete solvation shell, and, thus, the ions

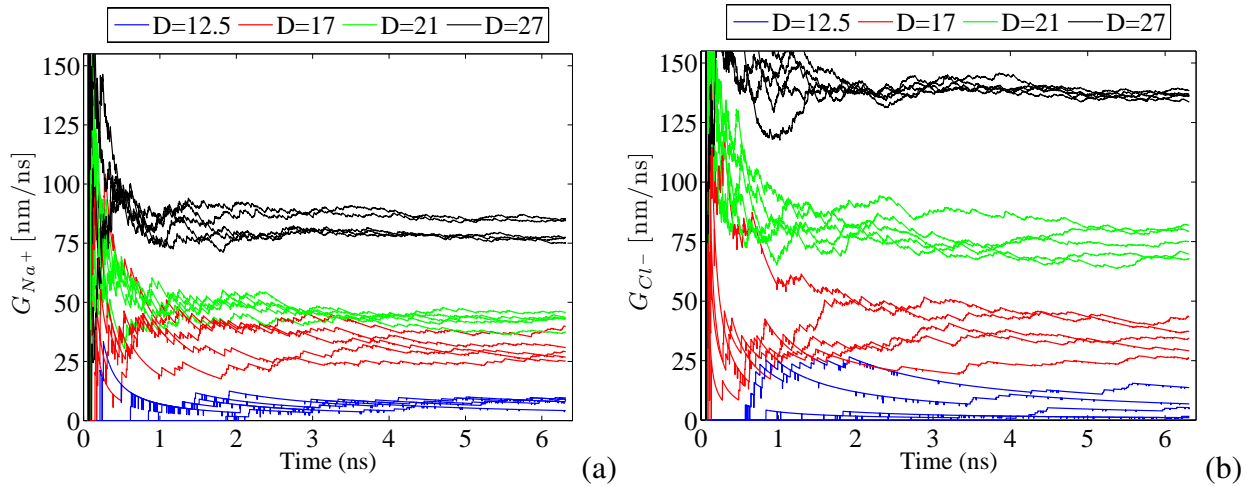


Figure 5.5. Time evolution of the running average conductance, $G(t)$, for Na^+ (a) and Cl^- (b) plotted for all 5 replicas and each diameter value showing the variation in steady state values and the timescale at which steady values are achieved.

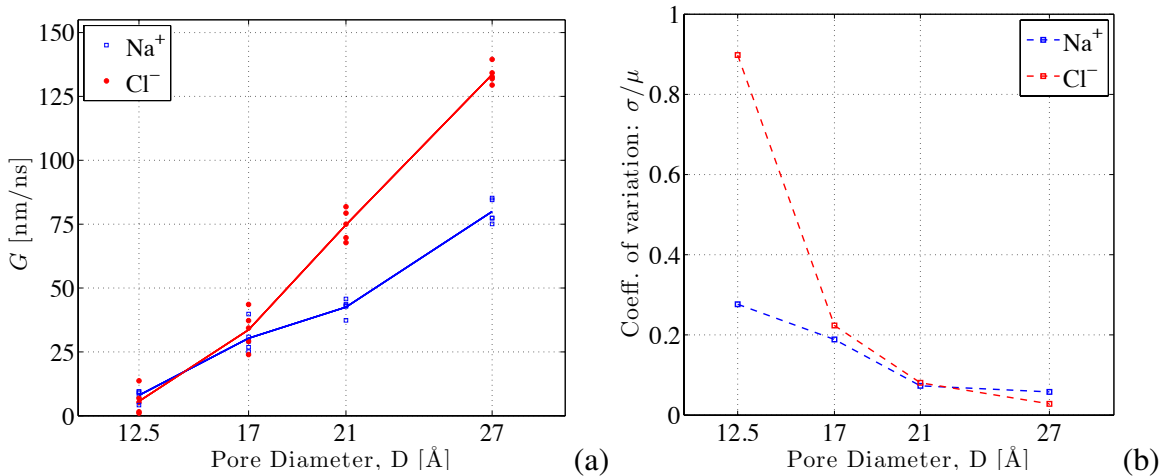


Figure 5.6. (a) Steady-state replica values (markers) of the Na^+ (blue) and Cl^- (red) conductance as a function of the nominal pore diameter D , with the superimposed lines outlining the replica-averaged values. (b) Coefficient of variation, σ/μ , i.e. the ratio of the standard deviation, σ , over the mean, μ , of the conductance data plotted as function of the pore diameter, D , for both ions.

are strongly affected by the pore walls. This confinement effect favors the flow of the ions with smaller size, i.e. Na^+ . Similar physical processes have been studied in Refs. [8, 85, 135, 44, 84]. In contrast, when the diameter D becomes sufficiently large, i.e. $D \geq 17$ Å, the water molecules

inside the pore can effectively create a complete solvation shell around the ions, as shown by Figures 5.7 (b,c,d). Therefore, the dynamics of the ions is dominated by their mobility. In this case, the resulting flux of Cl^- is greater than Na^+ , because the diffusivity of Cl^- is larger than that of Na^+ as reported, e.g., in Refs. [115, 78, 25, 70, 19, 27].

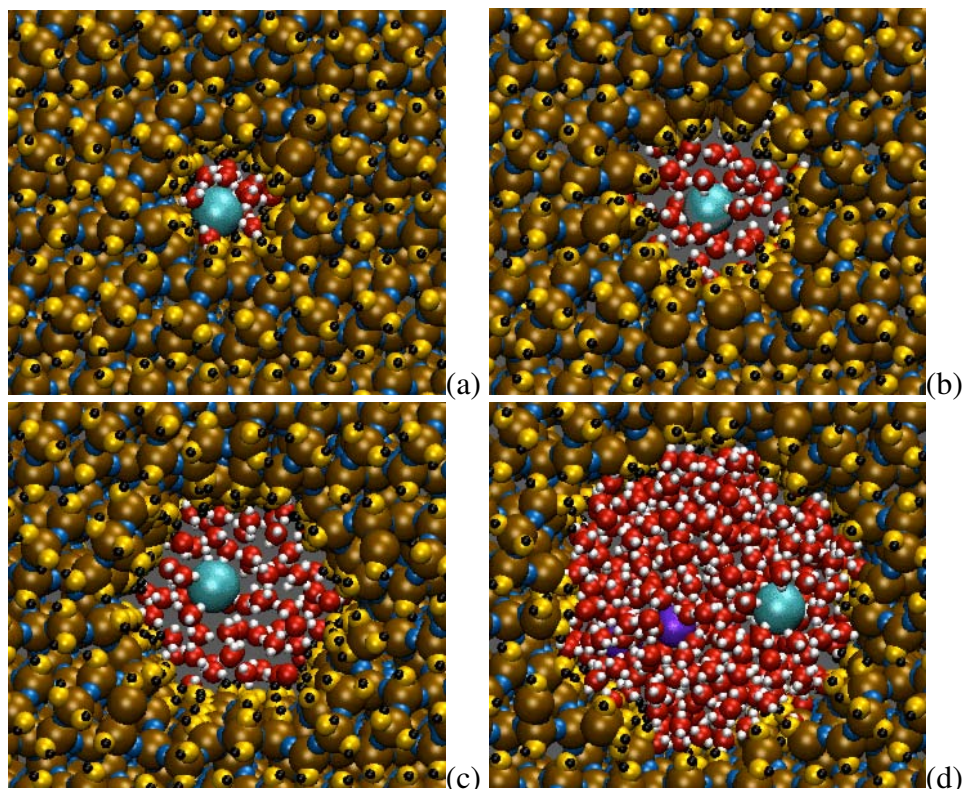


Figure 5.7. Snapshots obtained for $D = 12.5$ (a), 17 (b), 21 (c) and 27 \AA (d), during the steady state of the CC stage, showing the distribution of water molecules around the ions passing through the pore: Na^+ is color-coded purple, while Cl^- is color-coded cyan.

5.4 Sensitivity to the gating charge

This section explores how the silica system under study responds to a “gating charge,” for a fixed pore diameter, $D = 21 \text{ \AA}$.

We denote with q_{surf} the target *charge density* that is added to the inner pore surface to effect a gating charge. Since the actual charges are likely fluctuating and in the present case unknown, a modeling assumption is needed to determine how the charge is distributed on the exposed pore atoms. We assume that the distribution is uniform to mimic the addition of a uniform layer of functionalized/charged groups on the surface of the pore.

For a target value of the gating charge density, q_{surf} , we calculate the total charge, Q_g , to be added as

$$Q_g = q_{surf} \pi D L_z^{(s)}, \quad (5.7)$$

where $L_z^{(s)} = 32 \text{ \AA}$ is the pore length along the z -axis. Next, given the $N_{hy} = 162$ hydroxide groups on the pore surface, we calculate the local charge, q_{hy} , to add to the charge of each group given by the force-field parameterization in §5.2.2 as

$$q_{hy} = \frac{Q_g}{N_{hy}}, \quad (5.8)$$

and equally split q_{hy} between the oxygen, O_{hy} , and hydrogen, H_{hy} , of each OH-group.

Note that this procedure yields a system with an excess charge which must be compensated for to have a neutral system. The approach we adopted consists of adding to the salt-water solution a suitable number of positive, Na^+ , or negative, Cl^- , ions to regain zero total charge. This approach is motivated by the fact that the remainder of the molecules forming the pore surface functionalized groups (which we do not model explicitly) typically remain in solution. A further constraint is that for a given value of q_{surf} the resulting total charge, Q_g , must be compensated by an *integer* number of Na^+ or Cl^- ions. Consequently, this poses a limitation on the values of q_{surf} that can be explored.

Also, due to the fact that the gating charge is compensated by adding ions to the solution, the final concentration of Na^+ and Cl^- varies according to the target value of q_{surf} . Since the goal is to assess the effect of the gating charge only, with all the other components effectively constant, we apply another correction. For a given value of q_{surf} , we calculate *a priori* the number of ions needed to compensate this gating charge, and we slightly change the original base concentration (1.5 mol/l) such that the *total* final number of ions, i.e. after compensating for the gating charge, remains constant for all systems considered. Of course, according to the sign of q_{surf} , one of the two ionic species Na^+ or Cl^- will be in excess with respect to the other, but the overall differences are small. For instance, the maximum charge studied here is compensated with 35 ions, whereas the base concentration gives about 444 ions.

5.4.1 UQ Formulation

The goal is to explore the sensitivity of the ionic conductance on different charge distributions. In this present case, this can be effectively achieved by applying a *forward propagation* of uncertainty, where the charge density, q_{surf} , is assumed to be an uncertain parameter, and its uncertainty is propagated and mapped to a response surface for the observables of interest. We parametrize the uncertainty according to

$$q_{surf} = 0.3 \xi, \quad [\text{Coul/m}^2], \quad (5.9)$$

Alternately, an equal and opposite charge could be introduced inside the core of the bulk silica. This method, however, would create undesired asymmetries and inhomogeneities in the system.

where ξ is a standard uniform random variable, i.e. $\xi \sim \mathcal{U}(-1, 1)$, allowing us to explore a range of variation between -0.3 and 0.3 Coul/m², which has been chosen slightly larger than the one studied in Ref. [26].

The stochastic reformulation in equation (5.9) implies that the observables extracted from the MD simulations of the nanopore flow are considered as random variables. If it has finite variance, any quantity of interest (QoI) can be expressed with a polynomial chaos expansion (PCe) based on Legendre basis [74]. The PCe of a generic QoI, X , extracted from the present MD system can be expressed as

$$X = \sum_{k=0}^{\infty} c_k \Psi_k(\xi), \quad (5.10)$$

where $\{c_k\}_{k=0}^{\infty}$ is the set of PC coefficients, and Ψ_k are Legendre basis functions. Note that for the present 1D case, the basis functions coincide with the Legendre polynomials. Equation (5.10) allows us to build a direct relationship between the uncertain input, q_{surf} , and a target observable, and, thus, it represents a mapping of the uncertainty from the parameter to the observables. Note that a similar formalism could also have been applied to the sensitivity of the system to the pore diameter, but since the pore diameter is a discrete quantity, the associated UQ analysis would need the use of discrete UQ methods. For brevity, however, this UQ analysis was omitted and is limited to the gating charge only.

5.4.2 Bayesian regression

To determine the PC coefficients, we rely on a Bayesian regression approach [38, 118] that naturally accommodates noisy MD data [111, 112]. In this approach, the PC expansion represents the regression function [38, 118, 111, 112]. Its implementation consists of three main steps: (a) collecting a set of the observations $\{\xi_i, G_i\}$ of the Na⁺ and Cl⁻ conductance by suitably sampling the ξ variable, (b) formulating the Bayesian model and, finally, (c) sampling the target posterior distribution.

Collection of observations

We sample the ξ -support with five points $\{\xi_i\}_{i=1}^{n=5}$, corresponding to gating charge values $q_{surf} \approx -0.265619083, -0.144193217, 0.0, 0.144193217, 0.265619083$ Coul/m², and at each of these points we create the corresponding MD system. Note that this choice is not unique, because a regression approach does not pose specific constraints on the sampling procedure. However, for the present case, these points have been chosen because each one of them yields a system satisfying all the constraints defined previously, and because we are partially limited by the large computational cost of the system. The stochastic reformulation in equation (5.9) implies that when $q_{surf} = 0.0$ Coul/m², the corresponding system coincides with the one studied in § 5.3 for $D = 21$ Å.

To account for the effect of the intrinsic noise, at each grid point $\{\xi_i\}_{i=1}^{n=5}$, we generate $m = 3$

replicas of the corresponding MD system, by using 3 different sets of random numbers to initialize the velocity field of the atoms and the CC algorithm. This set of 5×3 MD simulations, yields the following set of observations

$$\mathbf{G} = \{G_{i,j}\}_{i=1,\dots,5}^{j=1,\dots,3}, \quad (5.11)$$

where G denotes the steady-state value of the conductance computed for Na^+ or Cl^- , the index i enumerates the 5 grid points along ξ , j enumerates the 3 replicas, and, consequently, $G_{i,j}$ denotes the j -th replica value obtained at the i -th sampling point ξ_i . Figure 5.8 (a) shows the conductance data obtained for Na^+ (blue) and Cl^- (red) plotted as a function of the gating charge density q_{surf} . The corresponding variances are plotted in Figure 5.8 (b). Note that the gating charge $q_{surf} = 0.265619083 \text{ Coul/m}^2$ yields the three replicas of the Na^+ conductance to be exactly zero and, thus, the corresponding variance is not shown Figure 5.8 (b), due to the logarithmic scale in the y-axis. This result is likely due to finite sampling, namely the fact that for a limited simulation time and a limited number of replicas the observation of an ion transit through the pore may not be observed. However, based on statistical mechanics, even at $q_{surf} \sim 0.27 \text{ Coul/m}^2$ we expect a non-zero probability for the Na^+ to pass through the pore.

Figure 5.8 (a) shows that the pore can be made effectively anion or cation selective by properly tuning the value and sign of q_{surf} . Specifically, the pore becomes essentially completely gated toward Na^+ when $q_{surf} > 0.2 \text{ Coul/m}^2$, while becoming gated toward Cl^- for $q_{surf} < -0.28 \text{ Coul/m}^2$. The results also reveal that for both ions, the variance increases with the in-

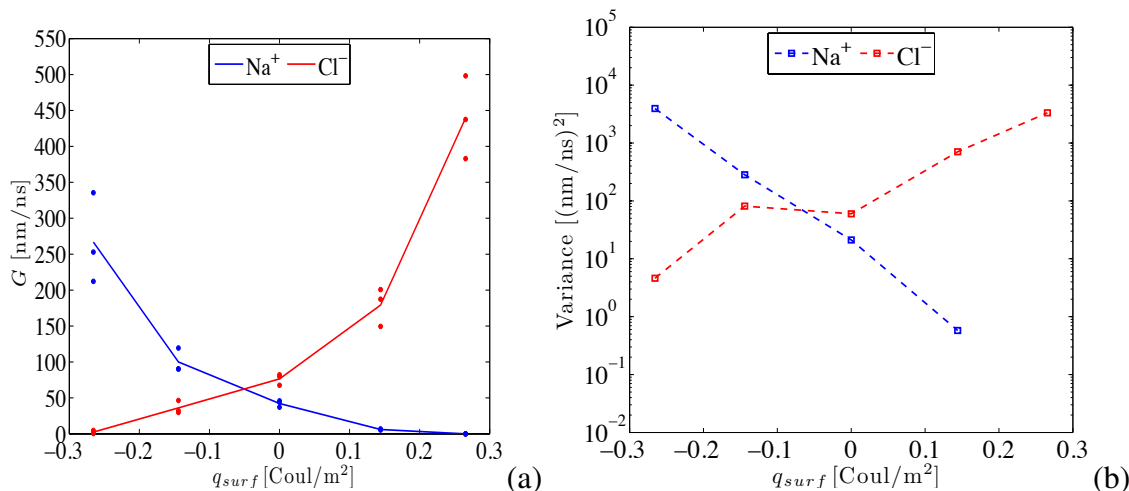


Figure 5.8. Panel (a): data set of the ionic conductance, G , computed for all replicas as a function of the gating charge density q_{surf} for Na^+ and Cl^- . The superimposed solid lines connect the replica-averaged values. Panel (b) shows the corresponding variances plotted as function of q_{surf} with a logarithmic scale on the y-axis. Note that since $q_{surf} = 0.265619083 \text{ Coul/m}^2$ yields vanishing Na^+ conductance for all three replicas, the corresponding variance is not shown panel (b).

creasing conductance, see Figure 5.8 (b). This can be explained by examining the situation in the limit of a completely gated pore. In this case, since the flux would be exactly zero for any given replica, the variance would be zero as well, as occurs for the Na^+ at $q_{surf} = 0.265619083 \text{ Coul/m}^2$. We thus expect the variance to decrease as the conductance (flux) decreases. Figure 5.8 (b) shows that the variances obtained for both ions approximately follow a linear behavior with respect to the charge density, q_{surf} , when plotted with a logarithmic scale for the y-axis. This observation will play a key role in defining the noise model of the Bayesian regression.

Finally, the results show that for a given q_{surf} , the associated Cl^- conductance is larger than the Na^+ conductance obtained at the same charge magnitude. This is due to the fact that for the current pore size, $D = 21 \text{ \AA}$, the ion's mobility dominates the size (steric) effects, and, thus, the larger mobility of Cl^- yields a larger flux. Overall, the gating effect observed in the conductance is relatively symmetric with a cross-over point at $\approx -0.05 \text{ Coul/m}^2$. The present results are in good agreement with those in Ref. [26].

Note that one could reduce *a priori* the variance in the MD predictions of a target observable by using a longer simulation time and/or larger number of atoms. This approach, however, is constrained by the large computational cost associated with the present MD system. The Bayesian approach thus provides the suitable framework to properly account for inherent noise, without the need to act on the system *a priori*.

Noise model and likelihood function

The regression analysis aims at representing, for each ion, the conductance data, \mathbf{G} , with respect to changes in the gating charge using a truncated PC expansion model

$$M(\xi) \doteq \sum_{k=0}^P g_k \Psi_k(\xi), \quad (5.12)$$

where $\{g_k\}_{k=0}^P$ are the set of PC coefficients, Ψ_k are the Legendre basis functions, and $P + 1$ is the dimension of the basis. Note that in the present 1D setting, P coincides with p , the highest order of all polynomials retained in the truncated basis.

The problem thus translates into using Bayesian inference to obtain the PC coefficients $\{g_k\}_{k=0}^P$ appearing in the above representation, given a data-set, \mathbf{G} , of the form in equation (5.11). To formulate the likelihood, we assume an additive error model according to

$$G_\ell = M(\xi_\ell) + \gamma_\ell, \quad \ell = 1, \dots, 15, \quad (5.13)$$

where the index ℓ enumerates the 15 available data points for Na^+ or Cl^- shown in Figure 5.8 (a), ξ_ℓ denotes the coordinate of the ℓ -th observation G_ℓ , and γ_ℓ is random variable capturing the discrepancy between the data point, G_ℓ , and the corresponding model prediction, $M(\xi_\ell)$. Again, G generically denotes the conductance of one of the ions, Na^+ or Cl^- .

An important step concerns the choice of the distribution of the random variables $\{\gamma_\ell\}_{\ell=1}^{15}$. Due to the fact that each data point, G_ℓ , is extracted from a running average in *independent* but statistically equivalent MD simulations, based on central limit arguments we expect that as the number

of atoms in the system and the number of time-averaged samples become large, the distribution of the target observable, G , around the true mean tends to a Gaussian. Based on the previous arguments, we assume $\{\gamma_\ell\}_{\ell=1}^{15}$ to be *independent* and *normally* distributed with mean zero. To model the variances, σ_ℓ^2 , of each random variable, γ_ℓ , we assume a ξ -dependent noise model, namely $\sigma_\ell^2 \equiv \sigma^2(\xi)$. This choice stems from the results shown in Figure 5.8, which reveal that the variance of the data varies approximately linearly with ξ in a semi-log plot. Hence, we translate this observation in mathematical form by parametrizing the *natural logarithm* of the variance, $\ln(\sigma^2)$, with a *linear* PC representation according to

$$\ln(\sigma^2) = d_0 + d_1 \xi. \quad (5.14)$$

Higher-order polynomials could be used, but we tested that, for the present case, they would not yield significant improvement in the final representation of the main target observable, i.e. the pore conductance. Hence, in the present work, we argue that a linear approximation is a good compromise between adequacy and simplicity. In the present work, we treat the coefficients $\{d_0, d_1\}$ as hyperparameters, i.e. they are become part of the set of unknowns. A key assumption, reflected by the lack of a model discrepancy term in equation (5.13), is that, for a given observable, the regression function, $M(\xi)$, properly captures the corresponding data set, \mathbf{G} . This hypothesis can be verified *a posteriori* by comparing the inferred trend of σ^2 with its estimate based on the data. For a given order, p , of the PC regression function, $M(\xi)$, if the inferred trend and magnitude of $\sigma^2(\xi)$ is in good agreement with its data-based estimate shown in Figure 5.8 (b), then this suggests that the model representation is appropriate. On the contrary, if they are significantly different, the regression function must be refined. An alternative but more delicate approach would be to set *a priori* the model noise variance equal to its data-based estimate. In this case, a model discrepancy term would be necessary to check the “goodness” of the chosen model.

The previous discussion yields the following likelihood function

$$\begin{aligned} \mathcal{L} &\doteq \mathcal{L} \left(\{g_k\}_{k=0}^P, \{d_0, d_1\} ; \mathbf{G} \right) \\ &= \prod_{i=1}^5 \prod_{j=1}^3 \frac{1}{\sqrt{2\pi[\sigma(\xi_i)]^2}} \exp \left(-\frac{[G_{i,j} - M(\xi_i)]^2}{2[\sigma(\xi_i)]^2} \right). \end{aligned} \quad (5.15)$$

Bayes’ theorem yields the target joint posterior distribution

$$\pi \left(\{g_k\}_{k=0}^P, \{d_0, d_1\} \mid \mathbf{G} \right) \propto \mathcal{L} \left(\{g_k\}_{k=0}^P, \{d_0, d_1\} ; \mathbf{G} \right) \prod_{k=0}^1 \hat{q}_k(d_k) \prod_{k=0}^P q_k(g_k), \quad (5.16)$$

where $\hat{q}_k(d_k)$ and $q_k(g_k)$ denote the presumed independent priors of the k -th PC coefficient, d_k , of the noise variance and the k -th PC coefficient, g_k , of the regression function, respectively. For $q_k(g_k)$, $k = 0, \dots, P$, we assume uniform priors with the additional constraint that for any given sample set $\mathbf{g} = \{g_0, \dots, g_P\}$, the corresponding model prediction, $M(\xi)$, must be non-negative over the entire axis ξ . This is a key physical constraint, because we are modeling the *magnitude* of the conductance, which must be non-negative, and the prior should suitably account for this constraint. For the priors $\hat{q}_k(d_k)$, $k = 0, 1$, the following distinction is made. In the inference run for Cl^- , the priors are chosen to be of the form $\hat{q}_k(d_k) = 1/d_k$, for $k = 0, 1$. For the inference run for Na^+ ,

the priors $\hat{q}_k(d_k)$, $k = 0, 1$, are still of the same form, but for $\hat{q}_1(d_1)$ we impose the additional constraint that the resulting variance cannot be smaller than 10^{-2} over the ξ -space. This model assumption stems from the fact that given the ξ -dependent noise, the zero variance obtained for the Na^+ conductance at $q_{surf} = 0.265619083 \text{ Coul/m}^2$, see Figure 5.8 (b), would make the inference numerically ill-posed. However, as discussed before, this is an artifact resulting from the finite sampling, and we therefore enforce a small, but non-zero, lower bound on the variance.

In the present work, we sample the posterior density in (5.16) with a Markov chain Monte Carlo (MCMC) method based on the so-called adaptive Metropolis (AM) algorithm [40, 5, 3, 113, 114]. As proposal distribution, we adopt a multivariate Gaussian, centered around the current state of the chain and whose covariance matrix, \mathcal{S} , is built according to

$$\mathcal{S} = \begin{cases} \mathcal{S}_0 & \text{for } t < t_0 \\ \beta \text{Cov}_{1,2,\dots,t} & \text{for } t \geq t_0 \end{cases} \quad (5.17)$$

where t_0 defines the step at which the adaptation is triggered, \mathcal{S}_0 is a fixed covariance used for the initial steps, $\text{Cov}_{1,2,\dots,t}$ denotes the covariance computed using the samples collected by the chain during all previous steps, and β is a parameter that must be fixed before running the chain, and tuned to achieve good mixing and an efficient exploration of the target distribution. In general, for a given MCMC run, multiple trials are needed before the proper value of β is obtained. Consequently, a single value of β does not work properly in all cases, but must be defined *ad hoc*. Unless stated otherwise, the learning time, t_0 , is set to 500 steps and each chain is run for 35000 steps, with the first 15000 steps discarded to eliminate the “burn-in” period, and only the remaining 20000 are used for statistical post-processing.

5.4.3 Bayesian regression: results

The samples obtained from the MCMC sampling can be used via Kernel Density Estimation (KDE) [103, 120, 126], to estimate joint posterior densities of the PC coefficients of the regression function and of the coefficients of the noise variance. Joint posteriors play, in fact, a key role since they contain the information about correlations between the parameters. As a representative result, Figures 5.9 (a,b) show the scatter plots of the chain samples, after removing the burn-in period, obtained for the marginalized joint posterior $\pi(g_0, g_1)$ computed for Na^+ (a) and Cl^- (b), by running the inference for a linear ($P = 1$), quadratic ($P = 2$), cubic ($P = 3$), and quartic ($P = 4$) PC regression function. Note that Figures 5.9 (a,b) are plotted using the same range for the x -axis, while, for clarity, a different range but with the same width is used for the y -axis. Figures 5.9 (a,b) reveal, for both ions, strong correlations arising between the leading, g_0 , and the first-order, g_1 , coefficient of the PC representation.

The Na^+ results show a clear negative correlation, while the opposite is observed for the Cl^- results. This is expected and justified by the trends in the original conductance data shown in Figure 5.8 (a). The result obtained by running the inference with a linear expansion substantially deviates from the ones obtained by using higher-order regression functions, $P \geq 2$, which are in good agreement with each other and this is reflected in the plots by a clear overlapping. These

differences will be discussed in detail in the following. For a given order, P , a comparison of the results in Figures 5.9 (a,b) reveals that the posterior samples obtained for Na^+ have a narrow spread, whereas those obtained for Cl^- are wider. This indicates that the posterior uncertainty in the regression parameters for Na^+ is smaller than the corresponding uncertainty obtained for the Cl^- regression parameters. This result is in accordance with Figure 5.8 (b) which showed that the noise level in the Cl^- conductance data is, on average, larger than that for the Na^+ data. This difference in the noise level amplitude is thus reflected in the joint posteriors shown in Figures 5.9 (a,b). Even though the previous discussion was limited to the posterior $\pi(g_0, g_1)$, similar results are obtained for the joint densities involving the higher-order coefficients, which are omitted for brevity.

Next, we perform a characterization of the posterior uncertainty arising in the full spectrum of PC coefficients defining the regression function. The bottom row of Figure 5.9 shows the marginalized posterior, $\pi(g_k)$, of each PC coefficient g_k , $k = 0, \dots, 4$, obtained via kernel density estimation (KDE) from the inference run using a linear ($P = 1$), quadratic ($P = 2$), cubic ($P = 3$), and quartic ($P = 4$) PC regression function. The results are shown for Na^+ (c) and Cl^- (d). These plots allow us to draw the following key observations. First, they show that the PDFs obtained for the Na^+ coefficients display small spread and are tight around the corresponding means, while those for Cl^- are wider, confirming that the posterior uncertainty arising for the Na^+ results is smaller than that for Cl^- coefficients. Secondly, both cases share the feature of having shapes closely resembling gaussian densities for most of the PC coefficients, thus implying that the maximum a posteriori (MAP) estimates (i.e. the peak values) nearly coincide with the mean values. Finally, note that the posteriors obtained using a linear regression function largely deviate from those based on higher-order expansions.

Figure 5.9 (c) shows that the PC coefficients for Na^+ oscillate between positive and negative values, and that the associated uncertainty is relatively large for the intermediate orders, i.e. g_1 , g_2 and g_3 , while being slightly smaller for g_0 and g_4 . Figure 5.9 (d), on the contrary, shows that the Cl^- coefficients are confined within the positive semi-axis, and reveal mild oscillations. Moreover, the uncertainty in the coefficients seems to be only weakly sensitive to the order, since pdf's plotted in Figures 5.9 (c,d) overall reveal a nearly constant spread across the orders. The previous analysis is presented here to provide a characterization of the uncertainty in the PC coefficients and its dependence on the order. As previously illustrated, however, since large correlations are present between the PC coefficients, we remark that for the present analysis one should rely on the joint posteriors of the PC coefficients to draw meaningful statistics. This is particularly important if one is interested in drawing samples of the PC coefficients, since the marginalized posteriors, $\pi(g_k)$, $k = 0, \dots, P$, shown in Figure 5.9 do not contain, by construction, any information about the correlation.

Figure 5.10 shows the data points (black circles) of the Na^+ (a) and Cl^- (b) conductance, superimposed to the predictions (solid lines) obtained by evaluating the corresponding regression function, M , using the maximum a posteriori (MAP) estimates of the inferred PC coefficients computed from the joint posteriors $\pi(g_0, \dots, g_P)$. The results are plotted as a function of q_{surf} , and obtained for a linear, quadratic, cubic, and quartic expansion. Figure 5.10 shows that for both ions, a linear ($P = 1$) PC representation, M , accurately describes the data only over the limited region of the domain where the conductance is small. This result can be explained as follows. Due to

the fact that we formulated the inference with a ξ -dependent noise model, we are able to capture the variation of the noise over the domain and, thus, regions of small noise impose tight constraint on the regression function. Therefore, if we are inferring a low-order regression function, all its degrees of freedom (i.e its coefficients) are constrained by the infinitesimal variance characterizing the data points in the region of small conductance. Consequently, given that a linear expansion has only two degrees of freedom, it cannot capture the remaining data points. These observation holds for the results of both ions.

As we increase the order, more degrees of freedom are available, and the regression function better approximates the MD conductance data. In particular, Figure 5.10 (a) shows that for the Na^+ conductance, G_{Na^+} , a second-order expansion slightly underestimates the MD data near the most negative value of q_{surf} . The third and fourth-order PC models, instead, both capture well the overall trend of G_{Na^+} . For the Cl^- conductance, the results are similar, see Figure 5.10 (b). The quadratic PC model provides a good approximation, but, similarly to panel (a), underestimates the conductance near the largest value of q_{surf} . The result substantially improves for a third and fourth-order expansions, which are nearly equivalent and provide a good representation of the data across the entire range. Note, also, that in all cases the model predictions are always greater than or equal to zero, as imposed by the prior distribution on the PC coefficients of the regression function. The previous discussion provides a qualitative basis allowing us to draw a first conclusion, namely that third and fourth-order expansions seem to be the most suitable models to capture the data for both Na^+ and Cl^- .

As previously anticipated, we can properly assess *a posteriori* whether an inferred regression function properly captures the behavior of the data, by comparing the inferred behavior of σ^2 with its estimate extracted from the noisy data. Figure 5.11 (a) shows the data-based variances (black circles) of the Na^+ conductance superimposed to the predictions of the corresponding $\sigma^2(\xi)$ obtained by evaluating its PC model (5.14) using the MAP estimate of the PC coefficients $\{d_0, d_1\}$. The results are plotted as a function of the order, P , of the regression function, $M(\xi)$, with a logarithmic scale for the y-axis. The corresponding results for Cl^- are shown in Figure 5.11 (b). Note that, as before, the zero variance obtained for the Na^+ conductance at $q_{surf} = 0.265619083$ Coul/m² is not shown for convenience.

Figures 5.11 (a,b) reflect the qualitative analysis illustrated above. For Na^+ , when the inference is based on a linear PC expansion, the trend of the inferred noise $\sigma^2(\xi)$ is substantially larger than the corresponding data-based estimates across the entire domain, see Figure 5.11 (a). This is due to the fact that a linear model does not capture the trend in the conductance data-points well, as shown by Figure 5.10 (a), and, thus, a model discrepancy effect arises and raises the magnitude of the inferred noise. The result drastically improves for $P \geq 2$. In this case, the corresponding inferred variance $\sigma^2(\xi)$ recovers with good accuracy both the magnitude and trend of the data-based estimate. A similar observation can be made for the variance of Cl^- , as shown by Figure 5.11 (b), where the fourth-order expansion seems to yield the best noise recovery.

Bayes Factor

To substantiate the previous qualitative description, we now apply a model selection analysis using Bayes factor [59]. The Bayes factor is a non-dimensional number that compares two “models” (or hypotheses) made to describe a target set of data, and provides a quantitative measure to discriminate between the two. Note that in this context, the term “model” refers to the *complete* set of parameters that are being inferred. The Bayes factor, in fact, does not depend on a specific subset of parameters, but it integrates over the *entire* parameter space. The second key property is that it automatically includes a penalty for overfitting models [59].

In the present study, a “model” refers to the parameter vector $\theta = \{g_0, \dots, g_p, d_0, d_1\}$, comprising the set of PC coefficients $\{g_0, \dots, g_p\}$ defining a p -th order regression function, M , and the two PC coefficients $\{d_0, d_1\}$ defining the PC expansion of the natural logarithm of the noise variance. Since in our formulation we only vary the order, p , of the regression function, $M(\xi)$, while keeping a fixed linear PCe of the noise variance, we can conveniently denote with θ_p the “model” based on a p -th order expansion for M .

Given two different models, namely θ_{p_1} and θ_{p_2} , associated with regression functions of order p_1 and p_2 , respectively, the corresponding Bayes factor, $B(\theta_{p_1}, \theta_{p_2})$, is given by

$$B(\theta_{p_1}, \theta_{p_2}) = \frac{\int \mathcal{L}(\theta_{p_1}; \mathbf{G}) \Pr(\theta_{p_1}) d\theta_{p_1}}{\int \mathcal{L}(\theta_{p_2}; \mathbf{G}) \Pr(\theta_{p_2}) d\theta_{p_2}}, \quad (5.18)$$

where \mathbf{G} is the data set for G_{Na^+} or G_{Cl^-} used in the inference, and $\mathcal{L}(\theta; \mathbf{G})$ and $\Pr(\theta)$ are the likelihood function and the prior, respectively. Both the numerator and denominator can be interpreted as the integrals of the posterior distribution $\pi(\theta | \mathbf{G})$ obtained for the model parameters θ_{p_1} and θ_{p_2} . The Bayes factor $B(\theta_{p_1}, \theta_{p_2})$ has the following interpretation: the larger its value, the stronger the evidence supporting the model θ_{p_1} . In general, the Bayes factor has to be computed numerically, and several methods are available [59]. In the present work, we rely on Monte Carlo integration. It is customary to report and discuss the (natural) logarithm of the Bayes factor [59]. With this setting, the interpretation is as follows: the more positive the value of $\ln(B(\theta_{p_1}, \theta_{p_2}))$, the stronger the evidence supporting θ_{p_1} . The statement is reversed for negative values.

The results computed for the present case using all models explored, i.e. from first ($p = 1$) to fourth ($p = 4$) order, are reported in Table 5.2. The results obtained for Na^+ indicate that using a *third-order* PC regression function is the most suitable model, while the results for Cl^- support a *fourth-order* regression function.

The explanation of these results stems from the fact that the Bayes factor integrates over all parameters involved in the inference and, thus, it accounts for the accuracy of both the PC regression model, M , as well as the PC model of the noise variance. The previous observations can be explained by looking at Figures 5.10 and 5.11. For Na^+ , e.g., these figures show that a third-order PC model represents with great accuracy the G_{Na^+} data-set and, at the same time, also the corresponding noise variance PC model captures well the spread and trend in the data-based variance. A similar explanation based on a fourth-order PC model, holds for the Cl^- results.

	Na^+				Cl^-			
	$p_2 = 1$	$p_2 = 2$	$p_2 = 3$	$p_2 = 4$	$p_2 = 1$	$p_2 = 2$	$p_2 = 3$	$p_2 = 4$
$p_1 = 1$	–	-18.456	-21.751	-20.542	–	-12.189	-13.643	-18.503
$p_1 = 2$	18.456	–	-3.295	-2.085	12.189	–	-1.453	-6.314
$p_1 = 3$	21.751	3.295	–	1.209	13.643	1.453	–	-4.860
$p_1 = 4$	20.542	2.085	-1.209	–	18.503	6.314	4.860	–

Table 5.2. Computed values of $\ln B(\theta_{p_1}, \theta_{p_2})$, obtained for all four different models and each ion Na^+ and Cl^- . Note that due to the logarithmic scale adopted, for a given ion, the corresponding matrix of values is antisymmetric.

Posterior predictive check and predictive uncertainty

To assess the consistency of the inference analysis, we now perform a posterior predictive check [36]. The analysis consists of the following steps. First, for a given observable and the associated model selected previously, we sample the joint posterior, $\pi(\{g_k\}_{k=0}^P, d_0, d_1)$, to generate 50 sample sets of model parameters, i.e. $\{\mathbf{g}_i, \mathbf{d}_i\}_{i=1}^{50}$. Secondly, each PC-spectrum $\{\mathbf{g}_i\}_{i=1}^{50}$ is used to evaluate the corresponding PC model, $M(\xi)$, over a fine grid in $(-1, 1)$, yielding 50 sets of predictions, \mathbf{f}_i , $i = 1, \dots, 50$, for the conductance. Finally, each set of predictions, \mathbf{f}_i , $i = 1, \dots, 50$, is perturbed at each grid point, ξ , with 30 *i.i.d.* samples, $\{\gamma_j\}_{j=1}^{30}$, drawn from a Gaussian with mean zero and variance $\sigma^2(\xi)$ calculated using its PC model (equation 5.14) based on the i -th PC spectrum \mathbf{d}_i .

The samples of predictions resulting from this procedure are plotted as gray dots in Figure 5.12 for Na^+ (a) and Cl^- (b). Superimposed to the predictive samples, we report the original data color-coded blue for Na^+ (a) and red for Cl^- (b), as well as error bars corresponding to $\mu \pm 3 \tilde{\sigma}$, where $\{\mu, \tilde{\sigma}\}$ are the mean and standard deviation estimated from the MD conductance data at a given sampling node. The results are obtained using a third-order ($p = 3$) model for the PC representation of the Na^+ conductance, and a fourth-order ($p = 4$) expansion for the Cl^- conductance.

Figure 5.12 shows that the predictive samples form a “cloud” demonstrating that these predictions accurately match the distribution of the original conductance data. More specifically, they indicate that the noise model adopted in the inference is appropriate to capture the actual spread in the data and its trend over the space. The results thus confirm that both the parameters of the regression function, i.e. the PC coefficients of M , as well as the hyperparameters, i.e. the coefficients of the PCE of the noise variance, have been properly inferred, and that the model structure is adequate.

To finalize the UQ analysis, we perform a “predictive uncertainty” evaluation to analyze how the posterior uncertainty in the inferred PC coefficients of the model, $M(\xi)$, affects the predictions. The importance of this analysis stems from the fact that for prediction purposes one typically relies on the regression function only, without accounting for the noise model. Exploring the prediction capability of the inferred regression functions for this system is thus a key step. We remark that

the key advantage of inferring a response surface is that it allows one to obtain corresponding predictions for the target conductance over the *whole* range of the wall charge, i.e. not only at the given sampling locations. The inference also yields an even better accuracy in the predictions at the locations where the MD data were collected, since the response surface reflects the macroscale smoothness of the conductance versus the gating wall charge.

To this end, we proceed as follows. For a given observable, we generate 250 sample PC-spectra $\{\mathbf{g}_i\}_{i=1}^{250}$, from the corresponding joint posterior distribution, $\pi(\mathbf{g})$, and use these sample spectra to evaluate the corresponding PC model, $M(\xi)$, on a suitably fine grid over $(-1, 1)$. This yields 250 sets of predictions, $\{\mathbf{f}_i\}_{i=1}^{250}$, of the conductance of a given ion over the stochastic domain $(-1, 1)$. The analysis is run using a third-order ($p = 3$) model for the PCe of the Na^+ conductance, and a fourth-order ($p = 4$) expansion for that of the Cl^- conductance. Figure 5.13 shows the 250 curves obtained for Na^+ (a) and Cl^- (b), and, for reference, we superimpose the original observations (black circles), plotted as a function of the gating charge density, q_{surf} .

Figure 5.13 shows that, in both cases, the curves suitably capture the trend in the original noisy data used to run the inference. Due to the constraints imposed on the PC coefficients during the inference, all curves are non-negative over the space $q_{surf} \in (-0.3, 0.3)$ Coul/m². For the Na^+ results, the “envelope” of predictions has very small variance for large positive values of the gating charge, and spreads out increasingly more as the gating charge becomes negative and large. The opposite holds for the negative ions, where the envelope of realizations is narrow for negative values of the gating charge and widens as the gating charge becomes increasingly positive. These trends were observed before, and reproduce with great accuracy the real trends underlying the data where the variance of G increases with the flux of the particular ionic species. The results reflect the posterior uncertainty in the regression functions obtained from the inference due to the noise in the conductance data. This posterior uncertainty can be reduced, e.g., by running the inference with more data points. In this case, in fact, since more information would be available, the inference would yield posterior distributions for the PC coefficients of the regression function, $M(\xi)$, characterized by smaller uncertainty.

5.5 Conclusions

This article focused on MD simulations of concentration driven ionic flow through a silica nanopore. The system involved a silica pore model connecting two reservoirs containing a solution of sodium (Na^+) and chloride (Cl^-) ions in water. An *ad hoc* concentration control algorithm was developed and implemented to create a counter flow of ions through the pore.

We first explored the dependence of the system on the pore diameter. The behavior of the system at small pore diameters is dominated by size (or steric) effects, favoring the flow of Na^+ . On the other hand, as the pore becomes larger, size effects become weaker and the individual mobilities of the ions become increasingly more important, thus favoring the flow of Cl^- .

We then analyzed the sensitivity of the system to a gating charge. The analysis was imple-

mented using an approach based on a forward propagation of uncertainty. As expected, a negative gating charge enhances the flow of Na^+ while counteracting the flux of Cl^- . Likewise, a positive gating charge enhances the flow of Cl^- and effectively counteracts the flux of Na^+ . The results showed that by varying the magnitude and sign of the gating charge, the nanopore can be made effectively open or closed toward a target ionic species. The results also revealed that, for both ions, the variance obtained from the replica values is positively correlated with the corresponding conductance.

PC representations, constructed using Bayesian regression, were exploited to capture the effect of parametric uncertainty and intrinsic noise in the conductance of both ions. This approach allowed us to properly describe the dependence of the observable on the uncertain input, i.e. the gating charge, and suitably capture the effect of the intrinsic noise in terms of uncertain PC coefficients. To define the noise model, we exploited the observation that the variance of the conductance data for both ions varies approximately linearly with gating charge in a semi-log plot. Hence, the logarithm of the noise variance was parametrized with a linear PC model to capture its space dependence. The results revealed large correlations in the PC coefficients obtained for both ionic conductances, suggesting that, for this case, the joint posteriors play a key role. A Bayes factor analysis was applied to choose the most suitable regression model describing the conductance data of both ions. The results indicated that a third-order PC regression function is the best model to represent the Na^+ data, while a fourth-order expansion is the best model for the Cl^- data. Finally, the UQ analysis was complemented with a posterior predictive check and a model prediction analysis, allowing us to confirm that the noise model adopted in the inference was appropriate to capture the actual spread in the data, its trend over the space, and confirmed the adequacy of the regression model and the underlying assumptions.

The UQ analysis of the silica nanopore flow investigated here is complemented in the second part of the article, which focuses on studying the effect of parametric uncertainties in a subset of the potential parameters. As shown in this article, the inherent noise and heterogeneity of the system sets the need for the application of UQ methods, which can play a key role for improving design capabilities. In fact, they allow one to understand the effect of uncertainties in the nanopore system by providing the theoretical framework and mathematical tools to properly quantify and characterize these sources of uncertainty.

5.6 Appendix: Dual control volume concentration control algorithm

Grand canonical molecular dynamics (GCMD) [101, 42, 119] is well-known and often applied to concentration-driven transport in a dual control volume configuration [4, 100]. It is based on controlling the chemical potential of a given species in target regions using Monte Carlo (MC) techniques to manipulate the corresponding concentrations. For a charged system, however, difficulties arise since the possibility of a net creation or destruction of charge with a GCMD method conflicts with the requirement of a Fast Fourier Transform-based Poisson solver, e.g. PPPM, for

the system to be charge neutral. Also, the inefficiency of MC algorithms in inserting atoms into a dense liquid is well-known [4, 12] and poses a serious limitation on the present study.

5.6.1 Concentration control

We developed a more efficient *ad hoc* approach to control the concentration in two control regions \mathcal{C}_1 and \mathcal{C}_2 , in a manner compatible with the PPPM Poisson solver which requires overall charge neutrality. In fact, the improved efficiency was necessary to make the intensive UQ study feasible. As mentioned, the algorithm was developed by borrowing aspects of GCMD and thermodynamic integration. In contrast to GCMD, the algorithm employed in this study controls the concentration directly and, in some sense, deterministically, as in the well-known thermostats described in [30, 94].

Specifically, the algorithm controls, for a given ionic species, the concentration difference $\Delta c(t)$ defined in Eq. eq. (5.4). The target concentration difference $\overline{\Delta c}$ is obtained by injecting or deleting ions in two control regions $\mathcal{C}_i \subset \mathcal{M}_i$, $i = 1, 2$. The measurement regions \mathcal{M}_1 and \mathcal{M}_2 are chosen to be the left and right halves of the fluid component of the system, shown in Figure 5.1, so that $N_1(t) + N_2(t)$ is equal to the total number of ions of a particular ionic species, and $V_1 = V_2 = \frac{1}{2}V_f$, where V_f is the volume of the fluid. Although the measurement regions could coincide with the control regions where insertions and deletions take place, they are chosen to be the left and right halves of the fluid volume, shown in Figure 5.1, since this enables conservation of the total number of atoms throughout the simulation and, hence, some numerical efficiencies. In the limit that the pore volume $\pi R^2 L_z^{(s)}$ is small compared to the reservoir volume $2L_x L_y L_z^{(w)}$, the concentration based on the control volume will converge to that based on the reservoir volume.

Given a target concentration difference, $\overline{\Delta c}$, the algorithm monitors the error

$$\text{error}_{\Delta c} \equiv \Delta c(t) - \overline{\Delta c} = \frac{N_2(t)}{V_2} - \frac{N_1(t)}{V_1} - \overline{\Delta c} = \frac{\Delta N(t)}{V} - \overline{\Delta c}, \quad (5.19)$$

during the simulation, where $\Delta N(t) \equiv N_2(t) - N_1(t)$ for a given ionic species. If $\Delta c(t) \neq \overline{\Delta c}$, then a integer number $\Delta n = \text{round}[1/2(\Delta N - V\overline{\Delta c})]$ of ions are taken from the control region with an excess of ions and transferred to the control region with a deficit. In addition to the geometric parameters of reservoir size and placement, the *ad hoc* concentration control (CC) introduces a maximum insertion/deletion energy, ε_E , a frequency, n , of swaps of ions between the reservoirs, and a transition number of steps, m , to relax the interaction energy of inserted atoms to the nominal value, $\varepsilon_i \rightarrow \varepsilon$. Every n steps, the concentration error (5.19) is computed and if it is non-zero ions are swapped. The appropriate ions are chosen based on the local insertion/deletion energy, as in a GCMC procedure, where the changes to the Lennard-Jones and short-range Coulomb energies are calculated from Eqs. eq. (5.2) and eq. (5.3), and the long-range Coulomb energy is assumed constant. Upon insertion of the ions, the LJ energy parameter ε of the transferred ions is decreased to ε_0/m , where ε_0 is its original value before the insertion. This is to minimize the disturbance to the existing molecules. Note that the charge of the inserted ions is unchanged to preserve charge neutrality of the system and for simplicity. Subsequently, over $m < n$ steps, ε is returned to its

original value. Note that this gradual transition could also be applied to the deletion of ions, but this was found to be unnecessary with respect to short range interactions. An extension of the present algorithm where the deletions are gradual and applied to the charge, as well as to the short-range interaction ϵ , would also preserve charge neutrality. Beside modifying the energy of the inserted ion, it is assigned a velocity that is the sum of a velocity from the appropriate Boltzmann distribution and the reservoir streaming velocity.

The transition parameters are adjusted to suit the expected flux so that disturbances are minimized and the ions are swapped frequently enough to produce a sufficiently continuous flow. For the present study, we used $n = 100$ steps and $\epsilon_E = 1 eV$ (compared to $k_B T \approx 0.03 eV$). Preliminary studies showed that these were roughly the minimal values for which a similar flow was observed given our target concentration difference of approximately 30 ions. It is possible to extend this algorithm to control the time averaged concentration $\langle \Delta c(t) \rangle$, instead of the instantaneous $\Delta c(t)$ as in the present study, by replacing $\Delta c(t)$ in equation (eq. (5.19)) by $\langle \Delta c(t) \rangle \approx \frac{1}{N_s} \sum_{i=1}^{N_s} \Delta c(t_i)$. This running average would be calculated on a sampling interval n_s , such that $N_s = \text{floor}[t/(n_s \Delta t)]$, smaller than that of the control interval n . This modification would allow for fluctuations in the flow range, and perhaps would be more in-line with a GCMD-based simulation, since only the long-time average concentration difference would be constrained but preliminary studies indicated that this modification produced no significant effects on the observables.

5.6.2 Temperature and momentum control

In addition to controlling the concentration in the control regions \mathcal{C}_1 and \mathcal{C}_2 , the temperature and momentum are controlled via a isokinetic thermostat [30, 54]. Gaussian least constraint minimization [30] leads to augmented Newtonian dynamics

$$m_\alpha \frac{d^2 \mathbf{x}_\alpha}{dt^2} = \mathbf{f}_\alpha^* + m_\alpha \zeta + \lambda m_\alpha \mathbf{v}'_\alpha, \quad (5.20)$$

where \mathbf{x}_α is the position of the α -th atom, m_α its mass, $\mathbf{f}_\alpha^* = -\partial_{\mathbf{x}_\alpha} \Phi$ is the force from the interatomic potential Φ , ζ is a Lagrange multiplier for a momentum constraint, and λ is a multiplier for the temperature constraint. The velocity \mathbf{v}'_α is defined as $\mathbf{v}'_\alpha = \mathbf{v}_\alpha - \bar{\mathbf{v}}$, where \mathbf{v}_α is the velocity of atom α and $\bar{\mathbf{v}} = \frac{1}{M} \mathbf{P}$ the average/streaming velocity of the control region. Furthermore, we define as $M = \sum_\alpha m_\alpha$ and $\mathbf{P} = \sum_\alpha m_\alpha \mathbf{v}_\alpha$ the mass and momentum of the control region, respectively, and N the number of atoms in the control region. The momentum constraint is $\mathbf{g} = \mathbf{P} - \bar{\mathbf{P}} = \mathbf{0}$, where $\bar{\mathbf{P}}$ is the prescribed value of momentum; while the temperature constraint is $h = 3k_B N(T - \bar{T}) = 0$, with \bar{T} being the target temperature and T is the computed temperature given by a kinetic definition:

$$\begin{aligned} T &= \frac{1}{3k_B N} \sum_\alpha m_\alpha \mathbf{v}'_\alpha \cdot \mathbf{v}'_\alpha \\ &= \frac{1}{3k_B N} \left[\sum_\alpha m_\alpha \mathbf{v}_\alpha \cdot \mathbf{v}_\alpha - \frac{1}{M} \mathbf{P} \cdot \mathbf{P} \right]. \end{aligned} \quad (5.21)$$

The approximations of $\dot{\mathbf{P}} = \frac{1}{\Delta t} (\bar{\mathbf{P}} - \mathbf{P})$ and $\dot{T} = \frac{1}{\Delta t} (\bar{T} - T)$ are made to control the thermodynamic variables \mathbf{P} and T directly, i.e. not their rates. These constraints lead to

$$\zeta = \frac{1}{M} \left[\dot{\mathbf{P}} - \sum_{\alpha} \mathbf{f}_{\alpha}^* \right] \approx \frac{1}{M} \left[\frac{1}{\Delta t} (\bar{\mathbf{P}} - \mathbf{P}) - \sum_{\alpha} \mathbf{f}_{\alpha}^* \right], \quad (5.22)$$

and

$$\begin{aligned} \lambda &= \frac{1}{2T} \left[\dot{T} - \frac{2}{3k_B} \sum_{\alpha} \mathbf{f}_{\alpha}^* \cdot \mathbf{v}'_{\alpha} \right] \\ &\approx \frac{1}{2T} \left[\frac{1}{\Delta t} (\bar{T} - T) - \frac{2}{3k_B} \sum_{\alpha} \mathbf{f}_{\alpha}^* \cdot \mathbf{v}'_{\alpha} \right], \end{aligned} \quad (5.23)$$

if we assume the momentum constraint is satisfied for λ and ignore terms dependent on the rates of N and M which vanish at steady state. Note that $\dot{\mathbf{P}} = \mathbf{0}$ for momentum preservation.

Given the SHAKE constraints on the TIP4P water, which affect the rigidity of the water molecules, and the significantly different expectations of streaming velocity for the different ionic species, the temperature and momentum control for the water and the ions is performed independently. More specifically, the temperatures are all the same, and the ions are allowed to preserve their momentum, while the water momentum in the control regions is zeroed.

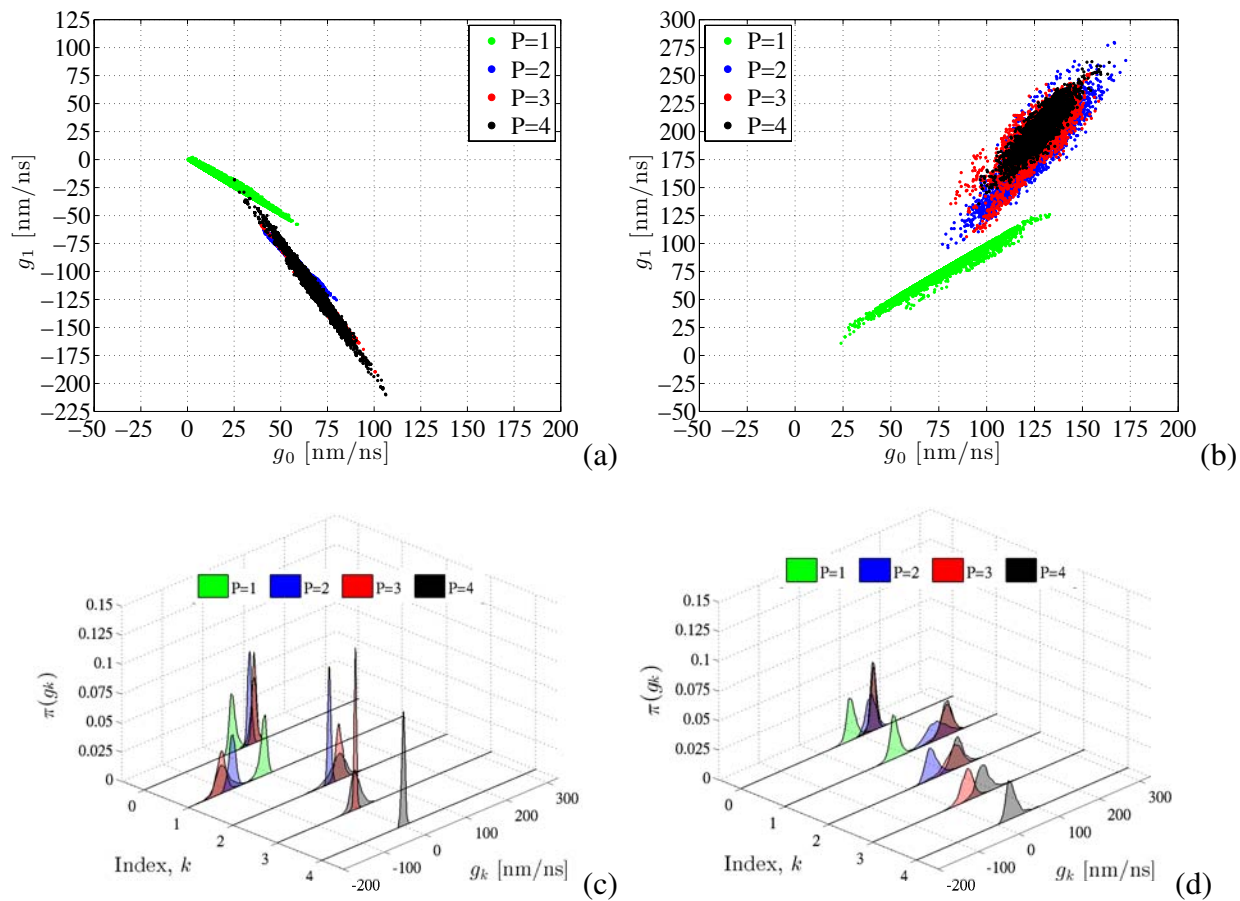


Figure 5.9. Top row: Scatter plots of 20000 MCMC chain samples obtained for $\pi(g_0, g_1)$ for Na^+ (a) and Cl^- (b), extracted from the original MCMC chain by removing the burn-in period comprising the first 15000 samples. Bottom row: marginalized posterior, $\pi(g_k)$, of each PC coefficient g_k , $k = 0, \dots, 4$, obtained via KDE for Na^+ (c) and Cl^- (d). All panels show the results for a linear ($P = 1$), quadratic ($P = 2$), cubic ($P = 3$), and quartic ($P = 4$) expansion.

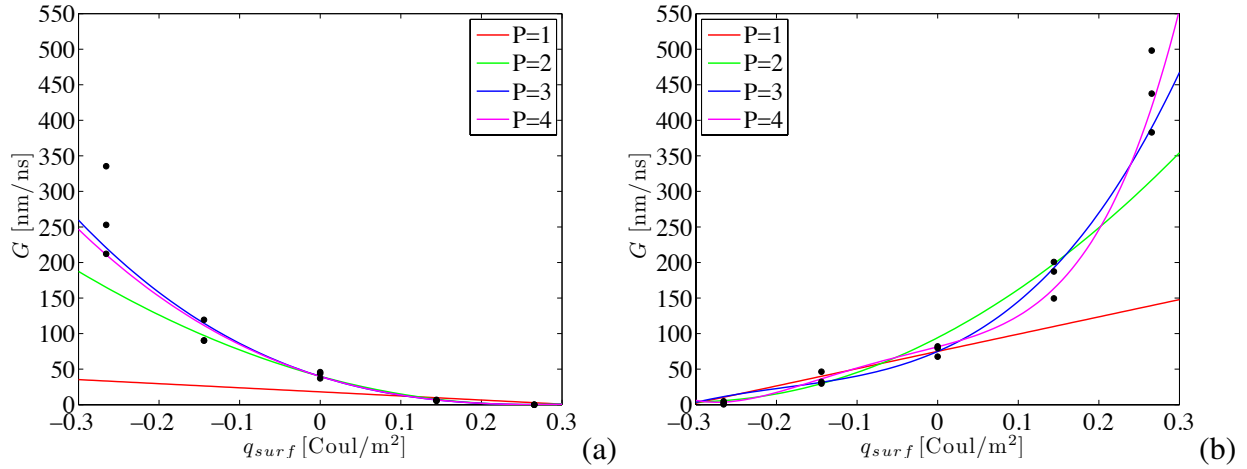


Figure 5.10. Panel (a) shows the comparison between the data points of the Na⁺ (black circles) conductance and the corresponding predictions obtained from the MAP estimate of the PC regression function, $M(\xi)$, computed for a linear ($P = 1$), quadratic ($P = 2$), cubic ($P = 3$), and quartic ($P = 4$) expansion as a function of q_{surf} . The corresponding results for Cl⁻ are shown in panel (b).

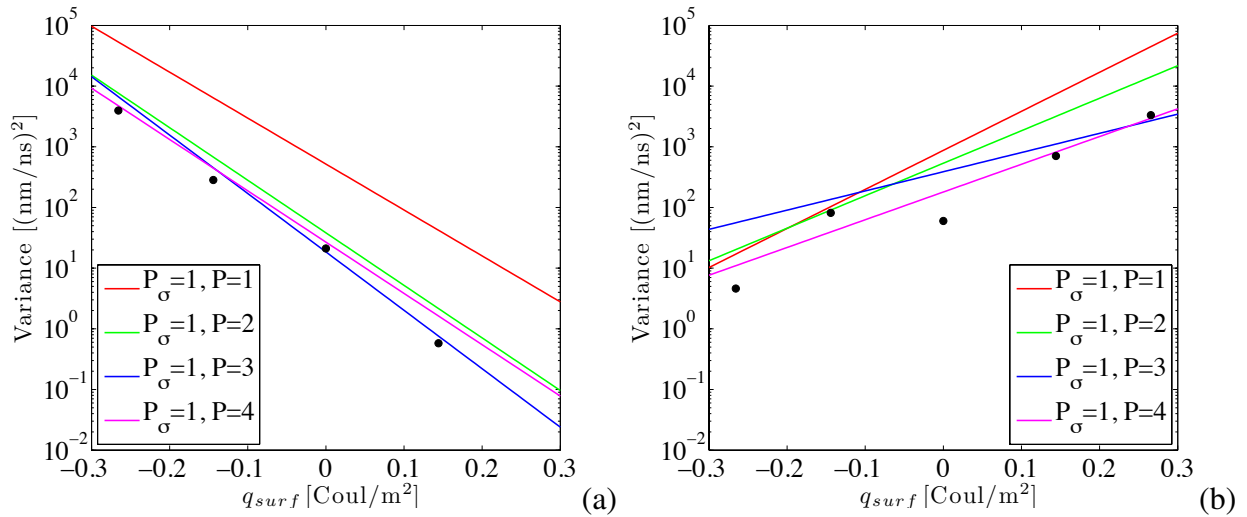


Figure 5.11. Panel (a) shows the data-based variance (black circles) of the Na⁺ conductance versus the corresponding predictions obtained from the MAP estimate of the noise PC coefficients $\{d_0, d_1\}$, as a function of the order, P , of the regression function, $M(\xi)$. The corresponding results for Cl⁻ are shown in panel (b). Both plots are presented with a log scale on the y-axis.

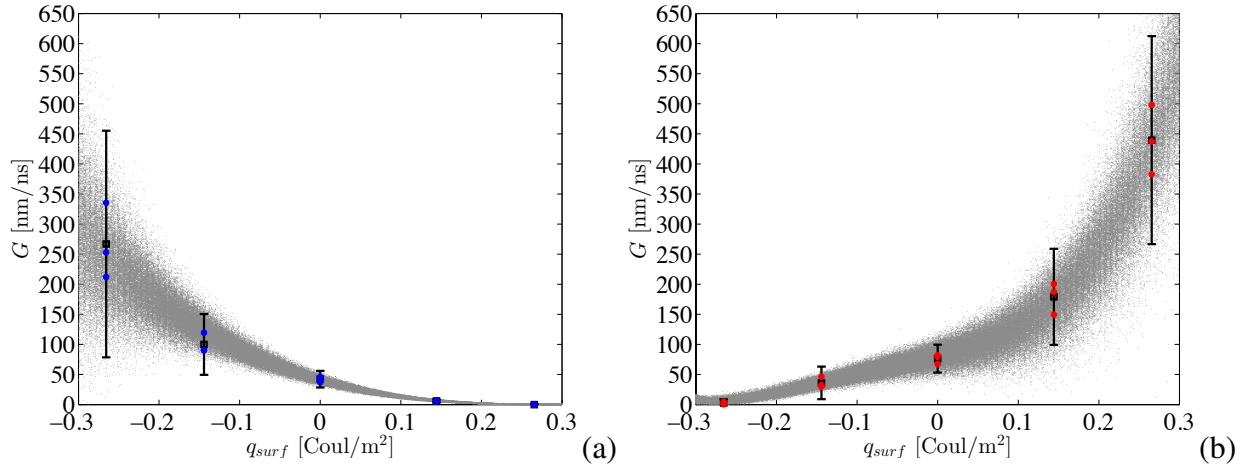


Figure 5.12. Results showing the posterior predictive check samples (gray) obtained for the Na^+ (a) and Cl^- (b) conductance using a third-order and fourth-order PC representation, respectively. Superimposed to the plots, we report the original data color-coded blue for Na^+ and red for Cl^- , and the mean (black square) and error bars for $\pm 3\tilde{\sigma}$, where $\tilde{\sigma}$ is the standard deviation calculated from the original data-set of conductances used in the inference.

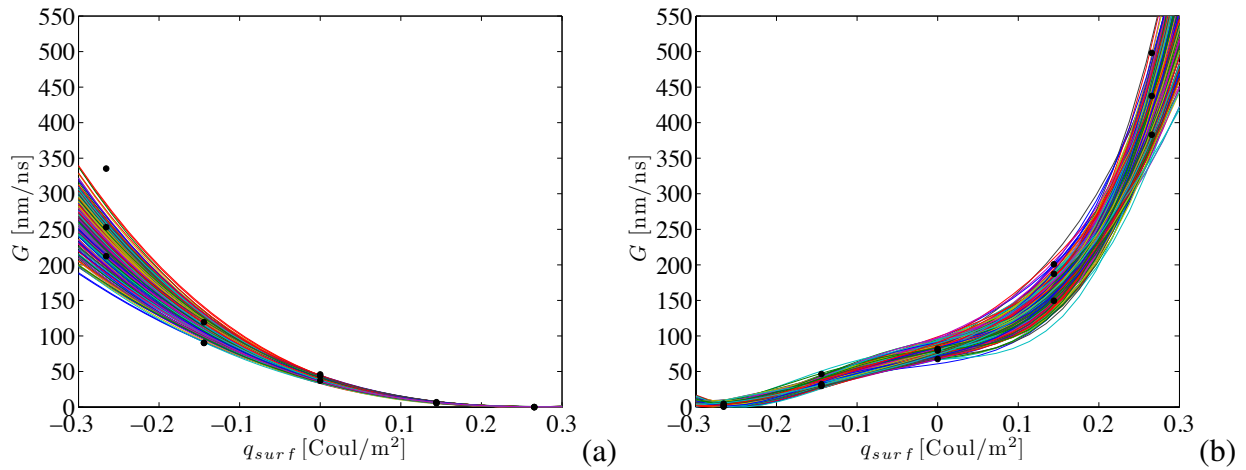


Figure 5.13. Results of the “model uncertainty” analysis obtained for Na^+ (a) and Cl^- (b) showing how the posterior uncertainty in the inferred PC representations of the conductances is reflected in the corresponding predictions.

This page intentionally left blank.

Chapter 6

Finite Element Methods for Fluctuating Hydrodynamics

=====

6.1 Introduction

6.2 Strong Form of Fluctuating Hydrodynamic Equations

The local form for the fluctuating hydrodynamics equations are given by

$$\begin{aligned}\frac{\partial \rho}{\partial t} + \frac{\partial}{\partial \mathbf{x}} \cdot (\rho \mathbf{v}) &= 0, \\ \rho \frac{\partial \mathbf{v}}{\partial t} + \rho \frac{\partial \mathbf{v}}{\partial \mathbf{x}} \cdot \mathbf{v} &= -\nabla p + \frac{\partial}{\partial \mathbf{x}} \cdot (\mathbf{T}),\end{aligned}\tag{6.1}$$

where ρ , \mathbf{v} , p and \mathbf{T} are the density, velocity, pressure and the deviatoric stress tensor, respectively. These quantities may be decomposed as

$$\begin{aligned}\rho &= \rho_0 + \tilde{\rho}, \\ \mathbf{v} &= \mathbf{v}_0 + \tilde{\mathbf{v}}, \\ p &= p_0 + \tilde{p}, \\ \mathbf{T} &= \mathbf{T}_0 + \tilde{\mathbf{T}},\end{aligned}\tag{6.2}$$

where $(\cdot)_0$ denote the averages and $(\tilde{\cdot})$ denote the fluctuations about the average. The average stress tensor is defined as

$$\mathbf{T}_0 = \eta (\nabla \mathbf{v} + \nabla \mathbf{v}^T - \frac{2}{3} \mathbf{I} (\nabla \cdot \mathbf{v})) + \zeta \mathbf{I} (\nabla \cdot \mathbf{v}),\tag{6.3}$$

where η and ζ are the viscosity coefficients. Moreover, the random stress tensor $\tilde{\mathbf{T}}$ follows the fluctuation-dissipation theorem and is given by the correlation tensor

$$\langle \tilde{T}_{ik}(\mathbf{r}_1, t_1) \tilde{T}_{lm}(\mathbf{r}_2, t_2) \rangle = 2T [\eta (\delta_{il} \delta_{km}) + (\zeta - \frac{2}{3} \eta) \delta_{ik} \delta_{lm}] \delta(\mathbf{r}_1 - \mathbf{r}_2) \delta(t_1 - t_2),\tag{6.4}$$

The primary authors of this chapter are K. Mandadapu and J. Templeton.

and can be modeled as Gaussian noise in space and time for all practical purposes. The basic problem is to solve the fluctuating hydrodynamics equations eq. (6.1) under well-posed boundary conditions.

Assuming that the fluctuations are sufficiently small, the fluctuating hydrodynamics equations eq. (6.1) can be linearized about the steady state $(\rho_0, \mathbf{v}_0, p_0)$ to yield

$$\begin{aligned} \frac{\partial \tilde{\rho}}{\partial t} + \frac{\partial}{\partial \mathbf{x}} \cdot (\rho_0 \tilde{\mathbf{v}} + \tilde{\rho} \mathbf{v}_0) &= 0, \\ \rho_0 \frac{\partial \tilde{\mathbf{v}}}{\partial t} + \tilde{\rho} \left(\frac{\partial \mathbf{v}_0}{\partial \mathbf{x}} \cdot \mathbf{v}_0 \right) + \rho_0 \frac{\partial \tilde{\mathbf{v}}}{\partial \mathbf{x}} \cdot \mathbf{v}_0 + \rho_0 \frac{\partial \mathbf{v}_0}{\partial \mathbf{x}} \cdot \tilde{\mathbf{v}} &= -\nabla \tilde{p} + \nabla \cdot \left(\eta (\nabla \tilde{\mathbf{v}} + \nabla \tilde{\mathbf{v}}^T - \frac{2}{3} \mathbf{I}(\nabla \cdot \tilde{\mathbf{v}})) \right. \\ &\quad \left. + \zeta \mathbf{I}(\nabla \cdot \tilde{\mathbf{v}}) \right) + \frac{\partial}{\partial \mathbf{x}} \cdot (\tilde{\mathbf{T}}). \end{aligned} \quad (6.5)$$

The linearized fluctuating hydrodynamics equations can be rewritten in a concise notation as

$$\begin{aligned} \frac{\partial \tilde{\rho}}{\partial t} &= \nabla \cdot \mathbf{J}_1, \\ \rho_0 \frac{\partial \tilde{\mathbf{v}}}{\partial t} &= -\nabla \tilde{p} + \nabla \cdot \mathbf{J}_2 + \frac{\partial}{\partial \mathbf{x}} \cdot (\tilde{\mathbf{T}}). \end{aligned} \quad (6.6)$$

where the corresponding fluxes are given by

$$\begin{aligned} \mathbf{J}_1 &= -(\rho_0 \tilde{\mathbf{v}} + \tilde{\rho} \mathbf{v}_0), \\ \mathbf{J}_2 &= \eta (\nabla \tilde{\mathbf{v}} + \nabla \tilde{\mathbf{v}}^T - \frac{2}{3} \mathbf{I}(\nabla \cdot \tilde{\mathbf{v}})) + \zeta \mathbf{I}(\nabla \cdot \tilde{\mathbf{v}}). \end{aligned} \quad (6.7)$$

6.3 Weak Form of Fluctuating Hydrodynamic Equations

In this section, to apply the finite element approximations to the primary dependent variables, weak forms for the fluctuating hydrodynamics equations are derived. It is assumed that the trial functions satisfy the standard conditions in the space of finite elements. Assuming w^ρ to be the trial function corresponding to the density $\tilde{\rho}$, the weak form for the density equation is given by

$$\int_{\Omega} \frac{\partial \tilde{\rho}}{\partial t} w^\rho \, dv = \int_{\Omega} \nabla \cdot \mathbf{J}_1 w^\rho \, dv. \quad (6.8)$$

In this case, one has two options: (i) Use the standard integration by parts to reduce the derivative on the flux \mathbf{J}_1 by one order and then use the finite element approximations for the density and trial functions. Here, boundary conditions for the density or the pressure must be used to solve the problem. (ii) Use the standard derivative as it is in eq. (6.8) and then perform the standard finite element approximations.

Similarly, assuming the trial function for the velocity operator to be \mathbf{w}^v , the weak form for the linear momentum equation can be written as

$$\int_{\Omega} \rho_0 \frac{\partial \tilde{\mathbf{v}}}{\partial t} \cdot \mathbf{w}^v \, dv = \int_{\Omega} -\nabla \tilde{p} \cdot \mathbf{w}^v \, dv + \int_{\Omega} (\nabla \cdot \mathbf{J}_2) \cdot \mathbf{w}^v \, dv + \int_{\Omega} \left(\frac{\partial}{\partial \mathbf{x}} \cdot (\tilde{\mathbf{T}}) \right) \cdot \mathbf{w}^v \, dv. \quad (6.9)$$

All operations on the terms except the last term on the right-hand side of eq. (6.9) can be performed using standard finite element framework. To this end, using standard integration by parts, eq. (6.9) can be rewritten as

$$\int_{\Omega} \rho_0 \frac{\partial \tilde{\mathbf{v}}}{\partial t} \cdot \mathbf{w}^v \, dv = \int_{\Omega} -\nabla \tilde{p} \cdot \mathbf{w}^v \, dv - \int_{\Omega} \mathbf{J}_2 \cdot \nabla \mathbf{w}^v \, dv + \int_{\Gamma_t} \mathbf{J}_2 \mathbf{n} \cdot \mathbf{w}^v \, dv + \int_{\Omega} \left(\frac{\partial}{\partial \mathbf{x}} \cdot (\tilde{\mathbf{T}}) \right) \cdot \mathbf{w}^v \, dv, \quad (6.10)$$

where Γ_t defines the boundary on which the traction boundary conditions are specified. However, the last term on the right-hand side of eq. (6.9) should be described in detail as it entails spatial white noise and follows Brownian process. It should be mentioned that the integral of the stochastic term in the right-hand side of eq. (6.10) should be understood as an Ito-integral and therefore can be calculated as a limit of the Riemann sums. To this end, it is best to introduce the finite element approximation for the primary dependent variables $(\tilde{\rho}, \tilde{\mathbf{v}}, \tilde{p})$ given by

$$\begin{aligned} \tilde{\rho} &\approx \tilde{\rho}_h = \sum_I \tilde{\rho}_I N_I(\mathbf{x}), \\ \tilde{\mathbf{v}} &\approx \tilde{\mathbf{v}}_h = \sum_I \tilde{\mathbf{v}}_I N_I(\mathbf{x}), \\ \tilde{p} &\approx \tilde{p}_h = \sum_I \tilde{p}_I N_I(\mathbf{x}), \end{aligned} \quad (6.11)$$

where $(\cdot)_I$ are the values of the quantities at the element nodes and $N_I(\mathbf{x})$ are the shape functions corresponding to the node I . To understand the effects of the random term in the momentum equation eq. (6.10), consider the case of 1-dimensional shape function of any node I corresponding to an element Ω^e of size L given by

$$N_I(\mathbf{x}) = 1 - \left(\frac{x}{L}\right), \quad x \in [0, L]. \quad (6.12)$$

In this case, the integral of the random term over the element Ω^e is given by

$$\begin{aligned} \int_{\Omega^e} \frac{\partial}{\partial x} \tilde{\mathbf{T}} N_I(x) \, dx &= \int_0^L \frac{\partial \tilde{\mathbf{T}}}{\partial x} \left(1 - \frac{x}{L}\right) \, dx \\ &= \lim_{N \rightarrow \infty} \sum_{n=1}^N \left(\tilde{T}(n\Delta x) - \tilde{T}((n-1)\Delta x) \right) \left(1 - \frac{n}{N}\right) \end{aligned} \quad (6.13)$$

where the second equality is rewritten as the limit of a Reimann sum over length intervals of $\Delta x = \frac{L}{N}$ as mentioned above. Since $\tilde{T}(x)$ is modeled as a Weiner process, $\tilde{T}(x_1) - \tilde{T}(x_2)$ is a Gaussian distribution with mean 0 and variance $x_1 - x_2$. Therefore, the term on the right-hand side of eq. (6.13) can be calculated as a limit of the sum of Gaussian random variables where the mean is zero and the variance is given by

$$\begin{aligned} &Var \left(\lim_{N \rightarrow \infty} \sum_{n=1}^N \left(\tilde{T}(n\Delta x) - \tilde{T}((n-1)\Delta x) \right) \left(1 - \frac{n}{N}\right) \right) \\ &= \lim_{N \rightarrow \infty} \sum_{n=1}^N Var \left(\left(\tilde{T}(n\Delta x) - \tilde{T}((n-1)\Delta x) \right) \left(1 - \frac{n}{N}\right) \right), \\ &= \lim_{N \rightarrow \infty} \sum_{n=1}^N \left(1 - \frac{n}{N}\right)^2 \frac{L}{N}, \\ &= L/3. \end{aligned} \quad (6.14)$$

It can be seen that the variance scales as the size of the size of the element. If the noise is normalized with the volume with the element, then the fluctuations or the random term has a variance of $\frac{1}{3L}$. This shows that the fluctuations drop as the averaging process includes larger volumes and the system of equations yield the regular Navier-Stokes equations. It is important to note that the random term in eq. (6.9) should not be converted using integration by parts like in regular finite element method and should be calculated in its original form to be able to utilize the Ito calculus for stochastic processes.

Chapter 7

Conclusions

The efforts in this work have focused on developing capabilities to predictively and efficiently simulate fluid processes at the nanoscale by combining atomistic and continuum descriptions of materials. Of particular importance are electrolyte flows through nanopores and at solid/fluid interfaces with molecular solvents. Progress in addressing both types of problems has been made in this project. Fluid-based problems require conserving mass and species between the continuum and atomic regions, so a concentration regulation methodology based on approximating Grand-Canonical Monte Carlo methods has been developed and demonstrated. Simultaneous control of both momentum and energy is as needed, and it too has solved. Finally, this project has derived, to the best of the authors' knowledge, the first theory for incorporating molecules into a multiscale framework.

Complementing the theory and methods development has been software engineering. The methods described in this work are available through LAMMPS' AtC package. It includes example problems demonstrating these techniques in their intended application to guide domain-specific experts in utilizing the code to solve their problems. Indeed, some of the methods presented in this work are already being applied to model electric double layers and compare those models with experiments. Further development efforts are planned to concurrently couple molecular fluids to a continuum model and complete new theories which describe the charge distribution in semi-conducting electrodes.

To increase the utility of the code, this project also has partially sponsored two computer science clinic projects at Harvey Mudd College. Associated reports can be found in [34, 6]. Both clinics worked on parallelizing the finite element operations in the code. While the data is not decomposed, calculation of finite element integrals is now distributed as are finite element matrix/vector multiplications. Atomistic calculations were already parallelized within the LAMMPS code. The result is a code which is significantly more scalable software package which can be applied to a greater range of problems. Further increasing the code's usefulness was the implementation of an unstructured mesh capability to better represent realistic geometries. Supporting this feature has been the addition of different element types, e.g. tetrahedrons, and higher-order polynomial bases.

The combination of new theory and enhanced software features has provided Sandia National Laboratories with a distinguishing capability to model nano- and micro-fluidic devices relevant to its nuclear weapons and energy storage missions. Future work remains to extend the elec-

tric field models and molecular multiscale coupling. However, the most important next step is to develop mesoscale models, i.e., atomistically-informed continuum models, for next generation fidelity. There is also a strong need for improved coupling between atomistic and quantum descriptions of matter to improve modeling of electron transport and fluid/solid interactions. The current AtC framework provides an excellent starting point for such efforts, as well as being immediately relevant to perform previously infeasible calculations to better understand fluid processes at the nanoscale.

References

- [1] T. W. Allen, S. Kuyucak, and S.-H. Chung. The effect of hydrophobic and hydrophilic channel walls on the structure and diffusion of water and ions. *The Journal of Chemical Physics*, 111(17):7985–7999, 1999.
- [2] G. Anciaux, S.B. Ramisetty, and J.F. Molinari. A finite temperature bridging domain method for MD-FE coupling and application to a contact problem. *Comput. Methods Appl. Mech. Eng.*, 62(5):5989–5997, 2000.
- [3] C. Andrieu and E. Moulines. On the ergodicity properties of some adaptive MCMC algorithms. *Ann. Appl. Prob.*, 16:1462–1505, 2006.
- [4] G Arya, HC Chang, and EJ Maginn. A critical comparison of equilibrium, non-equilibrium and boundary-driven molecular dynamics techniques for studying transport in microporous materials. *The Journal of Chemical Physics*, 115(17):8112–8124, 2001.
- [5] Y. F. Atchadé and J. S. Rosenthal. On adaptive markov chain monte carlo algorithms. *Bernoulli*, 11:815–828, 2005.
- [6] J. Bandes-Storch, J. Jonsson, J. Librande, and M. Morton. Development of an Advanced Finite Element Implementation for Atomistic-to-Continuum Modeling. Technical report, Harvey Mudd College Computer Science Clinic, May 2013.
- [7] G. I. Barenblatt. *Scaling*. Cambridge University Press, Cambridge, 2003.
- [8] Peter H. Barry and Joseph W. Lynch. Liquid junction potentials and small cell effects in patch-clamp analysis. *Journal of Membrane Biology*, 121:101–117, 1991.
- [9] M.R. Battaglia, A.D. Buckingham, and J.H. Williams. The electric quadrupole moments of benzene and hexafluorobenzene. *Chem. Phys. Lett.*, 78(3):421–423, 1981.
- [10] Oliver Beckstein, Philip C. Biggin, and Mark S. P. Sansom. A hydrophobic gating mechanism for nanopores. *The Journal of Physical Chemistry B*, 105(51):12902–12905, 2001.
- [11] Berthelot, D. Sur le mélange des gaz. *Comptes rendus hebdomadaires des séances de l’Académie des Sciences*, 126:1703–1855, 1898.
- [12] Sharada Boinepalli and Phil Attard. Grand canonical molecular dynamics. *The Journal of Chemical Physics*, 119(24):12769–12775, 2003.
- [13] D.J. Bonthuis, S. Gekle, and R.R. Netz. Dielectric profile of interfacial water and its effect on double-layer capacitance. *Phys. Rev. Lett.*, 107(16):166102, 2011.

- [14] I. Borukhov, D. Andelman, and H. Orland. Steric effects in electrolytes: A modified Poisson–Boltzmann equation. *Phys. Rev. Lett.*, 79:435–438, 1997.
- [15] I. Borukhov, D. Andelman, and H. Orland. Adsorption of large ions from an electrolyte solution: A modified Poisson–Boltzmann equation. *Electrochim. Acta*, 46:221–229, 2000.
- [16] D. L. Chapman. A contribution to the theory of electrocapillarity. *Phil. Mag.*, 25(148):475–481, 1913.
- [17] D. Chen, J. Lear, and B. Eisenberg. Permeation through an open channel: Poisson-Nernst-Planck theory of a synthetic ionic channel. *Biophysical Journal*, 72(1):97 – 116, 1997.
- [18] A.J. Chorin. Numerical solution of the Navier-Stokes equations. *Math Comp.*, 22:745–762, 1968.
- [19] Snehasis Chowdhuri and Amalendu Chandra. Molecular dynamics simulations of aqueous nacl and kcl solutions: Effects of ion concentration on the single-particle, pair, and collective dynamical properties of ions and water molecules. *The Journal of Chemical Physics*, 115(8):3732–3741, 2001.
- [20] Kyoung-Yong Chun and Pieter Stroeve. External control of ion transport in nanoporous membranes with surfaces modified with self-assembled monolayers. *Langmuir*, 17(17):5271–5275, 2001.
- [21] T. H. Cormen, C. E. Leiserson, R. L. Rivest, and C. Stein. *Introduction to Algorithms*. MIT press, 1990.
- [22] Roger F. Cracknell, David Nicholson, and Nicholas Quirke. Direct molecular dynamics simulation of flow down a chemical potential gradient in a slit-shaped micropore. *Phys. Rev. Lett.*, 74:2463–2466, Mar 1995.
- [23] Eduardo R. Cruz-Chu, Aleksei Aksimentiev, and Klaus Schulten. Watersilica force field for simulating nanodevices. *The Journal of Physical Chemistry B*, 110(43):21497–21508, 2006.
- [24] Hirofumi Daiguji, Peidong Yang, and Arun Majumdar. Ion transport in nanofluidic channels. *Nano Letters*, 4(1):137–142, 2004.
- [25] J.A. Dean. *Langes Handbook of Chemistry*. 15th Edition, McGraw-Hill, New York, 1999.
- [26] B. J. Debuschere, M. A. Hickner, F.J. Zendejas, H. Adalsteinsson, H.M. Tran, K.R. Long, H.N. Najm, D.A. Chinn, M.S. Kent, and B.A. Simmons. Computational and experimental study of nanoporous membranes for water desalination and decontamination. Technical report, Sandia National Laboratories, 2008.
- [27] Léo Degrève and Fernanda M. Mazzé. Molecular simulation of licl aqueous solutions. *Molecular Physics*, 101(10):1443–1453, 2003.

- [28] J. Dzubiella, R. J. Allen, and J.-P. Hansen. Electric field-controlled water permeation coupled to ion transport through a nanopore. *The Journal of Chemical Physics*, 120(11):5001–5004, 2004.
- [29] J. Dzubiella and J.-P. Hansen. Electric-field-controlled water and ion permeation of a hydrophobic nanopore. *The Journal of Chemical Physics*, 122(23):234706, 2005.
- [30] Denis J. Evans, William G. Hoover, Bruce H. Failor, Bill Moran, and Anthony J. C. Ladd. Nonequilibrium molecular dynamics via Gauss’s principle of least constraint. *Phys. Rev. A*, 28:1016–1021, 1983.
- [31] D.J. Evans, W.G. Hoover, B.H. Failor, B. Moran, and A.J.C. Ladd. Nonequilibrium molecular dynamics via Gauss’s principle of least constraint. *Phys. Rev. A*, 28(2):1016 – 21, 1983.
- [32] Carl S. Ewig, Thomas S. Thacher, and Arnold T. Hagler. Derivation of class ii force fields. 7. nonbonded force field parameters for organic compounds. *The Journal of Physical Chemistry B*, 103(33):6998–7014, 1999.
- [33] Daan Frenkel and Anthony J. C. Ladd. New monte carlo method to compute the free energy of arbitrary solids. application to the fcc and hcp phases of hard spheres. *The Journal of Chemical Physics*, 81(7):3188–3193, 1984.
- [34] A. Gable, S. Laguna, T. Schramm, and F. Tay. Parallelizing and Enriching AtC, a Finite Element Extension for the LAMMPS Molecular Dynamics Code. Technical report, Harvey Mudd College Computer Science Clinic, May 2012.
- [35] C. Gear. *Numerical Initial Value Problems in Ordinary Differential Equations*. Prentice-Hall, 1971.
- [36] A. Gelman, J.Ḃ. Carlin, H.Ḃ. Stern, and D.Ḃ. Rubin. *Bayesian Data Analysis*. Chapman and Hall/CRC, 2004.
- [37] R. Ghanem and P Spanos. *Stochastic Finite Elements: A Spectral Approach*. Springer Verlag, New York, 1991.
- [38] R.G. Ghanem and A. Doostan. On the construction and analysis of stochastic models: Characterization and propagation of the errors associated with limited data. *J. Comput. Phys.*, 217(1):63 – 81, 2006.
- [39] G. Gouy. Sur la constitution de la charge electrique à la surface d’un electrolyte. *J. Phys. Radium*, 9:457–468, 1910.
- [40] H. Haario, E. Saksman, and J. Tamminen. An adaptive metropolis algorithm. *Bernoulli*, 7:223–242, 2001.
- [41] J. Haile. *Molecular Dynamics Simulation: Elementary Methods*. Wiley, 1992.
- [42] Grant S. Heffelfinger and Frank van Swol. Diffusion in Lennard-Jones fluids using dual control volume grand canonical molecular dynamics simulation (DCV-GCMD). *The Journal of Chemical Physics*, 100(10):7548–7552, 1994.

- [43] T. N. Heinz, W. F. van Gunsteren, and P. H. Hünenberger. Comparison of four methods to compute the dielectric permittivity of liquids from molecular dynamics simulations. *J. Chem. Phys.*, 115:1125–1136, 2001.
- [44] Chuen Ho, Rui Qiao, Jiunn B. Heng, Aveek Chatterjee, Rolf J. Timp, Narayana R. Aluru, and Gregory Timp. Electrolytic transport through a synthetic nanometer-diameter pore. *Proceedings of the National Academy of Sciences of the United States of America*, 102(30):10445–10450, 2005.
- [45] R. W. Hockney and J. W. Eastwood. *Computer Simulation Using Particles*. Adam Hilger, New York, 1989.
- [46] Hockney, R.W. and Eastwood, J.W. *Computer Simulation using Particles*. American Institute of Physics, New York: McGraw-Hill, 1988.
- [47] W. Hoover. Canonical dynamics - equilibrium phase-space distributions. *Phys. Rev. A*, 31(3):1695 – 1697, 1985.
- [48] W. G. Hoover. Canonical dynamics: Equilibrium phase-space distributions. *Phys. Rev. A*, 31:1695–1697, 1985.
- [49] T.J.R. Hughes. *The Finite Element Method: Linear Static and Dynamic Finite Element Analysis*. Dover Publications, 2000.
- [50] R. J. Hunter. *Foundations of colloid science*. Oxford University Press, 2001.
- [51] Ciprian Iacob, Joshua Rume Sangoro, Periklis Papadopoulos, Tilman Schubert, Sergej Naumov, Rustem Valiullin, Jorg Karger, and Friedrich Kremer. Charge transport and diffusion of ionic liquids in nanoporous silica membranes. *Phys. Chem. Chem. Phys.*, 12:13798–13803, 2010.
- [52] Wonpil Im, Stefan Seefeld, and Benoît Roux. A grand canonical Monte Carlo-Brownian dynamics algorithm for simulating ion channels. *Biophysical Journal*, 79(2):788 – 801, 2000.
- [53] J. H. Irving and J. G. Kirkwood. The statistical mechanical theory of transport processes. IV. The equations of hydrodynamics. *J. Chem. Phys.*, 18:817–829, 1950.
- [54] D.S. Ivanov and L.V. Zhigilei. Combined atomistic-continuum modeling of short-pulse laser melting and disintegration of metal films. *Phys. Rev. B*, 68:064114, 2003.
- [55] J. D. Jackson. *Classical electrodynamics*. John Wiley and Sons, New York, 1999.
- [56] W. L. Jorgensen, J. Chandrasekhar, J. D. Madura, R. W. Impey, and M. L. Klein. Comparison of simple potential functions for simulating liquid water. *J. Chem. Phys.*, 79:926–935, 1983.
- [57] W. L. Jorgensen and J. D. Madura. Temperature and size dependence for Monte Carlo simulations of TIP4P water. *Mol. Phys.*, 56:1381–1392, 1985.

- [58] Eric Kalman, Olivier Sudre, Ivan Vlasiouk, and Zuzanna Siwy. Control of ionic transport through gated single conical nanopores. *Analytical and Bioanalytical Chemistry*, 394:413–419, 2009.
- [59] Robert E. Kass and Adrian E. Raftery. Bayes factors. *Journal of the American Statistical Association*, 90(430):773–795, 1995.
- [60] S.M. Kathmann, I-F.W. Kuo, and C.J. Mundy. Electronic effects on the surface potential at the vapor-liquid interface of water. *J. Am. Chem. Soc.*, 130(49):16556–16561, 2008.
- [61] S.M. Kathmann, I-F.W. Kuo, C.J. Mundy, and G.K. Schenter. Understanding the surface potential of water. *J. Phys. Chem. B*, 115(15):4369–4377, 2011.
- [62] Ulrich F. Keyser. Controlling molecular transport through nanopores. *Journal of The Royal Society Interface*, 2011.
- [63] M. S. Kilic and M. Bazant. Steric effects in the dynamics of electrolytes at large applied voltages. I. Double-layer charging. *Phys. Rev. E*, 75:021502–1–16, 2007.
- [64] D. Kim and E. Darve. Molecular dynamics simulation of electro-osmotic flows in rough wall nanochannels. *Phys. Rev. E*, 73:051203–1–12, 2006.
- [65] J. Kim and P. Moin. Application of a fractional-step method to incompressible Navier-Stokes equations. *J. Comp. Phys.*, 59:308–323, 1985.
- [66] J. G. Kirkwood. The statistical mechanical theory of transport processes. I. General theory. *J. Chem. Phys.*, 14:180–202, 1946.
- [67] John G. Kirkwood. Statistical mechanics of fluid mixtures. *The Journal of Chemical Physics*, 3(5):300–313, 1935.
- [68] R. Kobayashi, T. Nakamura, and S. Ogata. A coupled molecular dynamics/coarse-grained-particle method for dynamic simulation of crack growth at finite temperatures. *Mat. Trans.*, 52(8):1603–1610, 2011.
- [69] R. Kobayashi, T. Nakamura, and S. Ogata. Concurrent hybrid simulation of fracture dynamics of suspended graphene at finite temperatures. *Trans. Mat. Res. Soc. Japan*, 37(1):7–10, 2012.
- [70] S. Koneshan, Jayendran C. Rasaiah, R. M. Lynden-Bell, and S. H. Lee. Solvent structure, dynamics, and ion mobility in aqueous solutions at 25 c. *The Journal of Physical Chemistry B*, 102(21):4193–4204, 1998.
- [71] Y. Kulkarni, J. Knap, and M. Ortiz. A variational approach to coarse graining of equilibrium and non-equilibrium atomistic description at finite temperature. *J. Mech. Phys. Sol.*, 56(4):1417–1449, 2008.
- [72] K.E. Laidig. The atomic basis of the molecular quadrupole moments of benzene and hexafluorobenzene. *Chem. Phys. Lett.*, 185(5-6):483–389, 1991.

- [73] L. D. Landau, E. M. Lifshitz, and L. P. Pitaevskii. *Electrodynamics of Continuous Media*. Butterworth-Heinemann, Oxford, 1984.
- [74] O. P. Le Maître and O. M. Knio. *Spectral Methods for Uncertainty Quantification*. Springer, New York, 2010.
- [75] Y. Le Page and G. Donnay. Refinement of the crystal structure of low-quartz. *Acta Crystallographica Section B*, 32(8):2456–2459, Aug 1976.
- [76] J. W. Lee, J. A. Templeton, K. K. Mandadapu, and J. A. Zimmerman. Investigation of various molecular dynamics models of electric double layers in nanochannels. *J. Chem. Theory Comput.*, 2013 (Submitted).
- [77] J.W. Lee, R.H. Nilson, J.A. Templeton, S.K. Griffiths, A. Kung, and B.M. Wong. Comparison of molecular dynamics with classical density functional and poisson-boltzmann theories of the electric double layer in nanochannels. *J. Chem. Theor. Comp.*, 8(6):2012–2022, 2012.
- [78] Song Hi Lee and Jayendran C. Rasaiah. Molecular dynamics simulation of ion mobility. 2. alkali metal and halide ions using the spc/e model for water at 25 c. *The Journal of Physical Chemistry*, 100(4):1420–1425, 1996.
- [79] Kevin Leung, Susan B. Rempe, and Christian D. Lorenz. Salt permeation and exclusion in hydroxylated and functionalized silica pores. *Phys. Rev. Lett.*, 96:095504, 2006.
- [80] J. Liu, S. Chen, X. Nie, and M.O. Robbins. A continuum-atomistic simulation of heat transfer in micro- and nano-flows. *J. Comp. Phys.*, 227:279–291, 2007.
- [81] Yang Liu, David E. Huber, Vincent Tabard-Cossa, and Robert W. Dutton. Descreening of field effect in electrically gated nanopores. *Applied Physics Letters*, 97(14):143109, 2010.
- [82] Pedro E. M. Lopes, Vladimir Murashov, Mouhsine Tazi, Eugene Demchuk, and Alexander D. MacKerell. Development of an empirical force field for silica. application to the quartzwater interface. *The Journal of Physical Chemistry B*, 110(6):2782–2792, 2006.
- [83] Lorentz, H.A. Ueber die anwendung des satzes vom virial in der kinetischen theorie der gase. *Annalen der Physik*, 248(1):127–136, 1881.
- [84] Christian D. Lorenz, Paul S. Crozier, Joshua A. Anderson, and Alex Travesset. Molecular dynamics of ionic transport and electrokinetic effects in realistic silica channels. *The Journal of Physical Chemistry C*, 112(27):10222–10232, 2008.
- [85] RM LyndenBell and JC Rasaiah. Mobility and solvation of ions in channels. *The Journal of Chemical Physics*, 105(20):9266–9280, 1996.
- [86] AD MacKerell, D Bashford, M Bellott, RL Dunbrack, JD Evanseck, MJ Field, S Fischer, J Gao, H Guo, S Ha, D Joseph-McCarthy, L Kuchnir, K Kuczera, FTK Lau, C Matos, S Michnick, T Ngo, DT Nguyen, B Prodhom, WE Reiher, B Roux, M Schlenkrich, JC Smith, R Stote, J Straub, M Watanabe, J Wiorcikiewicz-Kuczera, D Yin, and M Karplus. All-atom empirical potential for molecular modeling and dynamics studies of proteins. *J. Phys. Chem. B*, 102(18):3586–3616, 1998.

- [87] J. J. Magda, M. Tirrell, and H. T. Davis. Molecular dynamics of narrow, liquid-filled pores. *J. Chem. Phys.*, 83:1888–1901, 1985.
- [88] M. W. Mahoney and W. L. Jorgensen. A five-site model for liquid water and the reproduction of the density anomaly by rigid, nonpolarizable potential functions. *J. Chem. Phys.*, 112:8910–8922, 2000.
- [89] K. K. Mandadapu, A. Sengupta, and P. Papadopoulos. A homogenization method for thermomechanical continua using extensive physical quantities. *Proc. R. Soc. A*, 468:1696–1715, 2012.
- [90] K.K. Mandadapu, J.A. Templeton, and J.W. Lee. Polarization as a field variable from molecular dynamics simulations. *J. Chem. Phys.*, 139:054115, 2013.
- [91] B Mannfors, K Palmo, and S Krimm. A new electrostatic model for molecular mechanics force fields. *Journal of Molecular Structure*, 556(1-3):1–21, 2000.
- [92] J. R. Maple, M.-J. Hwang, T. P. Stockfisch, U. Dinur, M. Waldman, C. S. Ewig, and A. T. Hagler. Derivation of class ii force fields. i. methodology and quantum force field for the alkyl functional group and alkane molecules. *Journal of Computational Chemistry*, 15(2):162–182, 1994.
- [93] R.E. Miller and E.B. Tadmor. A unified framework and performance benchmark of fourteen multiscale atomistic/continuum coupling methods. *Mod. Sim. Mat. Sci. Eng.*, 17(5):053001, 2009.
- [94] F. Muller-Plathe. A simple nonequilibrium molecular dynamics method for calculating the thermal conductivity. *J. Chem. Phys.*, 106(14):6082–6085, 1997.
- [95] H.N. Najm, B.J. Debusschere, Y.M. Marzouk, S. Widmer, and O.P. Le Maître. Uncertainty quantification in chemical systems. *Internat. J. Numer. Methods Engrg.*, 80:789–814, 2009.
- [96] Saima Nasir, Mubarak Ali, and Wolfgang Ensinger. Thermally controlled permeation of ionic molecules through synthetic nanopores functionalized with amine-terminated polymer brushes. *Nanotechnology*, 23(22):225502, 2012.
- [97] Matsuhiko Nishizawa, Vinod P. Menon, and Charles R. Martin. Metal nanotubule membranes with electrochemically switchable ion-transport selectivity. *Science*, 268(5211):700–702, 1995.
- [98] S. Nosé. A molecular dynamics method for simulations in the canonical ensemble. *Mol. Phys.*, 52(2):255–268, 1984.
- [99] Nosé, S. A unified formulation of the constant temperature molecular dynamics methods. *Journal of Chemical Physics*, 81(1):511–519, 1984.
- [100] George K. Papadopoulos. Diffusivity of CH₄ in model silica nanopores: Molecular dynamics and quasichemical mean field theory. *Molecular Simulation*, 31(1):57–66, 2005.

- [101] Aphrodite Papadopoulou, Ezra D. Becker, Mark Lupkowski, and Frank van Swol. Molecular dynamics and monte carlo simulations in the grand canonical ensemble: Local versus global control. *The Journal of Chemical Physics*, 98(6):4897–4908, 1993.
- [102] H.S. Park, E.G. Karpov, W.K. Liu, and P.A. Klein. The bridging scale for two-dimensional atomistic/continuum coupling. *Phil. Mag.*, 85(1):79–113, 2005.
- [103] E. Parzen. On estimation of a probability density function and mode. *Ann. Math. Stat.*, 33:1065–1076, 1962.
- [104] M. Patra and M. Karttunen. Systematic comparison of force fields for microscopic simulations of NaCl in aqueous solutions: Diffusion, free energy of hydration, and structural properties. *Journal of Computational Chemistry*, 25(5):678–689, 2004.
- [105] Christine Peter and Gerhard Hummer. Ion transport through membrane-spanning nanopores studied by molecular dynamics simulations and continuum electrostatics calculations. *Biophysical Journal*, 89(4):2222 – 2234, 2005.
- [106] S. J. Plimpton. Fast parallel algorithms for short-range molecular dynamics. *J. Comp. Phys.*, 117:1–19, 1995. See also <http://lammps.sandia.gov/>.
- [107] S. J. Plimpton. Fast parallel algorithms for short-range molecular dynamics. *J. Comput. Phys.*, 117:1–19, 1995.
- [108] D. J. Price and C. L. Brooks. A modified TIP3P water potential for simulation with Ewald summation. *J. Chem. Phys.*, 121:10096–10103, 2004.
- [109] Yong-Jian Qiu and John R. Reynolds. Dopant anion controlled ion transport behavior of polypyrrole. *Polymer Engineering & Science*, 31(6):417–421, 1991.
- [110] F. Rizzi, R.E. Jones, B.J. Debuscherre, and O.M. Knio. Uncertainty quantification in md simulations of concentration driven ionic flow through a silica nano pore. i. sensitivity to physical parameters of the pore. *J. Chem. Phys.*, 138:194104, 2013.
- [111] F. Rizzi, H.N. Najm, B.J. Debusschere, K. Sargsyan, M. Salloum, H. Adalsteinsson, and O.M. Knio. Uncertainty quantification in md simulations. part i: Forward propagation. *Multiscale Model. & Simul.*, in press, 2012.
- [112] F. Rizzi, H.N. Najm, B.J. Debusschere, K. Sargsyan, M. Salloum, H. Adalsteinsson, and O.M. Knio. Uncertainty quantification in md simulations. part ii: Bayesian inference of force-field parameters. *Multiscale Model. & Simul.*, in press, 2012.
- [113] G. O. Roberts and J. S. Rosenthal. Coupling and ergodicity of adaptive markov chain monte carlo algorithms. *J. Appl. Prob.*, 44(2):458–475, 2007.
- [114] G. O. Roberts and J. S. Rosenthal. Examples of adaptive MCMC. *J. Comput. and Graph. Stat.*, 18:349–367, 2009.
- [115] R.A. Robinson and R.H. Stokes. *Electrolyte Solutions*. Butterworth’s, London, 1965.

- [116] J-P. Ryckaert, G. Ciccotti, and H. J. C. Berendsen. Numerical integration of the cartesian equations of motion of a system with constraints: Molecular dynamics of n-alkanes. *J. Comp. Phys.*, 23(3):327–341, 1977.
- [117] M. Salloum, K. Sargsyan, R. Jones, B. Debusschere, H. Najm, and H. Adalsteinsson. A stochastic multiscale coupling scheme to account for sampling noise in atomistic-to-continuum simulations. *Multiscale Modeling & Simulation*, 10(2):550–584, 2012.
- [118] K. Sargsyan, B. Debusschere, H. N. Najm, and Y. Marzouk. Bayesian inference of spectral expansions for predictability assessment in stochastic reaction networks. *J. Comput. Theor. Nanosci.*, 6:2283–2297, 2009.
- [119] Robert M. Shroll and David E. Smith. Molecular dynamics simulations in the grand canonical ensemble: Formulation of a bias potential for umbrella sampling. *The Journal of Chemical Physics*, 110(17):8295–8302, 1999.
- [120] B.W. Silverman. *Density estimation for statistics and data analysis*. Chapman and Hall, 1986.
- [121] Derek Stein, Maarten Kruithof, and Cees Dekker. Surface-charge-governed ion transport in nanofluidic channels. *Phys. Rev. Lett.*, 93:035901, 2004.
- [122] J. A. Templeton, R. E. Jones, J. W. Lee, B. M. Wong, and J. A. Zimmerman. A long-range electric field solver for molecular dynamics based on atomistic-to-continuum modeling. *J. Chem. Theory Comput.*, 7(6):1736–1749, 2011.
- [123] J.A. Templeton, R.E. Jones, and G.J. Wagner. Application of a field-based method to spatially varying thermal transport problems in molecular dynamics. *Modelling Simul. Mater. Sci. Eng.*, 18:085007, 2010.
- [124] Karl P. Travis and Keith E. Gubbins. Combined diffusive and viscous transport of methane in a carbon slit pore. *Molecular Simulation*, 25(3-4):209–227, 2000.
- [125] Karl P. Travis and Keith E. Gubbins. Poiseuille flow of Lennard-Jones fluids in narrow slit pores. *The Journal of Chemical Physics*, 112(4):1984–1994, 2000.
- [126] B. A. Turlach. Bandwidth selection in kernel density estimation: A review. In *CORE and Institut de Statistique*, 1993.
- [127] M. H. Ulz, K. K. Mandadapu, and P. Papadopoulos. On the estimation of spatial averaging volume for determining stress using atomistic methods. *Model. Sim. Mat. Sci. Eng.*, 21:15010–15024, 2013.
- [128] Loup Verlet. Computer “experiments” on classical fluids. I. thermodynamical properties of Lennard-Jones molecules. *Phys. Rev.*, 159(1):98, 1967.
- [129] G.J. Wagner, R.E. Jones, J.A. Templeton, and M.L. Parks. An atomistic-to-continuum coupling method for heat transfer in solids. *Comp. Meth. Appl. Mech. Eng.*, 197:3351–3365, 2008.

- [130] G.J. Wagner and W.K. Liu. Coupling of atomistic and continuum simulations using a bridging scale decomposition. *J. Comp. Phys.*, 190:249–274, 2003.
- [131] T. Werder, J.H. Walther, and P. Koumoutsakos. Hybrid atomistic-continuum method for the simulation of dense fluid flows. *J. Comp. Phys.*, 205:373–390, 2005.
- [132] N. Wiener. The homogeneous chaos. *Am. J. Math.*, 60:897–936, 1938.
- [133] I.-C. Yeh and M. L. Berkowitz. Ewald summation for systems with slab geometry. *J. Chem. Phys.*, 111:3152–3162, 1999.
- [134] I.-C. Yeh and M.L. Berkowitz. Ewald summation for systems with slab geometry. *Journal of Chemical Physics*, 111(7):3155–3162, 1999.
- [135] JD Zhou, ST Cui, and HD Cochran. Molecular simulation of aqueous electrolytes in model silica nanochannels. *Molecular Physics*, 101(8):1089–1094, 2003.
- [136] Urs Zimmerli, Pedro G. Gonnet, Jens H. Walther, and Petros Koumoutsakos. Curvature induced I-defects in water conduction in carbon nanotubes. *Nano Letters*, 5(6):1017–1022, 2005.
- [137] J. A. Zimmerman, E. B. Webb III, J. J. Hoyt, R. E. Jones, P. A. Klein, and D. J. Bammann. Calculation of stress in atomistic simulation. *Modelling Simul. Mater. Sci. Eng.*, 12:S319–S332, 2004.
- [138] J.A. Zimmerman, R.E. Jones, and J.A. Templeton. A material frame approach for evaluating continuum variables in atomistic simulations. *J. Comp. Phys.*, 229(6):2364–2389, 2010.

DISTRIBUTION:

- 1 MS 0899 Technical Library, 8944 (electronic)
- 1 MS 0123 D. Chavez, LDRD Office, 1011

This page intentionally left blank.



Sandia National Laboratories